

Copyright

by

Reed Anthony Anzalone

2010

**The Thesis Committee for Reed Anthony Anzalone  
Certifies that this is the approved version of the following thesis:**

**A Toolkit for Characterizing Uncertainties in  
Hypersonic Flow-Induced Ablation**

**APPROVED BY  
SUPERVISING COMMITTEE:**

**Supervisor:**

---

Ofodike A. Ezekoye

---

Rochan R. Upadhyay

**A Toolkit for Characterizing Uncertainties in  
Hypersonic Flow-Induced Ablation**

**by**

**Reed Anthony Anzalone, B.S.**

**Thesis**

Presented to the Faculty of the Graduate School of

The University of Texas at Austin

in Partial Fulfillment

of the Requirements

for the Degree of

**Master of Science in Engineering**

**The University of Texas at Austin**

**December 2010**

## Acknowledgements

I would first like to thank my advisor, Dr. Ofodike Ezekoye, for all of his guidance, advice, and patience with me while I worked on this thesis. He has been an integral part of my work and development over the course of this process and I cannot acknowledge or praise his efforts enough. I must also acknowledge the work of Dr. Rochan Upadhyay, whose ablation library is underpinning much of the work in this code, and whose expertise in the quadrature method of moments has helped a great deal. This work would not exist without his assistance.

I must thank PECOS for their support, and for the framework and funding that enabled this research to be conducted: this work was supported by the Department of Energy (National Nuclear Security Administration) under Award Number (DE-FC52-08NA28615). As well, the PECOS Center staff in general have been an invaluable source of help and enlightenment over the past two years. I would particularly like to acknowledge Karl Schulz and Jeremy Jagodzinski, whose capability and knowledge of computing and experimentation have been extremely beneficial. Thanks are also due to Ben Blackwell, formerly of the Sandia National Lab, for his help in my knowledge and understanding of ablation and his kindness to me during my brief visit to Albuquerque.

Finally, I must thank my absolutely wonderful girlfriend Alex. She has always been loving and supportive throughout the course of my graduate education, and has helped me through difficult times with patience and compassion. I would not have made it here without her.

December 3, 2010

## **Abstract**

# **A Toolkit for Characterizing Uncertainties in Hypersonic Flow-Induced Ablation**

Reed Anthony Anzalone, M.S.E.

The University of Texas at Austin, 2010

Supervisor: Ofodike A. Ezekoye

A one-dimensional, quasi-steady ablation model with finite rate surface chemistry and frozen equilibrium pyrolysis gases is developed and discussed. This material response model is then coupled to a film-transfer boundary layer model to enable the computation of heat and mass transfer to and from the ablating surface. A shock model is outlined, as well, and all three components are then coupled together to form a stand-alone ablation code.

The coupled models in the code are validated with respect to arcjet experiments, and comparisons are drawn between the ablation code and the unsteady ablation code Chaleur, as well as other computations for a graphite ablator in an arcjet. The coupled code is found to compare very well to both the experimental results and the other

calculations. It is also found to have unique computational capabilities due to the use of finite-rate surface chemistry.

Finally, uncertainty propagation using the quadrature method of moments (QMOM) is discussed. The method is applied to a number of simplified sample problems, for both univariate and multivariate scenarios. QMOM is then used to compute the uncertainty in an application of the coupled ablation code using a graphite ablator. The results of this study are discussed, and conclusions about the utility of the method as well as the properties of the ablation code are drawn.

## Table of Contents

List of Tables .....	xii
List of Figures .....	xiii
Chapter 1: Introduction .....	1
1.1: Literature Review .....	2
Chapter 2: Ablation Modeling .....	4
2.1: Ablation Basics .....	4
2.2: The Quasi-Steady Ablation Library .....	6
2.2.1: Conservation Laws .....	6
2.2.2: Flow-Side Boundary Conditions .....	8
Surface Mass Balance .....	9
Surface Energy Balance .....	10
Surface Chemistry Models .....	11
2.2.3: Pyrolysis Gases .....	13
Pyrolysis Gas Production Rate Model .....	13
Pyrolysis Gas Composition Model .....	14
2.3: Flow-Side Models .....	17
2.3.1: Convective Heat Flux .....	18
2.3.2: Heat Transfer Coefficient Model .....	19
2.3.3: Blowing Correction .....	21
2.3.4: Hot Wall Correction .....	21
2.3.5: Diffusive Mass Fluxes .....	22
2.4: Supplementary Models .....	23
2.4.1: Shocks .....	23
2.4.2: Surface Pressure .....	24
2.4.3: Equation of State .....	24
Mole and Mass Fractions .....	25
2.4.4: Gas Thermodynamic Properties .....	26

Correlations.....	26
Thermodynamic Properties of Mixtures .....	27
2.4.5: Transport Properties.....	27
Transport Properties of Mixtures .....	28
Chapter 3: Code Development.....	29
3.1: Ablation Code Solution Method.....	29
3.1.1: Residuals and Jacobian of the Ablation Code .....	30
3.2: Ablation Code Procedure.....	32
3.3: Pyrolysis Gas Equilibrium Calculations .....	33
3.3.1: Pyrolysis Gas Equilibrium Calculation Procedure .....	35
3.4: Shock Code Implementation.....	36
3.4.1: Shock Code Procedure.....	38
3.4.2: Shock Code Coupling to the Ablation Code.....	39
Chapter 4: Model Validation and Code-to-Code Comparison .....	41
4.1: Submodel Validation .....	41
4.2: Shock Code Comparison .....	42
4.3: Ablation Code Model Validation with Arcjets.....	43
4.3.1: Issues with Arcjet Comparison.....	44
4.3.2: Arcjet Enthalpy Determination Methods .....	45
The Energy Balance Method .....	45
The Sonic Throat Method .....	46
Enthalpy Based on Heat Flux .....	47
4.3.3: Comparison to Covington.....	47
4.4: Comparison of Models Used in Chaleur and the Ablation Code .....	51
4.4.1: Comparison Method for Chaleur .....	53
4.4.2: Initial Chaleur Comparisons .....	56
4.4.3: Analysis of the Ablation Code B' Curve.....	64
New Chaleur Comparison Method .....	67
4.4.4: Final Chaleur Comparisons .....	68

Graphite Ablator Comparison .....	68
PICA Comparison .....	71
4.5: Chen and Milos Comparison .....	74
Chapter 5: Uncertainty Propagation with the Direct Quadrature Method of Moments .....	77
5.1: Uncertainty Propagation .....	77
5.2: Introduction to the Quadrature Method of Moments .....	78
5.3: libMoM .....	79
5.4: Application of QMOM .....	80
5.4.1: Univariate Cases .....	80
Univariate Example – $y = x^2$ .....	81
5.4.2: Multivariate Cases .....	81
Bivariate Example – $z = xy$ .....	83
5.5: Sample Problem .....	83
5.6: Selection of Uncertain Parameters .....	86
5.7: Uncertainty Propagation with Graphite in the Chen and Milos Conditions .....	88
5.7.1: Preliminary Uncertainty Analysis and Parameter Distributions .....	88
Probability Density of $\rho_c$ .....	90
Probability Density of $E_a, C_3, eq$ .....	91
Probability Density of $AC_3, eq$ .....	92
Probability Density of $\epsilon$ .....	93
Probability Density of $\beta N$ .....	94
5.7.2: QMOM Calculation Results .....	96
Chapter 6: Conclusions and Future Work .....	99
Appendix A: Ablation Code Inputs .....	101
A.1: Inputs in the [wrapper] Section .....	101
A.1.1: General Inputs .....	101
A.1.2: Flow Inputs .....	101
A.2: Inputs in the [ablation1d] Section .....	102

A.3: Inputs in the [ablation/standalone] Section .....	104
A.4: Inputs in the [ablator/props/graphite1] Section .....	105
A.5: Inputs in the [ablator/props/charring1] Section .....	105
A.6: Inputs in the [ablation1d/chemistry/10species] Section .....	106
A.7: Inputs in the [ablation1d/chemsitry/13species] Section .....	107
Appendix B: Nominal Parameters .....	108
B.1: Graphite Ablator Properties .....	108
B.2: PICA Properties .....	108
B.3: Kinetic Parameters .....	109
Appendix C: Jacobian of the Ablation Code .....	110
C.1: Common Terms.....	110
C.1.1: Sensitivities of the Gas Phase Density .....	110
C.1.2: Sensitivities of Reaction Terms .....	111
C.1.3: Sensitivities of the Pyrolysis Flux .....	113
C.2: Sensitivities of the Mass Balance Equations.....	114
C.2.1: Sensitivities of the Diffusive Term .....	114
C.2.2: Sensitivities of the Blowing Term.....	114
C.2.3: Sensitivities of the Reaction Term .....	115
C.2.4: Sensitivities of the Pyrolysis Flux Term .....	115
C.3: Sensitivities of the Surface Recession Rate Equation.....	115
C.3.1: Sensitivities of the Blowing Flux .....	116
C.3.2: Sensitivities of the Char Mass Loss Rate .....	116
C.3.3: Sensitivities of the Pyrolysis Mass Flux .....	117
C.4: Sensitivities of the Energy Balance Equation .....	117
C.4.1: Sensitivities of the Convective Heat Flux Term .....	117
C.4.2: Sensitivities of the Reaction Energy Term.....	118
C.4.3: Sensitivities of the Pyrolysis Enthalpy Flux Term.....	118
C.4.4: Sensitivities of the Radiative Heat Fluxes .....	119
C.4.5: Sensitivities of the Virgin Material Enthalpy Flux .....	119

Bibilography .....	120
Vita.....	124

## List of Tables

Table 4.1: Computed results of the shock code with values from Wittliff and Curtis [34].	42
Table 4.2: Comparison of results from the ablation code with the average of the results obtained from comparable experiments by Covington [35].	50
Table 4.3: Parameters used to generate the curves shown in Figure 4.3 through Figure 4.5.	57
Table 4.4: Parameters used to generate the curves shown in Figure 4.8	69
Table 4.5: Parameters used to generate the curves shown in Figure 4.10.	71
Table 4.6: Comparison of results from the ablation code to calculations by Chen and Milos.	75

## List of Figures

Figure 2.1: The physics encountered in hypersonic ablation.....	5
Figure 2.2: Quasi-steady ablation processes and their equations [22].....	9
Figure 3.1: Coupling of the shock code with the ablation code.....	40
Figure 4.1: Method for carrying out computations of both Chaleur and the ablation code.....	54
Figure 4.2: Plot of surface recession rate versus time for Chaleur with a graphite ablator. ....	58
Figure 4.3: $B'$ versus surface temperature for the ablation code and Chaleur with a graphite ablator. ....	60
Figure 4.4: Ablation rates versus surface temperature for the ablation code and Chaleur using a graphite ablator. ....	61
Figure 4.5: $B'$ versus surface temperature for the ablation code and Chaleur using a graphite ablator. These results were computed using $x_{C3,eq}$ values fitted from ACE.....	63
Figure 4.6: A typical ignition and extinction process. ....	64
Figure 4.7: $B'$ versus surface temperature for a number of values of $hm$ over a range of input recovery enthalpies.....	67
Figure 4.8: $B'$ versus surface temperature for Chaleur and the ablation code, over a range of input enthalpies and with $hm = 0.01$ .....	70
Figure 4.9: Plot of surface recession rate versus time for Chaleur running with a PICA ablator. ....	72

Figure 4.10: $Bc'$ versus surface temperature for PICA in air, with $hm = 0.1$ and the freestream velocity, which effectively sets the recovery enthalpy, varied from 1000 to 10000 m/s.....	73
Figure 5.1: Percent change of the ablation rate with respect to the percent change in the input parameters.....	89
Figure 5.2: Probability density function of the graphite density, which is a Gaussian distribution with a mean of $2162.5 \text{ kg/m}^3$ and standard deviation of $144.167 \text{ kg/m}^3$ .....	91
Figure 5.3: Probability density function of the tricarbon equilibrium concentration activation energy, which is a Gaussian distribution with a mean of 90908 K and a standard deviation of 1515 K. ....	92
Figure 5.4: Probability density function of the tricarbon equilibrium concentration pre-exponential, which is a Gaussian with a mean of $6.27 \times 10^{14} \text{ Pa}$ and standard deviation of $1.045 \times 10^{13} \text{ Pa}$ . ....	93
Figure 5.5: Probability density function of the graphite surface emissivity, which is a beta distribution with $\alpha = 20$ and $\beta = 2$ . ....	94
Figure 5.6: Probability density function of the nitridation reaction probability, which is a beta distribution with $\alpha = 2$ and $\beta = 600$ . ....	96
Figure 5.7: Cumulative distribution function for the surface recession rate, using the input pdfs described in Section 5.7.1:.....	97

## Chapter 1: Introduction

Ablation, in the context of this thesis, is the process by which material subjected to high thermal and mechanical stresses begins to degrade and react with the gases around it. While this process is important in many physical phenomena, such as the pyrolysis and eventual combustion of solid materials in fire, this paper will focus on the application of ablation as a thermal protection system for a vehicle entering a planetary atmosphere. Energy is consumed in the material degradation process and is therefore redirected from the vehicle, protecting it from the high heat fluxes encountered while using aerodynamic braking to slow the vehicle down during its descent.

Prior to this work, Upadhyay and other researchers at the Center for Predictive Engineering and Computational Science (PECOS) at the University of Texas had developed a one-dimensional quasi-steady ablation model for use with computational fluid dynamics simulations of the Orion Crew Exploration Vehicle in hypersonic re-entry. The resulting ablation library module, the models involved in which will be explored in detail, forms the basis of the current work. The goal, then, of this research is to augment the existing ablation library by coupling it to a film-transfer boundary layer, forming a stand-alone code. The coupled ablation code is then validated by comparison to arcjet experiments and, because the experimental validation was found to be insufficient, different ablation computations.

As one of the stated goals of the PECOS center is the pursuit of uncertainty quantification methodologies, the sensitivities of the ablation code to its input parameters are discussed. The ablation code is then used to propagate parameter uncertainty through to the quantity of interest--in this case, the ablation rate. The quadrature method of moments (QMOM) will be used to perform the forward uncertainty propagation, resulting in a single estimated probability density function of the quantity of interest based on uncertainty distributions for some of the input parameters.

## 1.1: LITERATURE REVIEW

Formal scientific and engineering research on ablation did not begin in earnest until the mid-1950s, when a growing interest in both civilian and military spaceflight spurred the research community into action. This was helped in large part by the 1958 creation of NASA, which has both pursued and pushed ablation research as a significant issue requiring careful study. Much of the work in the field of ablation has been done either by NASA directly or through their contractors.

The Aerotherm Corporation, a NASA contractor based in Palo Alto, was responsible for some of the more significant milestones in the ablation community. Rindal and Moyer [1] developed the Charring Materials Ablation (CMA) code while at Aerotherm, which was based on Rindal's previous work with Kendall and Bartlett [2]---a paper that remains a classic in the field and has guided a good deal of research since. Also out of the same group came the Aerotherm Chemical Equilibrium (ACE) code [3] which along with CMA forms a code suite that can be used to help design ablation systems.

Recently there has been a new surge of interest in ablation, due in large part to the ending of the space shuttle program and the re-development of blunt-body reentry vehicles. Starting in the mid-1990s, a number of ablation codes have been developed with varying levels of fidelity. Chen and Milos have developed FIAT [4], a one-dimensional code, and TITAN [5], a two-dimensional code that can simulate the changing shape of an ablator. Blackwell and Amar developed [6] Chaleur, a one-dimensional code which uses a newer solving scheme to determine the in-depth decomposition of an ablator.

The code being developed in the current work is motivated not out of a desire to have a more accurate model of the in-depth decomposition of an ablator, but out of the realization that equilibrium may not be the best way to characterize what is happening at the ablating surface. All of the codes mentioned previously use the same method to determine the surface recession rate: pre-computed tables of non-dimensionalized mass loss rates known as  $B'$  tables. Computing

power has advanced sufficiently in the last 40 years that it is possible to compute mass loss rates “on the fly” by looking at finite-rate kinetics at the surface.

Zhukov and Abe [7] and Chen and Milos [8] have recently been actively pursuing research in ablation codes with finite-rate chemistry. This work is aided by research in surface reactions, much of which has been led by Park [9,10] who has long studied aerothermodynamics. Recently some of his findings with respect to surface nitridation have been called into question by Marschall [11] and other researchers; the issue will be briefly discussed in the current work.

The ablation code outlined herein was originally developed to be coupled to NASA’s DPLR CFD code, but in the current work it is coupled to a film-transfer boundary layer. This entails modeling the heat and mass transfer on the gas-side of the ablator. A wide variety of studies have been done on stagnation-point heat transfer over the last 40 or so years. Zoby [12] and Sutton and Graves [13] developed simple, empirical correlations for the heat transfer coefficient based solely on the gas composition. These have been widely used in arcjet research. Fay and Riddell [14] and also Fay and Kemp [15] developed more complex semi-empirical relationships for the heat transfer coefficient, and these and a number of different blunt-body heating methods were collected into a very useful report by Crabtree, Dommett, and Woodley [16]. More recently, Quinn and Gong [17] revisited Fay and Riddell’s work and found it to be a good predictor of heat transfer in a variety of situations.

Coupling a boundary layer to the ablating surface transforms the code in the current work into a simple and efficient standalone ablation program, which is ideal for doing basic uncertainty analysis. Rather than using Monte Carlo methods, we instead opt to use the more computationally efficient quadrature based sampling procedure first used by Upadhyay and Ezekoye [18,19]. This method uses concepts from the Quadrature Method of Moments (QMOM), originally developed by McGraw [20]. The quadrature formula obtained from the moments of the density function is used to compute moments of the quantity of interest. Then the CDF is estimated by the moments by matching these moments with those of the Generalized Lambda Distribution (GLD) as described in Karian and Dudewicz [21].

## Chapter 2: Ablation Modeling

### 2.1: ABLATION BASICS

The reaction processes at the surface and in-depth are what make an ablator an effective thermal protection system. Reactions degrade the material and release volatile gases, which carry energy out of the ablator and into the flow field. As the ablator is subjected to heating, the ablation process itself proceeds generally as follows:

- The material begins to increase in temperature from the surface inward.
- When the temperature at the surface of the material reaches some critical value, the molecules at the surface begin to break apart and degrade, producing volatile gases in a process known as pyrolysis. These gases react with one another and the gases surrounding the material.
- The pyrolysis process continues into the material as a front (of generally unknown thickness), consuming the molecules that will break down and leaving behind a porous, carbonaceous char. Gases from the pyrolysis process, driven by the pressure differential between the inside of the material and its surface, filter out through the char and into the freestream. The temperature of the material continues to increase.
- When the surface of the material reaches a certain temperature, the char begins to react with the surrounding gases. This can occur through oxidation, nitridation, and sublimation of the surface carbon. As carbon is consumed in the surface reactions, the surface begins to recede in much the same manner as the pyrolysis front had before (though not necessarily the same rate).
- Surface and in-depth recession continue until there are no more volatile gases to be released from the interior of the ablator.

While this is the process for charring ablators, non-charring ablators work in a very similar way -- the difference being that non-charring ablators do not experience the in-depth decomposition that charring ablators do, and all of the reactions occur at the surface.

When an ablator is put into use as a thermal protection system on a re-entry vehicle, the surface is subjected to a wide variety of physical phenomena due to the physics of the hypersonic flow field around the ablator. An illustration listing many of the flow-side phenomena is given as Figure 2.1.

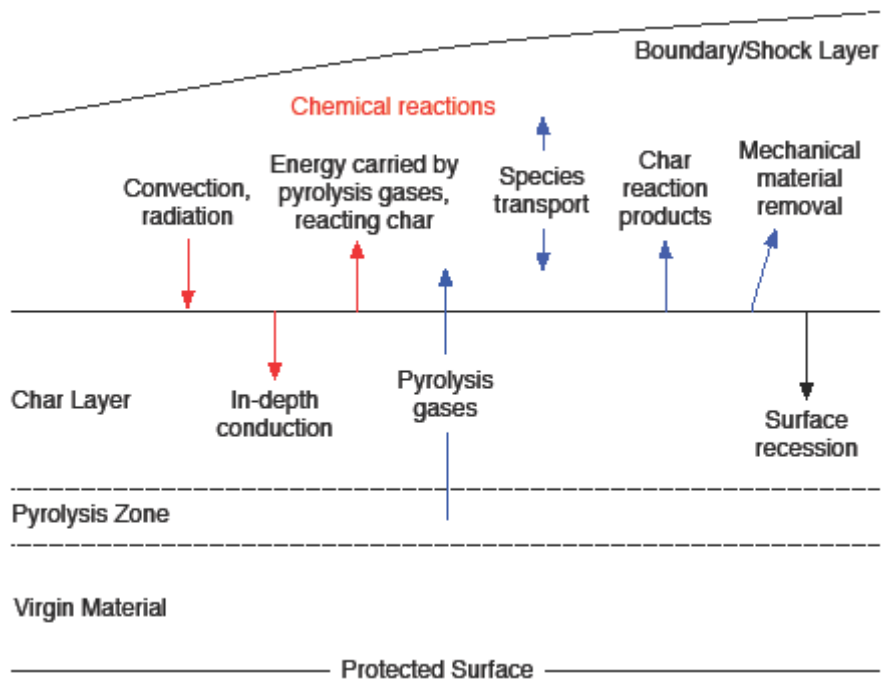


Figure 2.1: The physics encountered in hypersonic ablation.

A normal shock (which for blunt-body ablators is known as a bow shock) forms off the surface of the ablator. The shock heats the flow to extreme temperatures and causes the dissociation of many of the incident gaseous species. Inside the shock there are chemical reactions in the flow. Radiation between the surface of the ablator and the shock is an important phenomenon, and the gas between them acts as a participating medium. But radiation, while important, is not the only heat transfer mechanism; a huge amount of energy is transferred to the

surface by convection from the high-enthalpy external flow. Due to the mechanical forces the ablator is subjected to, especially shear loading, there is mechanical erosion on the surface.

## 2.2: THE QUASI-STEADY ABLATION LIBRARY

The ablation model developed at PECOS by Dr. Rochan Upadhyay and others simulates material response to imposed boundary conditions. It is a one-dimensional, quasi-steady ablation model. The goal of this section is to give an overview of the pieces of the model that are important to the current work and to provide some context and motivation for modeling and validation efforts that will follow later in the paper.

### 2.2.1: Conservation Laws

The conservation laws considered in the PECOS ablation model are conservation of mass (in both the solid and gas phases) and conservation of energy for a solid-gas mixture. They are formulated in a one-dimensional Cartesian coordinate system with assumptions that pyrolysis gases are non-reactive as they flow through the char, there is no thermal expansion of the solid, there is no radiative transfer within the char, the solid material is semi-infinite, and that there are no pressure gradients within the char [22].

If we describe the solid-gas mixture as having an effective density, we can write the solid-gas energy equation as

$$\frac{\partial \rho_{eff} e}{\partial t} - \frac{\partial \dot{m}_{py}'' i_g}{\partial z} = \frac{\partial}{\partial z} k_s \frac{\partial T}{\partial z} \quad 2.1$$

where the term  $e$  is the effective internal energy of the solid,  $\dot{m}_{py}''$  is the mass flux of pyrolysis gases,  $i$  is the specific enthalpy,  $k_s$  is the bulk thermal conductivity of the solid, and  $\rho_{eff}$  is the effective density in the solid, which can be represented in terms of a void fraction  $\phi$  and the densities of the solid and gas phases in the porous char layer:

$$\rho_{eff} = \phi \rho_{py} + (1 - \phi) \rho_s \quad 2.2$$

The gas and solid phase continuity equations can be represented as

$$\frac{\partial \rho_s}{\partial t} = -\dot{m}_s''' \quad 2.3$$

$$\frac{\partial \phi \rho_{py}}{\partial t} - \frac{\partial \dot{m}_{py}''}{\partial z} = \dot{m}_s''' \quad 2.4$$

where the  $\dot{m}_s'''$  terms are source/sink terms for the creation and destruction of solid and gaseous species in reactions.

Since the surface is receding, we can define a coordinate system in a moving frame of reference attached to the surface, given by  $x = z - s(t)$ . This transforms the derivatives according to

$$\frac{\partial}{\partial t} \Big|_z = \frac{\partial}{\partial t} \Big|_x - \frac{ds}{dt} \frac{\partial}{\partial x} \Big|_x \quad 2.5$$

and

$$\frac{\partial}{\partial z} \Big|_z = \frac{\partial}{\partial x} \Big|_x \quad 2.6$$

If the system is assumed to reach steady state in the context of the moving frame of reference, we can say that time derivatives at constant  $x$  are zero. We will also assume that the gas density is significantly less than the solid density, and therefore that the effective density  $\rho_{eff} \approx \rho_s$ .

Finally, we will assume that the system is quasi-steady; that is, that the rate of ablation is constant and  $ds/dt = v_s = \text{const}$ . With these assumptions we can write the energy equation as

$$-v_s \frac{\partial \rho_s e}{\partial x} - \frac{\partial \dot{m}_{py}'' i_{py}}{\partial x} = \frac{\partial}{\partial x} k_s \frac{\partial T}{\partial x} \quad 2.7$$

We can combine Equations 2.3 and 2.4 to write the mass conservation equation as

$$-v_s \frac{\partial \rho_s}{\partial x} - \frac{\partial \dot{m}_{py}''}{\partial x} = 0 \quad 2.8$$

These two equations are then integrated over the length of the ablator (from  $x = 0$  to  $x \rightarrow \infty$ ) to form a global mass and energy balance. Since the back face condition is adiabatic due to the semi-infinite boundary condition, the integrated energy equation comes out to

$$k_s \frac{\partial T}{\partial x} \Big|_{s,w} = -v_s \rho_s i \Big|_{s,w} + v_s \rho_s i \Big|_{x \rightarrow \infty} - \dot{m}''_{py} i_{py} \Big|_{s,w} \quad 2.9$$

Similarly, the mass conservation equation becomes

$$\dot{m}''_{py} = -v_s (\rho_s \Big|_{s,w} - \rho_s \Big|_{x \rightarrow \infty}) = -v_s (\rho_c - \rho_v) \quad 2.10$$

This integration process only takes care of half of the boundary conditions, however. While the conditions on the interior of the ablator at the infinite boundary are assumed to be known, the conditions at the ablating surface are decidedly unknown. Constitutive relations for parameters on the gas side of the wall will help complete the system of equations that will be solved.

### 2.2.2: Flow-Side Boundary Conditions

Since the global balances on the interior of the ablator have been defined, we must now explore the boundary conditions that occur on the ablator's surface for both energy and mass conservation. Figure 2.2, from [22] gives a good overview of the processes involved and their equations, and will be explained over the course of this section.

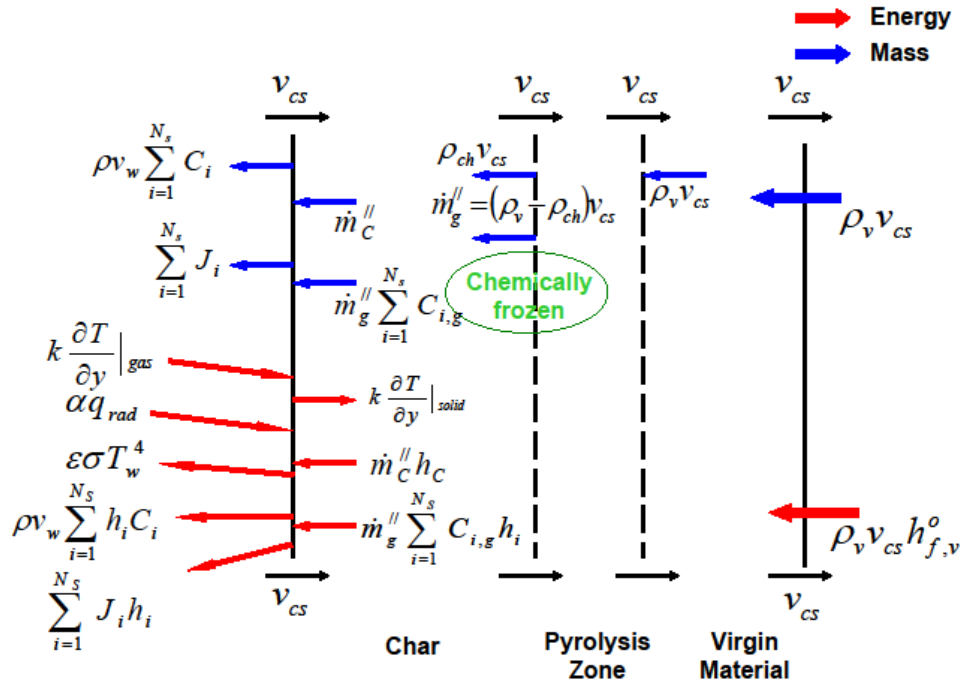


Figure 2.2: Quasi-steady ablation processes and their equations [22].

### Surface Mass Balance

Mass is conserved at the surface through conservation of species. The surface mass balance may be represented as:

$$J_i|_{g,w} + \rho_g v_w Y_{i,w} = \tilde{N}_i + \dot{m}''_{py} Y_{i,py} \quad 2.11$$

where  $J_i|_{g,w}$  represents the diffusive flux of the  $i^{\text{th}}$  species out of the wall,  $\rho_g v_w Y_{i,w}$  is the convective flux of the  $i^{\text{th}}$  species out of the wall,  $\tilde{N}_i$  is a kinetic source/sink term to describe the creation or destruction of the  $i^{\text{th}}$  species through reactions, and  $\dot{m}''_{py} Y_{i,py}$  is the flux of the  $i^{\text{th}}$  gas species in the pyrolysis gases. In Equation 2.11, while the rightmost three terms and the pyrolysis flux term are computed internally by the ablation code, the diffusive flux is not --- it must be provided by some sort of flow-side model.

### Surface Energy Balance

Energy is conserved at the surface as well. The surface energy balance may be represented as

$$\begin{aligned}
 -k_g \frac{\partial T}{\partial Y} \Big|_{g,w} - \sum_{i=1}^{N_s} i_i J_i \Big|_{g,w} + \rho_g v_g \sum_{i=1}^{N_s} Y_{i,g} i_i + \dot{m}_c'' i_c \\
 + \dot{m}_{py}'' \sum_{i=1}^{N_s} Y_{i,py} i_i + \alpha q_{rad}'' - \epsilon \sigma T_w^4 + k_s \frac{\partial T}{\partial Y} \Big|_{s,w} = 0
 \end{aligned} \tag{2.12}$$

where, from left to right, the terms represent: diffusive flux of energy to the surface from the gas phase, energy carried by gases diffusing out of the surface, energy carried by convecting gases out of the surface, energy carried by char convecting in to the surface, energy convected by pyrolysis gases into the surface, radiative flux in to the surface, radiative flux out of the surface, and conduction in to the solid (which is represented as going out of the surface).

If we consider Equation 2.12 we may reformulate the conductive flux term using the global energy balance. If we assume that the interior of the ablator is at the reference temperature for the enthalpy of formation of the virgin material, we have

$$k_s \frac{\partial T}{\partial Y} = -\dot{m}_c'' i_c - \dot{m}_{py}'' \sum_{i=1}^{N_s} Y_{i,py} i_i + \rho_v v_s i_{f,v}^\circ \tag{2.13}$$

If we then multiply the surface species conservation equation, Equation 2.11, by the enthalpy of each species and sum over all of the species, we get

$$\sum_{i=1}^{N_s} i_i [J_i \Big|_{g,w} + \rho_g v_w Y_{i,w}] = \sum_{i=1}^{N_s} i_i [\tilde{N}_i + \dot{m}_{py}'' Y_{i,py}] \tag{2.14}$$

Taking the right hand sides of Equations 2.13 and 2.14, substituting them into their respective terms in Equation 2.12, and rewriting the convective heat flux term as a single term yields the final surface energy balance:

$$q_{conv}'' - \sum_{i=1}^{N_s} i_i [\tilde{N}_i + \dot{m}_{py}'' Y_{i,py}] + \alpha q_{rad}'' - \epsilon \sigma T_w^4 + \rho_v v_s i_{f,v}^\circ = 0 \tag{2.15}$$

Again, as in Equation 2.11, the diffusive heat flux term must be provided by a flow-side model.

## Surface Chemistry Models

Because of the quasi-steady model being used for material response, surface chemistry is perhaps the most important of the sub-models. The surface chemistry controls the surface recession rate, which in turn sets the in-depth recession rate and thus the overall mass loss rate. Technically, there are two chemistry models: there is a 10-species model, where the species considered are CO, CN, C<sub>3</sub>, N, O, O<sub>2</sub>, N<sub>2</sub>, NO, C<sub>2</sub>, and C; and a 13-species model which considers all of the species in the 10-species model as well as C<sub>2</sub>H, H<sub>2</sub>, and H. In general, the 10-species model is supposed to be used for non-decomposing ablators, which will not produce hydrogen species, whereas the 13-species model is designed to be used with decomposing ablators, where hydrogen may be produced in the pyrolysis gases. While the 10-species model may not be suitable for decomposing ablators, there is no reason that the 13-species model could not be used for any problem and has, in fact, been used in all of the computations presented in this paper.

Regardless of the chemistry model used, only four reactions between the gas phase and the surface are considered:

- Oxidation (with atomic oxygen):  $C(s)+O\rightarrow CO$
- Oxidation (with molecular oxygen):  $C(s)+\frac{1}{2}O_2\rightarrow CO$
- Nitridation:  $C(s)+N\rightarrow CN$
- Sublimation:  $3C(s)\rightarrow C_3$

The chemistry of the oxidation and nitridation reactions is modeled by Arrhenius terms of the form

$$\dot{m}''_{i,C} = \rho Y_i \sqrt{\frac{k_B T}{2\pi m_i}} \beta_i \frac{W_C}{W_i} \quad 2.16$$

Where  $\dot{m}''_{i,C}$  is the mass loss of carbon due to reactions with the  $i^{\text{th}}$  species. The sublimation reaction is modeled slightly differently, in terms of the difference between the equilibrium and actual surface concentrations of tricarbon:

$$\dot{m}_{C_3,C}'' = \rho(x_{C_3,eq} - x_{C_3}) \sqrt{\frac{k_B T}{2\pi m_{C_3}}} \beta_{C_3} \quad 2.17$$

In the above equations, the reaction probability  $\beta_i$  is generally modeled in the form

$$\beta_i = A_i e^{-E_{a,i}/T} \quad 2.18$$

where  $A_i$  and  $E_{a,i}$  are the pre-exponential and the activation energy, respectively, of the  $i^{\text{th}}$  species. In some cases, though,  $B_i$  has been found to be a constant. For molecular oxygen reactions with the surface,  $\beta_{O_2}$  is specified as 0.25, though Chen and Milos [8] used it in the range from 0 to 0.5. They also varied  $\beta_{C_3}$  from 0.1 to 1 and found that changing it had little net effect; it is therefore taken here to be 1. For surface nitridation,  $\beta_N$  is specified by Park and Bogdanoff [10] to be 0.3 --- though this is disputed by Marschall [11] and will be investigated later in this paper. The equilibrium concentration of tricarbon at the surface can be given by

$$x_{C_3,eq} = \frac{P_{C_3,eq}}{P} = \frac{A_{C_3,eq}}{P} \exp\left(\frac{-E_{a,C_3,eq}}{T_w}\right) \quad 2.19$$

As mentioned earlier in the section, up to 13 species will be considered in the gas phase: the six that participate in surface reactions (CO, CN, C<sub>3</sub>, O, O<sub>2</sub>, N), four that do not (N<sub>2</sub>, NO, C<sub>2</sub>, C(g)), and those produced in the pyrolysis process (C<sub>2</sub>H, H<sub>2</sub>, H). Their species mass loss terms relate back to the source/sink terms in Equation 2.11, which may be written by summing the mass loss rates of carbon over all of the reactions that produce the  $i^{\text{th}}$  species.

As such, the source/sink terms for all of the species that participate in the reactions may be written:

$$\tilde{N}_{CO} = \dot{m}_{O,C}'' \frac{W_{CO}}{W_C} + \dot{m}_{O_2,C}'' \frac{W_{CO}}{W_C} \quad 2.20$$

$$\tilde{N}_{CN} = \dot{m}_{N,C}'' \frac{W_{CN}}{W_C} \quad 2.21$$

$$\tilde{N}_{C_3} = \dot{m}_{C_3,C}'' \quad 2.22$$

$$\tilde{N}_N = -\dot{m}_{N,C}'' \frac{W_N}{W_C} \quad 2.23$$

$$\tilde{N}_O = -\dot{m}''_{O,C} \frac{W_O}{W_C} \quad 2.24$$

$$\tilde{N}_{O_2} = -\dot{m}''_{O_2,C} \frac{W_{O_2}}{2W_C} \quad 2.25$$

In the same vein, we can also derive a relationship for the total mass loss in the system based on mass conservation. We can say

$$\rho_g v_w = \dot{m}''_C + \dot{m}''_{py} \quad 2.26$$

which means that the net mass flux into the gas phase is equal to the sum of the mass flux of carbon into the ablating surface and the mass flux of pyrolysis gases. This will end up being the blowing residual equation when we go to solve the system. The carbon mass flux can be written in terms of the loss rates due to each surface reaction,

$$\dot{m}''_C = \dot{m}''_{O,C} + \dot{m}''_{O_2,C} + \dot{m}''_{N,C} + \dot{m}''_{C_3,C} \quad 2.27$$

### 2.2.3: Pyrolysis Gases

In the event that the ablator being modeled is a decomposing ablator, we will have to model the production of pyrolysis gases from the decomposition process. Pyrolysis gases are assumed to form at an input pyrolysis temperature, with mass fractions equal to the equilibrium concentrations of the elemental composition of the virgin material at that temperature.

#### *Pyrolysis Gas Production Rate Model*

The rate at which pyrolysis gases are produced is derived from the quasi steady ablation formulation. In the event that in-depth pyrolysis occurs, the rate at which the mass of the virgin material enters the control surface must equal the rate at which gases leave the ablating surface, which is the sum of the pyrolysis flux and the char flux---similar to Equation 2.26, but with the gas velocity and density replaced by the virgin density and the surface recession rate. We can therefore say that

$$\dot{m}''_{py} = \rho_v v_s - \dot{m}''_C \quad 2.28$$

Noting that the char mass loss rate is simply the surface recession rate multiplied by the char density allows us to say

$$\dot{m}''_{py} = \rho_v v_s - \rho_{ch} v_s \quad 2.29$$

which can be written

$$\dot{m}''_{py} = v_s (\rho_v - \rho_{ch}) \quad 2.30$$

The surface recession rate may be written in terms of the blowing velocity:

$$v_s = \frac{\rho_g v_w}{\rho_v} \quad 2.31$$

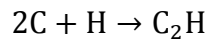
### ***Pyrolysis Gas Composition Model***

The composition of the pyrolysis gases is computed with an equilibrium solution of the composition of the virgin material at a fixed pyrolysis temperature and pressure. These equilibrium computations are done before the code actually starts processing, because they are not dependent on the surface temperature; rather, they are dependent on an input pyrolysis temperature. The equilibrium composition will be computed by minimization of the Gibbs free energy.

Say that the set of gas-phase species considered in the freestream is broken into two subsets: a set  $K$  of pure gaseous elements (C, H, O, and N) and a complementary set  $K^C$  of compounds ( $C_2H$ ,  $N_2$ ,  $O_2$ ,  $NO$ ,  $CO$ ,  $C_2$ ,  $C_3$ ,  $CN$ ,  $H_2$ ). We can treat the formation of one of the compound species from the various elemental species as

$$\sum_{k=1}^K e_{k_i} N_k \rightarrow N_i \quad 2.32$$

where  $e_{k_i}$  is the number of atoms of the  $k^{\text{th}}$  element in the  $i^{\text{th}}$  compound,  $N_k$  denotes the  $k^{\text{th}}$  elemental species, and  $N_i$  denotes the  $i^{\text{th}}$  compound species. For example,



If we create an index  $p$  that runs over all of the species in the set  $K$  and the  $i^{\text{th}}$  compound species (so from 1 to  $N_K + 1$ ), we can say that the Gibbs free energy for the above system is

$$G = \sum_p \left[ n_p \mu_p + n_p RT \ln \left( \frac{P_p}{P_{ref}} \right) \right] \quad 2.33$$

where  $n_p$  is the number of moles of the  $p^{\text{th}}$  species,  $\mu_p$  is the temperature dependent part of the chemical potential of the  $p^{\text{th}}$  species, and  $P_p$  is the partial pressure of the  $p^{\text{th}}$  species. The chemical potential can be written in terms of the enthalpy and entropy as

$$\mu(T) = i(T) - Ts(T) \quad 2.34$$

where the enthalpy and entropy will be defined later in this chapter.

Say now that the affinity,  $A$ , is the derivative of the Gibbs free energy with respect to the species at fixed temperature---in chemical equilibrium,  $A = 0$ . We can write  $A$  in terms of a degree of reaction variable  $\xi$  for a single reaction as

$$A = \left. \frac{\partial G}{\partial \xi} \right|_{P,T} = \sum_p \left[ \nu_p \mu_p + \nu_p RT \ln \left( \frac{P_{ref}}{P_p} \right) \right] = 0 \quad 2.35$$

where  $\nu_p$  is the stoichiometric coefficient for the  $p^{\text{th}}$  species of the reaction in question. For the elemental species  $\nu_p = -e_{\kappa_i}$  and for the compound species  $i$ ,  $\nu_i = 1$ .

The equilibrium constant for the formation of the  $i^{\text{th}}$  species is defined as

$$K_{p,i}(T) = \frac{1}{RT} \left[ - \sum_p \nu_p \mu_p \right] \quad 2.36$$

As such we can substitute the equilibrium constant into Equation 2.35 and rearrange it to say

$$\sum_p \nu_p \ln \left( \frac{P_p}{P_{ref}} \right) = K_{p,i}(T) \quad 2.37$$

If we move the stoichiometric coefficient inside of the natural logarithm, we can say

$$\sum_p \ln \left[ \left( \frac{P_p}{P_{ref}} \right)^{v_p} \right] = K_{p,i}(T) \quad 2.38$$

Let us define a normalized partial pressure by saying

$$P_p^* = \frac{P_p}{P_{ref}} \quad 2.39$$

Equation 2.37 then becomes

$$\sum_p \ln [P_p^{*v_p}] = K_{p,i}(T) \quad 2.40$$

By noting that all of the stoichiometric coefficients of the elemental species will be negative and that the stoichiometric coefficients of the compound species will be unity, this equation can be rearranged to a more usual form:

$$\ln(P_i^*) - \sum_{k=1}^K e_{k_i} \ln(P_k^*) = K_{p,i}(T) \quad 2.41$$

This will give the mole fraction of the  $i^{\text{th}}$  species based on the mole fractions of the  $K$  elemental species inside the ablator. This equation is used for all of the compound species.

There is another relation for the elemental species saying that the amount of an element in the virgin material must be equal to the amount of that element in the pyrolysis gas. As such we can say that

$$Y_{k,v} = \sum_{i=1}^{N_{comp}} e_{k_i} Y_{i,py} \frac{W_k}{W_i} \quad 2.42$$

where the term on the left is the mass fraction of the  $k^{\text{th}}$  species and the term on the right represents the mass fraction of the  $k^{\text{th}}$  species in the pyrolysis gas.

The final relationship for the equilibrium computations of the pyrolysis gas flux is that the sum of the normalized partial pressures of the individual species must be equal to the

normalized pressure---essentially, the partial pressures must sum to the pressure. This can be written

$$\sum_{i=1}^{N_s} P_i^* = P^* \quad 2.43$$

Equations 2.41, 2.42, and 2.43 will be used as the residual equations in a Newton solve that will be performed at the beginning of the execution of the ablation code. More information about the functionality of that solution method (solution variables and Jacobians) may be found in Chapter 3:.

### **2.3: FLOW-SIDE MODELS**

As explored in Section 2.2:, the PECOS one-dimensional in-depth quasi-steady ablation model relies on other models to approximate phenomena coming from the external flow. There must be models for heat transfer, both radiative and convective, and a model for diffusive mass transfer in order to close the system of equations.

The model chosen to approximate the flow field around the ablator is a film transfer model, wherein heat and mass are transferred between the surface and the edge of a boundary layer inside the bow shock layer. The convective heat transfer will be driven by an enthalpy potential and diffusive mass transfer will be driven by a mass fraction potential.

This approximation will not attempt to model some of the flow-side phenomena detailed in Section 2.1: and Figure 2.1, which must be simplified to fit with the film transfer model. There are assumed to be no chemical reactions inside the boundary layer, there is no modeling of gaseous participation in radiative heat transfer, and there is no attempt to model incident radiation on the surface (other than provided as an input constant value to the material response model). The shock may or may not be modeled depending on the desired simulation. Regardless, flow before and after the shock, and at the boundary layer edge, is assumed to be in thermal and chemical equilibrium.

### 2.3.1: Convective Heat Flux

The literature is full of different methods for handling convective heat flux in a film-transfer context. There are correlations for the heat transfer coefficient based on the Nusselt number, the Stanton number, and others; and the convective heat flux calculated with those coefficients may be driven by temperature or enthalpy differential.

We will have multiple options for computing convective heat flux. One will be a temperature driven heat flux of the form

$$q''_{conv} = h_c(T_e - T_w) \quad 2.44$$

where  $T_e$  and  $T_w$  are the boundary layer edge gas and surface temperatures, respectively, and  $h_c$  is a user-provided heat transfer coefficient with units of  $W/m^2K$  that will be kept constant as a parameter throughout the computations. This option will serve in large part as a diagnostic tool.

The second option is to use an enthalpy-driven convective heat flux of the form

$$q''_{conv} = h(i_r - i_w) \quad 2.45$$

where  $h$  is technically a convective mass transfer coefficient, with units of  $kg/m^2s$  and  $i_w$  is the enthalpy at the ablating surface. The other enthalpy term,  $i_r$ , is the recovery enthalpy, which is often defined as

$$i_r = i_e + r \frac{u_e^2}{2} \quad 2.46$$

where  $r$  is a recovery factor which for our purposes will be equal to  $Pr^{1/3}$ . The recovery enthalpy serves as a way to capture the effects of the kinetic energy in the freestream on the heating rate. However, by the time the flow has passed through the shock, it has already been heated by a significant amount and slowed considerably, mitigating its relative importance somewhat.

Let us define the Stanton number as

$$C_H = \frac{h}{\rho_e u_e} \quad 2.47$$

If we take this definition and substitute it into Equation 2.45, we can see that we have

$$q''_{conv} = \rho_e u_e C_H (i_r - i_w) \quad 2.48$$

The Stanton number, however, may vary depending on the surface mass blowing rate and the surface temperature. As such, we will rewrite Equation 2.48 in terms of a nominal Stanton number and a Stanton number correction:

$$q''_{conv} = \rho_e u_e C_{H_o} \left( \frac{C_H}{C_{H_o}} \right) (i_r - i_w) \quad 2.49$$

The Stanton number correction ( $C_{H_o}/C_H$ ) is composed of the product of a blowing correction and a hot wall correction:

$$\left( \frac{C_H}{C_{H_o}} \right) = \Omega_{blw} \Omega_{hw} \quad 2.50$$

which will themselves be defined later in this section.

### 2.3.2: Heat Transfer Coefficient Model

The heat transfer model to be used is one developed in the late 1950s by Fay and Riddell [14] and is a semi-empirical formula to calculate stagnation-point convective heat transfer. This model, along with another stagnation-point heating model developed by Sutton and Graves [13], has been widely used for precisely the kinds of calculations we wish to perform. We can say that the heat transfer coefficient is:

$$h = \frac{0.537a}{Pr^{0.6}} \left[ 1 + \left( \frac{D_x}{D_z} \right)^{\frac{1}{2}} \right]^{\frac{1}{2}} \left( \frac{du_e}{dx} \right)_{x=0}^{\frac{1}{2}} \left[ 1 + (Le - 1) \frac{i_{D_e} - i_{D_w}}{i_e - i_w} \right] \quad 2.51$$

where  $D_x$  and  $D_z$  are the diameters of curvature of the two axes of the surface,  $(du_e/dx)_{x=0}$  is a term that represents the derivative of the velocity along the surface coordinate, and the term on the right accounts for unequal diffusion. Fay and Riddell also define the parameter  $a$  in terms of the freestream stagnation and wall viscosities and densities as

$$a = (\rho_{st} \mu_{st})^{0.4} (\rho_w \mu_w)^{0.1} \quad 2.52$$

If we assume the Lewis number is one, which we must for equal mass and heat transfer coefficients (an assumption that will be made later in the section), the term on the right hand side of the function is equal to unity. Since the ablation model is only capable of one dimensional calculations, we will use the one-dimensional form of this model; thus we shall say  $D_x = D_z$  and that term is also equal to unity. We shall also assume throughout calculations that the Prandtl number is 0.71. Finally, then, we are left with an equation of the form

$$h = \frac{0.537\sqrt{2}}{\text{Pr}^{0.6}} (\rho_{st}\mu_{st})^{0.4} (\rho_w\mu_w)^{0.1} \left(\frac{du_e}{dx}\right)_{x=0}^{\frac{1}{2}} \quad 2.53$$

It is possible to approximate the velocity gradient in Equation 2.53 by the properties of the freestream flow and the shock. Crabtree, Dommett, and Woodley [16] note that it may be written

$$\left(\frac{du_e}{dx}\right)_{x=0} = \frac{1}{R_b} \sqrt{\frac{2(p_{st} - p_\infty)}{\rho_{st}}} \quad 2.54$$

where  $R_b$  is the radius of curvature of the body in question and the stagnation values (those with the subscript “st”) are the stagnation values evaluated in the freestream.

As such, then, we have a formula for the heat transfer coefficient of the form:

$$h = \frac{0.537\sqrt{2}}{\text{Pr}^{0.6}} (\rho_{st}\mu_{st})^{0.4} (\rho_w\mu_w)^{0.1} \left(\frac{1}{R_b} \sqrt{\frac{2(p_{st} - p_\infty)}{\rho_{st}}}\right)^{\frac{1}{2}} \quad 2.55$$

However, it is possible to simplify this somewhat further depending on how the shock is modeled. Consider the formula for freestream stagnation pressure:

$$p_{st} = p_\infty + \frac{1}{2}\rho_\infty u_\infty^2 \quad 2.56$$

If this is substituted into Equation 2.45, we can see that

$$\left(\frac{du_e}{dx}\right)_{x=0} = \frac{u_\infty}{R_b} \sqrt{\frac{\rho_\infty}{\rho_{st}}} \quad 2.57$$

If we are modeling a shock, it may be noted that the ratio  $\rho_\infty/\rho_{st}$  is the shock density ratio  $\epsilon$ , which will be explored later in the section. If a shock is not being modeled, the parameters may still be calculated as normal.

### 2.3.3: Blowing Correction

The blowing correction to the Stanton number accounts for the effect of mass blowing from the surface out into the boundary layer on the heat transfer coefficient. It was originally developed to calculate the impact of transpiration cooling, but has found some utility in ablation calculations. Following Kays and Crawford [23], we may write the blowing correction as

$$\Omega_{blw} = \frac{\Phi}{e^\Phi - 1} \quad 2.58$$

where

$$\Phi = 2\lambda \frac{\dot{m}''}{\rho_e u_e C_{H_o}} \quad 2.59$$

$\lambda$  is defined as 0.5 for laminar flow and 0.4 for turbulent flow. The mass flux,  $\dot{m}''$  is the net total mass flux into the boundary layer, including effects from surface convection, diffusion, and pyrolysis.

### 2.3.4: Hot Wall Correction

Following Amar [24] the hot wall correction may be given by

$$\Omega_{hw} = \left(\frac{\rho_{hw}\mu_{hw}}{\rho_{cw}\mu_{cw}}\right)^{0.1} \quad 2.60$$

where  $\rho_{hw}$  and  $\mu_{hw}$  are the hot wall density and viscosity, respectively, and  $\rho_{cw}$  and  $\mu_{cw}$  are the cold wall density and viscosity, respectively.

The “hot wall” state is the state of the wall as it is normally in the flow, with the temperature, composition, and pressure that that entails. The “cold wall” state is the state of the

wall with pressure and composition equal to the hot wall state, but at some reference temperature—in this case, 298.15 K.

### 2.3.5: Diffusive Mass Fluxes

Diffusive mass fluxes are calculated in much the same manner as the convective heat flux --- a transfer coefficient multiplied by a driving potential. Whereas in heat transfer the driving potential was either temperature or enthalpy (depending on the model), in mass transfer it is the mass fraction.

This means that, for a given species  $i$ , the diffusive mass flux  $J$  may be given by

$$J_i = h_m(Y_{i,w} - Y_{i,e}) \quad 2.61$$

where  $h_m$  is the mass transfer coefficient. This coefficient may be calculated differently depending on the model used. In the temperature-driven case of the user-input heat transfer model, the mass transfer coefficient may be estimated by  $h_m = h/C_p$ , where in our model the specific heat in question is taken at the wall. When heat flux is calculated with the Fay-Riddell enthalpy-driven model, the heat transfer coefficient is technically a mass transfer coefficient. We can therefore state that

$$h_m = \frac{C_M}{C_H} h \quad 2.62$$

where the ratio of mass transfer Stanton number to heat transfer Stanton number,  $C_M/C_H$  is assumed to be one. This fits with our assumption of a Lewis number of one when modeling the heat transfer coefficient. Since the mass transfer coefficient will be equal to the heat transfer coefficient, it will be subject to the same blowing and heat transfer corrections as the heat transfer coefficient.

## 2.4: SUPPLEMENTARY MODELS

### 2.4.1: Shocks

It is in our interest to model shocks for two reasons. The main reason is that shocks are very realistic for a number of the scenarios that we would like to simulate. Because it is difficult to measure values of parameters inside the shock, many experiments will give estimations of their freestream values rather than values from inside the shock layer. A shock will convert most of the kinetic energy of a flow into pressure and enthalpy, which, coupled with the potential chemical changes due to the temperature increase, will have a significant impact on the state of the flow inside the shock. For the purposes of the film transfer model being used, all of the heat and mass transfer takes place between the surface and the boundary layer edge, which is inside the shock layer. Not modeling the shock means that there is an ill-informed understanding of the conditions at the boundary layer edge. A second, more minor reason for modeling shocks is that our heat transfer model, as has been discussed earlier in this section, can potentially depend on the shock density ratio  $\epsilon$ , which is the ratio of the density of the post-shock gas to the pre-shock gas.

The shock model to be used is largely based on that of the Caltech Explosion Dynamics Laboratory's Shock and Detonation Toolbox, which is designed to work with Cantera to provide thermodynamic property and equilibrium calculations. While the SD Toolbox contains a number of shock models, the one to be used here is one where both the pre-shock and post-shock gases are in thermal and chemical equilibrium.

The system of equations used to calculate the post-shock conditions from the pre-shock conditions are the Rankine-Hugoniot relations. Anderson [25] gives the following relationships for enthalpy and pressure across a shock, respectively:

$$i_1 + \frac{1}{2}u_1^2 = i_0 + \frac{1}{2}u_0^2 \quad 2.63$$

$$p_1 + \rho_1 u_1^2 = p_0 + \rho_0 u_0^2 \quad 2.64$$

where the  $0$  and  $1$  subscripts represent the points before and after the shock, respectively. However, these two equations in and of themselves have too many unknowns to be able to solve the system. We will also use the ideal gas law (to relate pressure, temperature, density, and composition) and equilibrium calculations (to relate enthalpy, temperature, pressure, density, and composition) to fill out the system. The final system will be solved using Newton's method, and the mechanics of the actual code used to perform the computations will be described in more detail in the Code Development section.

### 2.4.2: Surface Pressure

Surface pressure is a required input to the material response model, and is kept constant throughout its calculations. As such, it will be calculated in the same manner regardless of the coupling. Since the gas-side model will be used specifically for stagnation-point computations, it makes sense to use the stagnation pressure as the surface pressure:

$$P_w = P_e + \frac{1}{2}\rho_e u_e^2 \quad 2.65$$

where  $P_w$  is the surface pressure and  $P_e$ ,  $\rho_e$ , and  $u_e$  are the pressure, density, and velocity, respectively, at the boundary layer edge. If wall blowing velocity were significant relative to the boundary layer edge velocity, it would subtract from the overall edge gas velocity. However, since the blowing velocity is small compared to the edge velocity, its contribution is neglected.

### 2.4.3: Equation of State

Gases on the flow side in general are assumed to be ideal (both inside and outside of the shock and boundary layers). We will therefore use the ideal gas law as our equation of state, which may be written:

$$P = \rho RT \quad 2.66$$

where  $R$  is the specific gas constant, which is dependent on the composition of the gas in question. We may write this dependency as

$$R = \frac{\bar{R}}{\sum x_i W_i} \quad 2.67$$

where the universal gas constant  $\bar{R}$  is defined as 8314.47215 J/kmol K, and  $x_i$  is the mole fraction of the  $i^{\text{th}}$  species.

### ***Mole and Mass Fractions***

The mole fraction of the  $i^{\text{th}}$  species, as noted previously, is denoted  $x_i$  and is given by

$$x_i = \frac{n_i}{n} \quad 2.68$$

where  $n_i$  is the number of moles of the  $i^{\text{th}}$  species. For an ideal gas, the mole fraction of the  $i^{\text{th}}$  species is directly related to the partial pressure of that species, or

$$P_i = x_i P \quad 2.69$$

The mass fraction of the  $i^{\text{th}}$  species is denoted  $Y_i$  and is given by

$$Y_i = \frac{\rho_i}{\rho} \quad 2.70$$

We can derive a relationship between the mole fraction and mass fractions by examining how they are defined. Noting that the number of moles of a species is simply the mass of that species divided by its molecular weight, we can take Equation 2.68 and say

$$x_i = \frac{n_i}{n} = \frac{m_i/W_i}{\sum m_i/W_i} = \frac{\rho_i V/W_i}{\sum \rho_i V/W_i} \quad 2.71$$

Noting from Equation 2.70 that the density of a species is the bulk density times the mass fraction, we can say

$$x_i = \frac{\rho V Y_i / W_i}{\sum \rho V Y_i / W_i} \quad 2.72$$

The bulk density and volume are not function of the species so they can be taken outside of the sum and canceled, leaving us with

$$x_i = \frac{Y_i/W_i}{\sum Y_i/W_i} \quad 2.73$$

#### 2.4.4: Gas Thermodynamic Properties

Correlations and their corresponding coefficients from NASA's Glenn Research Center are used to model thermodynamic properties in the gas phase. These correlations were originally made for use with NASA's Chemical Equilibrium and Applications (CEA) code, and are used in a wide range of applications. Using coefficients generated online by NASA's ThermoBuild [26] and correlation forms given by Sanford and McBride's CEA manual [27], enthalpy and specific heat of gases may be easily calculated for any temperature in the range from 200 to 20,000 K.

##### *Correlations*

From the CEA Manual [27] correlations for molar specific heat capacity and molar specific enthalpy are given (for an individual species) by

$$\frac{C_p^\circ}{R} = a_1 T^{-2} + a_2 T^{-1} + a_3 + a_4 T + a_5 T^2 + a_6 T^3 + a_7 T^4 \quad 2.74$$

$$\begin{aligned} \frac{i^\circ}{RT} = & -a_1 T^{-2} + a_2 T^{-1} \ln T + a_3 + a_4 \frac{T}{2} + a_5 \frac{T^2}{3} + a_6 \frac{T^3}{4} \\ & + a_7 \frac{T^4}{5} + \frac{b_1}{T} \end{aligned} \quad 2.75$$

Note, however, that these are the molar specific heat and molar specific enthalpy --- to get the mass specific enthalpy and specific heat, the gas constant above is should be the specific gas constant for the gas whose enthalpy or specific heat is being calculated.

Each gas has its own set of coefficients. These coefficients are put into tables and divided into three sets for different data ranges. One range is from 200 to 1000 K, the second is from 1000 to 6000 K, and the final range is from 6000 to 20000 K. It is important that all of these values be correct; when the author first received a version of the material response part of the ablation code, several of the parameters were wrong and led to incorrect calculations.

## ***Thermodynamic Properties of Mixtures***

Of course, gas mixtures are more important to consider in the current model than enthalpies or specific heats of individual gases. Mixture thermodynamic properties are defined in terms of the sum of the individual species' properties multiplied by their respective mass fractions. Bulk enthalpy, for example, taken at a specific temperature and composition, may be written

$$i = \sum_{i=1}^{N_s} i_i Y_i \quad 2.76$$

### **2.4.5: Transport Properties**

The one transport property required of the gas-side model is viscosity, which will be used in a number of other sub-models within this work --- namely, the convective heat transfer coefficient and the hot wall correction to the convective heat flux, as have been discussed earlier in this section. Viscosity is modeled using a form given in Kee [28] which is based on molecular gas dynamics calculations. For a given species, it takes the form

$$\mu_{gas} = 2.67 \times 10^{-6} \frac{\sqrt{WT}}{\sigma^2 \Omega^{(2,2)*}} \quad 2.77$$

where the leading factor is a combination of several universal constants (Boltzmann's number, Avogadro's number, etc.). In the denominator, the  $\sigma$  is the molecular diameter of the given species, the  $\Omega^{(2,2)*}$  is a reduced collision integral which is evaluated at some reduced temperature  $T^*$ .

This model is based on the Lennard-Jones potential for gases, and as such this model is dependent on parameters from that model. The reduced temperature,  $T^*$ , is calculated based on the Lennard-Jones potential well depth,  $\epsilon/k$ :

$$T^* = \frac{kT}{\epsilon} \quad 2.78$$

and the molecular diameter,  $\sigma$ , is also a parameter in the Lennard-Jones potential. Values for  $\epsilon/k$  and  $\sigma$  have been obtained from Poling's gas reference book [29], which in turn references Svelha [30], where any values not seen in Poling were found.

The reduced collision integral may be approximated by a correlation.

Kee [28] provides:

$$\Omega^{(2,2)*} = 1.0413(T^{*-0.1193}) + (T^* + 0.43628)^{-1.6041} \quad 2.79$$

### ***Transport Properties of Mixtures***

Estimating mixture transport properties is inherently more complicated than thermodynamic properties due to the need to account for molecular interactions. Bird, Stewart, and Lightfoot [31] present a mixture model, based on that of Wilke, for any transport property:

$$\mu_{mix} = \sum_{i=1}^{N_s} \frac{x_i \mu_i}{\sum_{j=1}^{N_s} x_j \Phi_{i,j}} \quad 2.80$$

where  $\Phi_{i,j}$  accounts for multi-species molecular interactions and may be written

$$\Phi_{i,j} = \frac{1}{\sqrt{8}} \left(1 + \frac{W_i}{W_j}\right)^{-1/2} \left[1 + \left(\frac{\mu_i}{\mu_j}\right)^{1/2} \left(\frac{W_j}{W_i}\right)^{1/4}\right]^2 \quad 2.81$$

## Chapter 3: Code Development

### 3.1: ABLATION CODE SOLUTION METHOD

The final result of the modeling effort in Chapter 2 is a nonlinear system of equations centered around the surface of the ablator. Because of the quasi-steady ablation model, which enables us to integrate over the length of the ablator, the only unknown parameters (at least, those that are not input) are at the surface. Therefore, the system of equations to be solved is formulated in terms of the surface temperature  $T_w$ , the blowing velocity  $v_w$ , and the composition at the surface denoted by the vector of gas-side surface mass fractions  $\vec{Y}_w$ .

The method to be used to solve this system of equations is the Newton-Raphson method, where a set of residual equations  $\mathbf{r}$  are minimized by finding successive better approximations of the solution vector  $\mathbf{x}$ ---if the exact solution is reached, all the residual equations will be equal to zero. In general, we can say

$$\mathbf{J}(\mathbf{x}_{n+1})(\mathbf{x}_{n+1} - \mathbf{x}_n) = -\mathbf{r}(\mathbf{x}_n) \quad 3.1$$

where as previously mentioned,  $\mathbf{x}$  and  $\mathbf{r}$  are the solution vector and vector of residual equations, respectively,  $\mathbf{J}$  is the Jacobian matrix, and the subscripts  $n$  and  $n + 1$  represent the current state of the solution and the state of the solution in the next iteration. Essentially, the system is solved for successive new values of  $\mathbf{x}$  (the  $\mathbf{x}_{n+1}$  terms) using the current solution and knowledge of the system of equations contained in the residual vector and Jacobian matrix.

The Jacobian is the matrix of the sensitivities of the residual equations to the solution vector. That is:

$$\mathbf{J} = \begin{bmatrix} \frac{\partial R_1}{\partial x_1} & \frac{\partial R_1}{\partial x_2} & \dots & \frac{\partial R_1}{\partial x_N} \\ \frac{\partial R_2}{\partial x_1} & \frac{\partial R_2}{\partial x_2} & \dots & \frac{\partial R_2}{\partial x_N} \\ \vdots & \vdots & \ddots & \vdots \\ \frac{\partial R_N}{\partial x_1} & \frac{\partial R_N}{\partial x_2} & \dots & \frac{\partial R_N}{\partial x_N} \end{bmatrix} \quad 3.2$$

The sensitivity of a residual equation to a solution parameter is expressed as the partial derivative of that equation with respect to the solution parameter. The first row contains the sensitivities of the first residual equation to the first through last solution variables. The second row is the same but for the second residual equation, and so on and so forth until the matrix is fully populated.

After the Jacobian matrix has been defined, the system can then be solved using linear algebra for new solution values  $\mathbf{x}_{n+1}$ . In the implementation being used in the ablation code, this is done using LU decomposition.

### 3.1.1: Residuals and Jacobian of the Ablation Code

To summarize, the residual equations to be solved in the ablation code as developed in Section 2.2:, are

$$J_i |_{g,w} + \rho_g v_w Y_{i,w} - \tilde{N}_i - \dot{m}''_{py} Y_{i,py} = 0 \quad (i = 1, \dots, N_s) \quad 3.3$$

$$\sum_{i=1}^{N_s} Y_i - 1 = 0 \quad 3.4$$

$$\rho_g v_w - \dot{m}''_C - \dot{m}''_{py} = 0 \quad 3.5$$

$$q''_{conv} - \sum_{i=1}^{N_s} i_i [\tilde{N}_i + \dot{m}''_{py} Y_{i,py}] + \alpha q''_{rad} - \epsilon \sigma T_w^4 + \rho_v v_s i_{f,v}^{\circ} = 0 \quad 3.6$$

where the carbon mass loss rate  $\dot{m}''_C$  may be written in terms of the sum of the reaction terms discussed in the Surface Chemistry subsection of Section 2.2.2.:

$$\dot{m}''_C = \dot{m}''_{O,C} + \dot{m}''_{O_2,C} + \dot{m}''_{N,C} + \dot{m}''_{C_3} \quad 3.7$$

and the gas phase density is given by the ideal gas law as discussed in Section.

In order to find the sensitivities in the Jacobian, we will need to calculate all of the derivatives of all of the terms in the residual equations with respect to all of our solution parameters. Since each residual equation is the sum of a series of terms, to find the Jacobian terms we may simply sum all of the derivatives of each term with respect to each solution

variable. The process of deriving the Jacobians will be performed in detail in Appendix C:, but a brief example will be shown here.

Take the energy balance equation:

$$R_{N_s+2} = q''_{conv} - \sum_{i=1}^{N_s} i_i [\tilde{N}_i + \dot{m}''_{py} Y_{i,py}] + \alpha q''_{rad} - \epsilon \sigma T_w^4 + \rho_v v_s i_{f,v}^\circ \quad 3.8$$

The partial derivative of this residual equation with respect to the surface temperature can be written

$$\frac{\partial R_{N_s+2}}{\partial T_w} = \frac{\partial}{\partial T_w} \left( q''_{conv} - \sum_{i=1}^{N_s} i_i \tilde{N}_i + \alpha q''_{rad} - \epsilon \sigma T_w^4 + \rho_v v_s i_{f,v}^\circ \right) \quad 3.9$$

We can therefore break it up into its component terms as

$$\begin{aligned} \frac{\partial R_{N_s+2}}{\partial T_w} = & \frac{\partial(q''_{conv})}{\partial T_w} - \frac{\partial(\sum i_i [\tilde{N}_i + \dot{m}''_{py} Y_{i,py}])}{\partial T_w} + \frac{\partial(\alpha q''_{rad})}{\partial T_w} \\ & - \frac{\partial(\epsilon \sigma T_w^4)}{\partial T_w} + \frac{\partial(\rho_v v_s i_{f,v}^\circ)}{\partial T_w} \end{aligned} \quad 3.10$$

The input radiative heat flux and the flux of enthalpy of the virgin material are not sensitive to the surface temperature, so those terms are zero. We then have

$$\frac{\partial R_{N_s+2}}{\partial T_w} = \frac{\partial(q''_{conv})}{\partial T_w} - \frac{\partial(\sum i_i [\tilde{N}_i + \dot{m}''_{py} Y_{i,py}])}{\partial T_w} - \frac{\partial(\epsilon \sigma T_w^4)}{\partial T_w} \quad 3.11$$

The sensitivity of the output radiative heat flux is simple to compute:

$$\frac{\partial R_4}{\partial T_w} = \frac{\partial(q''_{conv})}{\partial T_w} - \frac{\partial(\sum i_i [\tilde{N}_i + \dot{m}''_{py} Y_{i,py}])}{\partial T_w} - 4\epsilon \sigma T_w^3 \quad 3.12$$

Depending on the model used for the convective heat flux, the other terms may be difficult to model. In the case where the boundary layer model developed in Chapter 2: is not used, the convective heat flux is a constant input value and

$$\frac{\partial(q''_{conv})}{\partial T_w} = 0 \quad 3.13$$

In the case where we are using the boundary layer model, the derivative is evaluated by performing a finite difference operation with respect to the surface temperature. Therefore, we can say that

$$\frac{\partial(q''_{conv})}{\partial T_w} = \frac{1}{\Delta T_w} [q''_{conv}(T_w + \Delta T_w) - q''_{conv}(T_w)] \quad 3.14$$

where  $\Delta T_w$  is a small perturbation (in the code it is currently  $1 \times 10^{-7}$ ), and the convective heat flux is evaluated at the surface temperature and the surface temperature plus the perturbation.

### 3.2: ABLATION CODE PROCEDURE

In general, the process is relatively simple. A driver program reads some values from the input file to serve as boundary conditions for the flow, and passes these boundary conditions to the main function, `ablation1d`. This function then reads the remainder of the inputs from the file, which are numerous and include flow parameters, numerical controls, ablator material properties, chemistry model parameters, and all of the coefficients used to calculate thermodynamic properties. Significantly more detail on the input file will be given in Appendix A:.

Once all of the input is read and validated (to make sure that the inputs are physical), a guess of the solution is initialized based on the input parameters. The temperature and mass fraction guesses are obtained from the input values of “`T_nw`” and “`C_nw`”. Gas density near the wall is based on these values in conjunction with the ideal gas law, and this density is used along with an input guess of the recession rate to compute a guess of the final remaining solution parameter, the blowing velocity. The composition of pyrolysis gases is then computed---since these gases are assumed to be in frozen equilibrium at a specified pyrolysis temperature, they need only be computed once at the beginning of the simulation.

With a guess of the solution, the code then enters the Newton iterations described above. At every iteration step, the residuals are evaluated and the error of the iteration is set by taking the sum of the squares of the residual terms. The Jacobian is then computed. Finally, the system of equations is solved using LU decomposition and back-substitution. New values of the solution variables are not necessarily taken directly from this solve, however; the solution may be (and in many cases must be) under-relaxed. As such, we can say

$$Y_{i,w}^{n+1} = Y_{i,w}^n + \alpha \Delta Y_{i,w} \quad i = 1 \dots N_s \quad 3.15$$

$$v_w^{n+1} = v_w^n + \alpha \Delta v_w \quad 3.16$$

$$T_w^{n+1} = T_w^n + \beta \Delta T_w \quad 3.17$$

where the species mass fractions and the blowing velocity are under-relaxed by the same parameter  $\alpha$  and the temperature is under-relaxed by a different parameter  $\beta$ .

The error is then computed again (based on the sum of the squares of the residual equations) and if the error is found to be lower than a tolerance specified in the input file, the solution is said to be converged. The code then computes the output parameters of net mass flux into the flow and recession rate, and outputs these along with species concentrations and surface temperature.

### 3.3: PYROLYSIS GAS EQUILIBRIUM CALCULATIONS

The solution of the pyrolysis gas composition will be computed by Newton's method, as discussed in Section 3.1:. For the computation, we have  $N_s$  residual equations---rather than solving all  $N_s$  equilibrium relationships, it is easier to enforce the partial pressure constraint. Therefore, one compound species,  $N_2$ , will be neglected and used to absorb the differential in the partial pressures.

As such, the first  $N_{comp}$  residual equations, which are for the partial pressure of the compound species are

$$R_i = \ln(P_i^*) - \sum_{k=1}^K e_{k_i} \ln(P_k^*) - K_{p,i}(T) \quad 3.18$$

The next set  $K$  of residuals is for the conservation of elemental mass between the virgin ablator and the pyrolysis gas

$$R_k = Y_{k,v} - \sum_{i=1}^{N_{comp}} e_{k_i} Y_{i,py} \frac{W_k}{W_i} \quad 3.19$$

The final supplemental relation is the constraint on the partial pressures

$$R_{N_s} = P^* - \sum_{i=1}^{N_s} P_i^* \quad 3.20$$

The variables being solved for are the natural logarithms of the normalized partial pressures of the species in the flow,  $\ln(P_i^*)$ . As such, the sensitivities of the first  $N_{comp}$  residuals to the species in the set of compound species is

$$\frac{\partial R_i}{\partial \ln(P_j^*)} = \begin{cases} 0 & i \neq j \\ 1 & i = j \end{cases} \quad 3.21$$

The sensitivities to the elemental species may be written

$$\frac{\partial R_i}{\partial \ln(P_k^*)} = -e_{k_i} \quad 3.22$$

The sensitivities of the next set of residuals, those of the elemental species, may be written in terms of a number of derivatives of pyrolysis gas mass fractions. The mass fractions may be written in terms of the mole fractions as

$$Y_i = \frac{x_i W_i}{\sum_j x_j W_j} \quad 3.23$$

These mole fractions may then be converted to the partial pressure as  $x_i = P_i/P_{tot}$ . Substitution gives

$$Y_i = \frac{\frac{p_i W_i}{p_{tot}}}{\sum_j \frac{p_j W_j}{p_{tot}}} \quad 3.24$$

the total pressures cancel and we are left with

$$Y_i = \frac{p_i W_i}{\sum_j p_j W_j} \quad 3.25$$

where the partial pressures may be rewritten in their normalized form with no other changes since the reference pressure should cancel. The normalized partial pressure of each species may be written as the exponent of the natural logarithm of the normalized partial pressure, giving us

$$Y_i = \frac{\exp(\ln p_i^*) W_i}{\sum_j \exp(\ln p_j^*) W_j} \quad 3.26$$

Finally, the partial derivatives may be evaluated using the quotient rule as

$$\frac{\partial Y_k}{\partial \ln(P_i^*)} = \begin{cases} Y_{k,py} Y_{l,py} & k \neq l \\ Y_{k,py} (1 - Y_{k,py}) & k = l \end{cases} \quad 3.27$$

As such, we can define the Jacobian terms using these sensitivities and write

$$\frac{\partial R_k}{\partial \ln(P_j^*)} = -\frac{\partial Y_k}{\partial \ln(P_j^*)} - \sum_{l=1}^{N_{comp}} e_{kl} \frac{\partial Y_l}{\partial \ln(P_j^*)} \frac{W_k}{W_l} \quad 3.28$$

The sensitivities for the constraint equation may be written as

$$\frac{\partial R_{Ns}}{\partial \ln(P_i^*)} = -P^* \quad 3.29$$

### 3.3.1: Pyrolysis Gas Equilibrium Calculation Procedure

The procedure for computing the composition of the pyrolysis gases is roughly similar to the other processes outlined in this chapter. The computations begin with a guess of the  $\ln(P_i^*)$  terms, which are hard-coded into the ablation code and were the result of computations using the

CEA equilibrium code. The mole fractions of all of the individual species are determined from these guesses by dividing each term by the sum of the total, or

$$x_i = \frac{\ln(P_i^*)}{\sum_i \ln(P_i^*)} \quad 3.30$$

These mole fractions are then used, along with the pyrolysis temperature and a guess of the gas density (based on the given pressure and pyrolysis temperature) to get the partial pressures

$$p_i = x_i \rho \left( \frac{\bar{R}}{W_i} \right) T \quad 3.31$$

The natural logarithms of the partial pressures are taken, and the code begins Newton iterations, in the same manner as the main solver in the ablation code: residuals are computed according to the residual equations above, Jacobians are computed according to the residual sensitivities, and the linear algebra solve is performed using LU decomposition and backsubstitution. As in the main ablation solver, there is also an option for under-relaxation of the equilibrium calculation, and again the error between terms is computed by the sum of the square of the residuals after the iteration.

### 3.4: SHOCK CODE IMPLEMENTATION

The code used to compute the post-shock state of the flow gases, as was described in Section 2.4.1., is entirely separate from the ablation code. As mentioned previously, it is largely similar to the Shock and Detonation (SD) Toolbox [32] from Caltech, and it is dependent on the Cantera [33] package for thermodynamic property and equilibrium calculations.

The system of equations to be solved are the Rankine-Hugoniot relations, which in residual form may be written

$$H = i_1 + \frac{1}{2} u_1^2 - \left( i_0 + \frac{1}{2} u_0^2 \right) \quad 3.32$$

$$P = p_1 + \rho_1 u_1^2 - (p_2 + \rho_2 u_2^2) \quad 3.33$$

where  $H$  is the conservation of energy and  $P$  is the conservation of momentum, the subscript 1 represents the post-shock state and the subscript 0 represents the pre-shock state. In the above relationships, there are technically four unknowns – they may be reduced by the conservation of mass across a shock, which is written

$$\rho_1 u_1 = \rho_0 u_0 \tag{3.34}$$

The system is closed with two more relationships: the knowledge that the system is in thermal and chemical equilibrium after the shock sets the composition at a given temperature and pressure, and the assumption that the gases are ideal tells us that we can specify the state with any two independent thermodynamic variables.

The fact that the code uses Cantera is important, because the native variables that Cantera uses for equilibrium solves are temperature and specific volume, rather than enthalpy and pressure. Formulating the system in terms of these native variables helps the equilibrium calculations to converge much faster. It is also relatively simple.

The Newton-Raphson method will also be used to solve this system of equations. To formulate the system in terms of temperature and specific volume, all we have to do is say that the solution vector  $\mathbf{x}$  is

$$\mathbf{x} = \begin{bmatrix} T_1 \\ v_1 \end{bmatrix} \tag{3.35}$$

and the Jacobian is

$$\mathbf{J} = \begin{bmatrix} \frac{\partial H}{\partial T_1} & \frac{\partial H}{\partial v_1} \\ \frac{\partial P}{\partial T_1} & \frac{\partial P}{\partial v_1} \end{bmatrix} \tag{3.36}$$

If we evaluate the derivatives in the Jacobian by finite difference, there is no need to completely reformulate the residuals. Since the thermodynamic state of both gases is considered known at every iteration step, it is simple to get the enthalpy and pressure from a gas with known temperature and specific volume at equilibrium. Cantera, in fact, is built for this purpose---once

the state of a gas is specified, it is possible to obtain any thermodynamic property of that gas using a simple function call.

### 3.4.1: Shock Code Procedure

First, the state of the pre-shock gas is input. With Cantera, this is generally done as an input velocity, temperature, pressure, and composition. The equilibrium composition of the pre-shock gas (holding temperature and pressure constant) is then found using Cantera's equilibrium solver.

A first guess of the state of the post-shock gas is made by assuming that the post-shock specific volume is one-fifth of the pre-shock specific volume. The post-shock pressure is then calculated using

$$p_1 = p_0 + \rho_0 u_0^2 \left[ 1 - \left( \frac{v_1}{v_0} \right) \right] \quad 3.37$$

which is simply a rearrangement of the conservation of momentum across a shock with the conservation of mass substituted in. The post-shock temperature is then computed from the post-shock pressure and density using the combined gas law:

$$T_1 = p_1 v_1 \left( \frac{T_0}{p_0 v_0} \right) \quad 3.38$$

Finally, the guess of the post-shock state is completed by finding the equilibrium composition of the post-shock gas while holding temperature and specific volume constant. It is at this time that the pressure and enthalpy are evaluated as well.

When a guess is obtained, the Newton iterations of the system begin. The residual equations  $H$  and  $P$  are evaluated at the current state of the post-shock gas. The temperature is then perturbed by  $\Delta T_1 = 0.01 T_1$ , the equilibrium state at the new temperature is computed, and the residuals are re-evaluated. The Jacobian terms are then computed using finite difference:

$$\frac{\partial H}{\partial T} = \frac{1}{\Delta T_1} [H(T_1 + \Delta T_1) - H(T_1)] \quad 3.39$$

$$\frac{\partial P}{\partial T} = \frac{1}{\Delta T_1} [P(T_1 + \Delta T_1) - P(T_1)] \quad 3.40$$

The exact same method is employed to compute the sensitivities of the residuals with respect to specific volume. The volume perturbation is  $\Delta v_1 = 0.01v_1$ , the equilibrium state at the new volume is computed, and the derivatives are computed accordingly by finite difference.

Since the Jacobian is small and easy to invert, new values of the solution variables  $T$  and  $v$  are computed by multiplying the inverse of the Jacobian by the residual. The difference between the old and new values are given by

$$T_1^{n+1} - T_1^n = \frac{\left[ -H \left( \frac{\partial P}{\partial v_1} \right) + P \left( \frac{\partial H}{\partial v_1} \right) \right]}{\det \mathbf{J}} \quad 3.41$$

$$v_1^{n+1} - v_1^n = \frac{\left[ H \left( \frac{\partial P}{\partial v_1} \right) - P \left( \frac{\partial H}{\partial T_1} \right) \right]}{\det \mathbf{J}} \quad 3.42$$

where the determinant of the Jacobian is

$$\det \mathbf{J} = \frac{\partial H}{\partial T_1} \left( \frac{\partial P}{\partial v_1} \right) - \frac{\partial P}{\partial T_1} \left( \frac{\partial H}{\partial v_1} \right) \quad 3.43$$

After new values of the temperature and specific volume are computed, the equilibrium state of the gas is calculated and the process begins again. This is done until the error, defined in this problem as  $T_1^{n+1} - T_1^n$  or  $v_1^{n+1} - v_1^n$  (whichever is larger), reaches a value of  $1 \times 10^{-8}$ .

When the system is considered to be converged, the equilibrium state of the gas is computed and the relevant parameters for input to the ablation code are output. These parameters are post-shock temperature, post-shock pressure, shock density ratio, post-shock velocity, and post-shock gas composition.

### 3.4.2: Shock Code Coupling to the Ablation Code

The shock code must interface with the ablation code, and does so through its inputs. The interaction can be seen below in Figure 3.1. Various freestream parameters (velocity and enough information to specify the thermodynamic state) in input to the shock code. Many outputs of the

shock code, including the boundary layer edge velocity, temperature, pressure, composition, and the shock density ratio, are used as inputs to the ablation code, which may then compute normally. It must be noted, however, that currently this coupling is achieved through Python scripts and the two codes are completely separate.

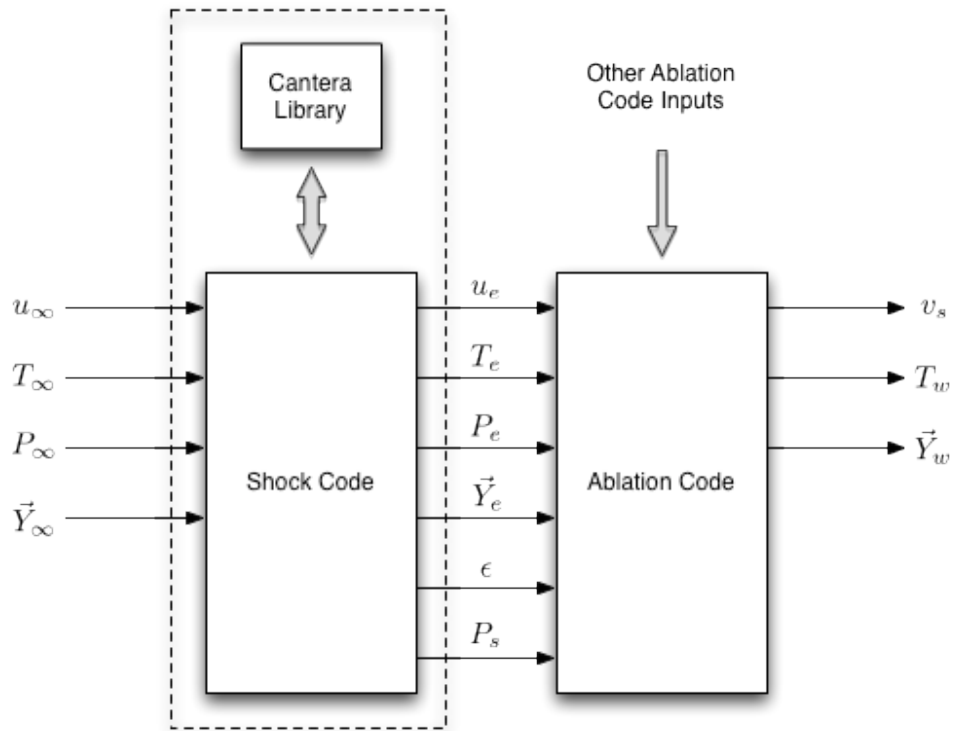


Figure 3.1: Coupling of the shock code with the ablation code.

## Chapter 4: Model Validation and Code-to-Code Comparison

Validation is one of the most important aspects of code development; a model that is written but not validated is essentially useless, as its results may or may not have any relation to reality. Models must be compared to reality by way of experiments---which may or may not do a particularly good job of representing realistic use scenarios. We may also use a more sophisticated code to represent a “truth” that can be compared to, in the event that experiments are unavailable or lacking in data. By going through this process, we can be assured of precisely which regimes the code will work well in, and in which regimes we are extrapolating.

The validation process is best performed hierarchically, starting with the independent validation of single-physics submodels and gradually moving up into the fully-coupled system simulation. This ensures that the submodels are adequate and helps to eliminate sources of error from the fully coupled system validation. To do this we need to pick an output quantity that is most relevant to what we are interested in using the code to compute. In the case of the ablation code being developed here, the quantity of interest (QoI) is the ablation rate,  $v_s$ . We can also define other QoIs depending on the situation and comparison that we are trying to make---a good QoI for comparison in some situations is the peak heat flux, if for some reason the ablation rate is unavailable.

In this section, the ablation model will be validated with respect to arcjet experiments, and the coupled code will be compared to the Chaleur ablation code developed at Sandia National Laboratory.

### 4.1: SUBMODEL VALIDATION

All of the submodels used---most importantly, those for modeling specific heat, enthalpy, entropy, viscosity, and convective heat transfer---are widely used. They are all from the literature

and have essentially been validated over the course of their development and usage. For information about how these models have been validated and under what conditions they are valid, one must simply look at the papers where the models are defined. These references for each of the submodels are given in the relevant sections in Chapter 2:, where the models are laid out.

## 4.2: SHOCK CODE COMPARISON

To help validate the shock model, it is insufficient to look at the regular NACA shock tables because while these exist for both perfect and imperfect gases, they do not consider equilibrium compositions on both sides of the shock. As such, we will look at calculations performed by Wittliff and Curtis [34], who computed normal shock wave parameters in equilibrium air. The calculations performed are at a range of standard altitudes (with their own given temperatures, pressures and densities. Table 4.1 gives a number of values of the expected and computed shock ratios in air (which we say is composed of  $Y_{O_2} = 0.233$  and  $Y_{N_2} = 0.767$ ) at sea level for different velocities.

Table 4.1: Computed results of the shock code with values from Wittliff and Curtis [34].

Velocity (m/s)	Shock Density Ratio		Shock Pressure Ratio		Shock Temperature Ratio	
	Expected	Computed	Expected	Computed	Expected	Computed
609.6	0.4301	0.4253	0.2810	0.2800	0.6532	0.6582
914.4	0.2766	0.2771	0.1585	0.1208	0.4350	0.4359
3048	0.1299	0.1297	0.01013	0.01016	0.07911	0.07944

The shock code does a reasonably good job of approximating the answers from the literature, though there are some small differences. Most differences can likely be attributed to

the gas composition in the shock code, which as mentioned previously is assumed to compose entirely of molecular nitrogen and molecular oxygen (before being brought to equilibrium at a given temperature) and therefore omits other important species, such as argon.

### **4.3: ABLATION CODE MODEL VALIDATION WITH ARCJETS**

Arcjets are some of the most commonly used experiments to help characterize the material response of ablators. This is because they generally do a good job of achieving the heating regimes commonly encountered in hypersonic reentry. Though they do not exactly replicate the flow field in terms of chemistry, radiation, and shocks, they have been used extensively for testing over the course of ablation research. There are a number of issues associated with the comparison of computations to arcjet experiments, and these will be discussed later in this section. First, though, it is important to understand how arcjets work.

The basic idea behind an arcjet is relatively simple --- an electric arc is struck between an anode and a cathode, and air is passed through the arc in order to heat it. In many modern arcjets, there is a long region where the arc and the air are constricted to flow together through a narrow tube such that electrical energy is transmitted to the flow more efficiently. The constrictor section (where the arc and the flow are constrained to share the same space) and the downstream electrode are cooled with a water-cooling system, and the arc attachment location is rotated around the downstream electrode with a variable magnetic field so as to keep the net heating load to any one point on the electrode down. After the flow passes the downstream electrode, the arc-heated air then flows through a settling chamber, where some of the ions are allowed to recombine, and out through a converging/diverging nozzle.

The resulting flow from the nozzle can be difficult to characterize for a number of reasons. A major problem is that the flow in the constrictor section is essentially a plasma, with extremely high levels of ionization and dissociation. This flow is difficult to measure, characterize, and model, making it even more difficult to determine all of the states that follow in

the settling chamber, nozzle, and test section. The flow coming out of the constrictor section is theorized to be in thermal and chemical nonequilibrium, and this theory carries through to the downstream segments. The degree of nonequilibrium is somewhat poorly understood, and almost certainly changes over the length of the arcjet. Measurements can characterize the pressure and enthalpy of the flow, but it may be very difficult to learn just how far the flow is from equilibrium based on simple measurements.

#### **4.3.1: Issues with Arcjet Comparison**

The main issues with comparison of computations to arcjets are related to the fact that arcjet flow is extremely difficult to measure and characterize. Even in well-instrumented experiments, like those performed by Covington [35], the measurements are made more with an eye towards experimental replication rather than computational simulation. As a result, the boundary conditions used when performing a simulation of a test article in an arcjet must be based on correlations using measurements far upstream of the test section and assumptions about the flow conditions that may or may not be correct. For example, many arcjet papers cite heat fluxes that are measured while putting a test article into the flow very briefly; this may be a good way to ensure that arcjet experiments are self-consistent, but these values are somewhat misleading for computationalists.

Further, arcjet test-section flows tend to be highly nonequilibrium flows; the methods laid out here for calculating the flow across the shock and the heat and mass transfer to the surface of the ablator both assume that the flow is in thermal and chemical equilibrium throughout. This discrepancy could potentially lead to significant differences between the computational result and the experimental result.

It is also assumed in the ablation code that the ablation rate is steady. This is clearly not the case at the beginning of any ablation process, as it will take some time for an ablator to reach steady-state. However, for the short experimental durations experienced in arcjets, it is uncertain as to whether or not the ablation is ever steady---this depends significantly on the material of

interest and the flow conditions in the experiment, and must be evaluated on a case-by-case basis.

Additionally, it is assumed in this code and many others that the ablation taking place is one-dimensional. In many arcjet experiments, this does not seem to be the case, especially for smaller ablator samples and at higher heating rates, where the effects of flow around the edges of the test article become more important.

### **4.3.2: Arcjet Enthalpy Determination Methods**

There are several ways to determine the enthalpy at various points along the length of an arcjet, running the gamut from simple bulk energy balances to full CFD simulations. This can be a fairly significant issue because different calculations may lead to substantial differences in the value of the enthalpy determined. As well, these relationships should theoretically calculate different values of enthalpy at different points in the flow, though some papers seem to treat them as mostly interchangeable.

#### ***The Energy Balance Method***

Fletcher [36] discusses a simple first-law energy balance to compute the average enthalpy of the flow immediately after leaving the downstream electrode. Essentially, the amount of energy in the flow is assumed to be all of the energy used to generate and sustain the electrical arc minus the amount of heat carried away from the constrictor and electrodes by the water cooling system. Performing this simple energy balance yields the equation

$$\dot{m}i_{avg} = VI - \dot{m}c_p(\Delta T_{on} - \Delta T_{off}) \quad 4.1$$

where  $\dot{m}$  is the bulk mass flow rate of air through the arcjet,  $i_{avg}$  is the average bulk enthalpy of the air at the constrictor exit,  $VI$  is the total power input to the arcjet, and the  $\Delta T$  terms represent the temperature differential across the cooling system when the arcjet is on and off, so as to account for friction heating of the coolant. However, while the formula does account for the energy removed from the flow to the water cooling system, it does not account for any

inefficiencies in the energy transfer between the arc and the flow. As such, it should be seen as an upper bound on the flow enthalpy.

### ***The Sonic Throat Method***

The sonic throat method was developed by Winovich [37] specifically to help evaluate the performance of electric arc air heating systems. It uses as its basic principle the idea that for a given thermodynamic state there is a unique value of the sonic mass flow from a reservoir. Known values of pressure and mass flow rate may then uniquely determine the value of the enthalpy. Choked, one-dimensional, equilibrium flow through a nozzle may be represented by

$$\frac{\dot{m}}{Ap_0} = \frac{\sqrt{2i_0}}{RT_0} \left[ \frac{\rho^*}{\rho_0} \left( 1 - \frac{i^*}{i_0} \right)^{\frac{1}{2}} \right] \quad 4.2$$

where  $A$  is the cross-sectional area of the throat, the subscript 0 refers to stagnation conditions in the reservoir leading up to the nozzle, and the superscript \* refers to the conditions at the sonic point of the throat.

There are simplified versions of the above equation for perfect and imperfect gases, using familiar parameters from hypersonics such as the ratio of specific heats,  $\gamma$ , and the specific gas constant  $R$ . For a real gas, however,  $\gamma$  and  $R$  will vary with temperature and pressure and there is no simple solution to the above equation. As such, an experimental correlation has been developed relating the left hand side of Equation 4.2 directly to the enthalpy:

$$\frac{\dot{m}}{Ap_0} = \frac{C}{i_0^{0.397}} \quad 4.3$$

where the constant  $C$  depends on the system of units being used (Winovich gives 280 for Imperial units).

It is important to note that these sonic throat relationships give the total enthalpy *before* the flow goes through the nozzle rather than afterwards. However, if the nozzle is isentropic, the

total enthalpy will be conserved across the nozzle and the total enthalpy in the test section will be equal to the total enthalpy in the region before the nozzle.

### ***Enthalpy Based on Heat Flux***

Zoby [12] developed a method for computing stagnation-point heat flux driven by enthalpy with a simple, experimentally derived, heat transfer coefficient that changes depending only on the composition of the gas. The form of the convective heat flux is given by

$$q''_{conv} = \sqrt{\frac{p_s}{R_{eff}}} \left( \sum_i \frac{C_i}{K_i} \right)^{-1} (i_s - i_w) \quad 4.4$$

Where  $C_i$  is the concentration of the  $i^{\text{th}}$  gaseous species,  $K_i$  is its associated “heat transfer constant”,  $R_{eff}$  is the effective radius of curvature of the body in the flow,  $p_s$  is the stagnation pressure,  $i_s$  is the stagnation enthalpy and  $i_w$  is the enthalpy at the wall.

As an example of how this could be used in an arcjet, Park [38] uses this technique to compute the “centerline enthalpy” for a test article and presents it as

$$i_c = \frac{q}{\dot{m}} \sqrt{\frac{R}{p_o}} \left( \frac{\dot{m}_A}{K_A} + \frac{\dot{m}_a}{K_a} \right) \quad 4.5$$

where in this relation it is considered that there is one heat transfer constant for air and another for argon; the ratio  $\dot{m}_i/\dot{m}$  is the mass fraction of that species in the flow, and argon is often injected into the flow stream of arcjets.

### **4.3.3: Comparison to Covington**

Despite the challenges laid out over the course of this section, efforts were made to validate the fully-coupled code with respect to arcjet tests performed by Covington, et al. [35], who tested a range of models using phenolic impregnated carbon ablator (PICA) material in NASA's Interaction Heating Facility (IHF) over a variety of heat fluxes.

The issues in experimental validation of ablation codes with respect to arcjet experiments became immediately apparent as soon as the process was undertaken. No information is given in

the Covington paper about the flow in the arcjet itself; all measurements are made relative to the test articles. Heat flux and pressure measurements are given, but they are not well detailed---it is mentioned only that the heat flux measurements were made using copper slug calorimeters and water-cooled Gardon gauges, and that the pressure measurements were made with pitot probes. These measurements were used with the Zoby [12] heat flux correlations to evaluate the enthalpy of the flow. The effective radii of curvature for the relatively cylindrical test subjects used by Covington were evaluated using an expression by Zoby and Sullivan [39], which says that this effective radius is 3.15 times the base radius of the cylinder.

Not knowing anything about the flow presents an interesting challenge for computations. However, Park, et al. evaluated the flow characteristics of the IHF using a variety of methods [38]. The results of this paper give a good starting point for the computation to be performed herein, and insight into the way that calculations and measurements are made in arcjet facilities.

First, the Park paper evaluates the flow using the one-dimensional nozzle code NOZNT to calculate the freestream conditions in the test section of the IHF based on assumed values of the settling chamber enthalpy. With a settling chamber enthalpy of 44.5 MJ/kg, Park was able to calculate a test section total enthalpy of 40.6 MJ/kg. The enthalpy is then computed with the aforementioned energy balance, sonic throat, and heat flux techniques using measurements made throughout the arcjet facility. These computations resulted in enthalpies of 28.7, 28.83, and 30.5 MJ/kg.

In choosing an enthalpy to be used for the freestream flow in our ablation calculations, it was important to decide which would be the most appropriate based on the models underlying the enthalpy calculations. The NOZNT calculation presented seems to be based largely on assumptions about the arcjet facility, though it is consistent with some experimental observations and measurements discussed later in the paper. The steady energy balance method should give the enthalpy at the constrictor exit, which is not what we are interested in, and the heat flux method should give the value at the boundary layer edge inside the shock layer of the ablator, as discussed earlier in this paper. The sonic throat method, however, does give us the stagnation

enthalpy in the test section. This is close to what is desired, but in order to compute the state of the gas in the test section, enthalpy (not stagnation enthalpy) is needed.

As such, an amalgamation of measurements and computations from the Park paper was used to find the freestream conditions of the IHF for our computational purposes. The enthalpy in the flow is evaluated by the definition of the stagnation enthalpy, rearranged to say

$$i_{\infty} = i_{hf} - \frac{1}{2}u_{\infty}^2 \quad 4.6$$

where  $i_{hf}$  is the heat flux calculation of enthalpy performed by Park and  $u_{\infty}$  is the velocity calculated by NOZNT in the test section. They are 28.83 MJ/kg and 5890 m/s respectively, resulting in a freestream enthalpy of 11.48 MJ/kg. To set the state of the system, the NOZNT-computed pressure of 2.517 kPa is used. Assuming that the gas in the flow is entirely air at equilibrium, the temperature is found to be 4803 K

Then, using the method described in Section 3.4:, with a slightly modified procedure due to the fact that the inputs are enthalpy and pressure rather than temperature and density, the effects of the shock on the gas were calculated. The boundary layer edge, as per the assumptions made in the shock computation process, is also at equilibrium. Across the shock, the temperature increases to 15,256 K, the pressure increases to 33.54 kPa, and the velocity decreases to 2210 m/s. The gas composition after the shock, as would be expected of air at equilibrium at such a high temperature, is almost entirely composed of dissociated nitrogen and oxygen. The shock density ratio,  $\epsilon$ , is found to be 0.3753. The surface pressure, which is computed as the stagnation pressure at the boundary layer edge, is calculated to be 42.86 kPa.

One unresolved question, though, is the effective radius of curvature to be used. From Covington, there are a number of different sized models used; for each of these models, a surface pressure is given. Because the surface pressure calculated herein is closest to that of the 10.16-cm diameter model with a cold-wall heat flux of 580 W/m<sup>2</sup>, that is the diameter chosen to calculate the effective radius of curvature for the simulation, which was found to be 0.16002 m.

The ablation code was then run with the above input conditions. For material properties, the ablation code used the averages of those given for PICA in the Covington paper, since material properties in the ablation code are assumed to be independent of temperature. The results of this calculation, along with average results from Covington, are given in Table 4.2.

Table 4.2: Comparison of results from the ablation code with the average of the results obtained from comparable experiments by Covington [35].

Parameter	Covington (Average)	Ablation Code
Recession Rate (mm/s)	0.1779	0.1509
Surface Temperature (K)	2650	3035
Heat Flux (W/cm <sup>2</sup> )	580 (cold wall)	373.6

Though the ablation rate calculation is surprisingly close to the average from Covington (approximately a 15% difference), the results in Table 4.2 must be viewed with a healthy dose of skepticism. The comparison of arcjet experiment and computation is still very much problematic (as discussed previously), and in particular these computations were made using assumed freestream values that could be completely different from those that actually occurred in the experiment. Further, the heating times throughout the experiments vary significantly---from as low as 10 seconds to as high as 86 seconds---and may or may not be at steady state depending on the experiment in question. As well, it can be seen in the experimental data that the bondline temperature, which for our intents and purposes represents the back of the ablating material, of one of the models in question (7B) is changing with time shortly after the model is placed in the stream. This invalidates our assumption that the backface temperature is constant throughout the experiment, and is a strong indicator that the experiment would not reach steady state.

As such, though the results in Table 4.2 are promising, we must find another method to help understand how the ablation code performs in comparison to a baseline scenario. Another

code, Chaleur, was chosen for this. The capabilities and performance of the ablation code and Chaleur will be compared and contrasted over a range of conditions, including with both nondecomposing and decomposing ablators.

#### 4.4: COMPARISON OF MODELS USED IN CHALEUR AND THE ABLATION CODE

Chaleur is the ablation code developed by Adam Amar and Ben Blackwell [6] at the Sandia National Laboratory. It performs an unsteady calculation using a control-volume finite-element method (CVFEM) to obtain the ablation rate as well as in-depth profiles of temperature and solid density and their evolution in time. Though the solution method is completely different from the ablation code being developed here, they are intended to be used for similar computations and can both solve for the same quantities of interest, namely the ablation rate and peak heat flux (as mentioned earlier in the chapter).

Arguably, comparison to Chaleur is not validation. Though Chaleur is somewhat more sophisticated than the ablation code, especially in terms of the in-depth decomposition model it uses, it has a large number of simplifying assumptions and may be just as inaccurate as the ablation code. As such, the purpose of this section is more to understand and analyze the abilities of the ablation code with respect to a code that has known capabilities.

When performing this comparison, it is important to understand how the two codes differ and how they are similar. One significant way that Chaleur differs from the ablation code developed in this paper is that Chaleur is heavily dependent on thermochemistry tables to calculate the ablation rate and pyrolysis gas production rate. Thermochemistry tables contain tabulated values for the non-dimensionalized char mass loss rate and pyrolysis mass loss rate,  $B'_c$  and  $B'_g$ , at different values of the surface temperature and surface pressure.

Recall that the total mass loss rate from the ablator is

$$\dot{m}'' = \dot{m}''_c + \dot{m}''_{py}$$

where the char mass loss rate is

$$\dot{m}_c'' = \rho_c v_s$$

and the pyrolysis mass loss rate is

$$\dot{m}_{py}'' = \rho_g v_w \left( 1 - \frac{\rho_{ch}}{\rho_v} \right)$$

Knowing this,  $B_c'$  and  $B_g'$ , can be written

$$B_c' = \frac{\dot{m}_c''}{h_m} = \frac{\rho_c v_s}{h_m} \quad 4.7$$

$$B_g' = \frac{\dot{m}_{py}''}{h_m} = \frac{\rho_g v_w \left( 1 - \frac{\rho_{ch}}{\rho_v} \right)}{h_m} \quad 4.8$$

In general, these tables have historically been computed using the Aerotherm Chemical Equilibrium (ACE) code, which is able to perform an open-system equilibrium calculation using the species at the surface, in depth, and in the gas phase to find the mass loss rates. This contrasts with the current code, which computes the surface recession rate based on chemical kinetics and the pyrolysis gas mass flux based on that surface recession rate. Because of this, it may be difficult to directly compare the two codes in some regimes. In a kinetically-controlled regime, where the reaction kinetics are slow compared to the diffusion of species to and from the surface, the ablation code will do a much better job of predicting the ablation rate; Chaleur is simply not equipped to handle that kind of calculation. However, in a diffusion-controlled regime, where the kinetics are fast compared to the diffusion of species to and from the surface, the two codes should produce similar results. The same is true in a sublimation-controlled regime, where the model used in the ablation code is more similar to that of Chaleur.

Another way that the two codes differ is that Chaleur performs an unsteady computation. The ablation code in this paper is a quasi-steady code, which, as discussed previously, means that the surface is assumed to be receding at a constant rate. As such, it is important that Chaleur

reaches this quasi-steady condition before we try to draw any comparisons between it and the ablation code. This is done by computing the normalized error in the ablation rate

$$\text{error} = \frac{v_s^n - v_s^{n-1}}{v_s^n} \quad 4.9$$

where  $n$  is an index to represent the time step. When the error is below a certain bound (in our case,  $1 \times 10^{-5}$ ) the solution is said to have reached steady state and the desired parameters are output.

#### **4.4.1: Comparison Method for Chaleur**

To ensure that comparisons in different heating and reaction regimes are done in a manner that is self-consistent, a pre-defined method for performing computations with the ablation code and Chaleur has been developed. Developing a consistent method also helps when automating the process, which has been done here using Python scripts. The method is shown diagrammatically below in Figure 4.1, and explored in more detail in the following paragraphs.

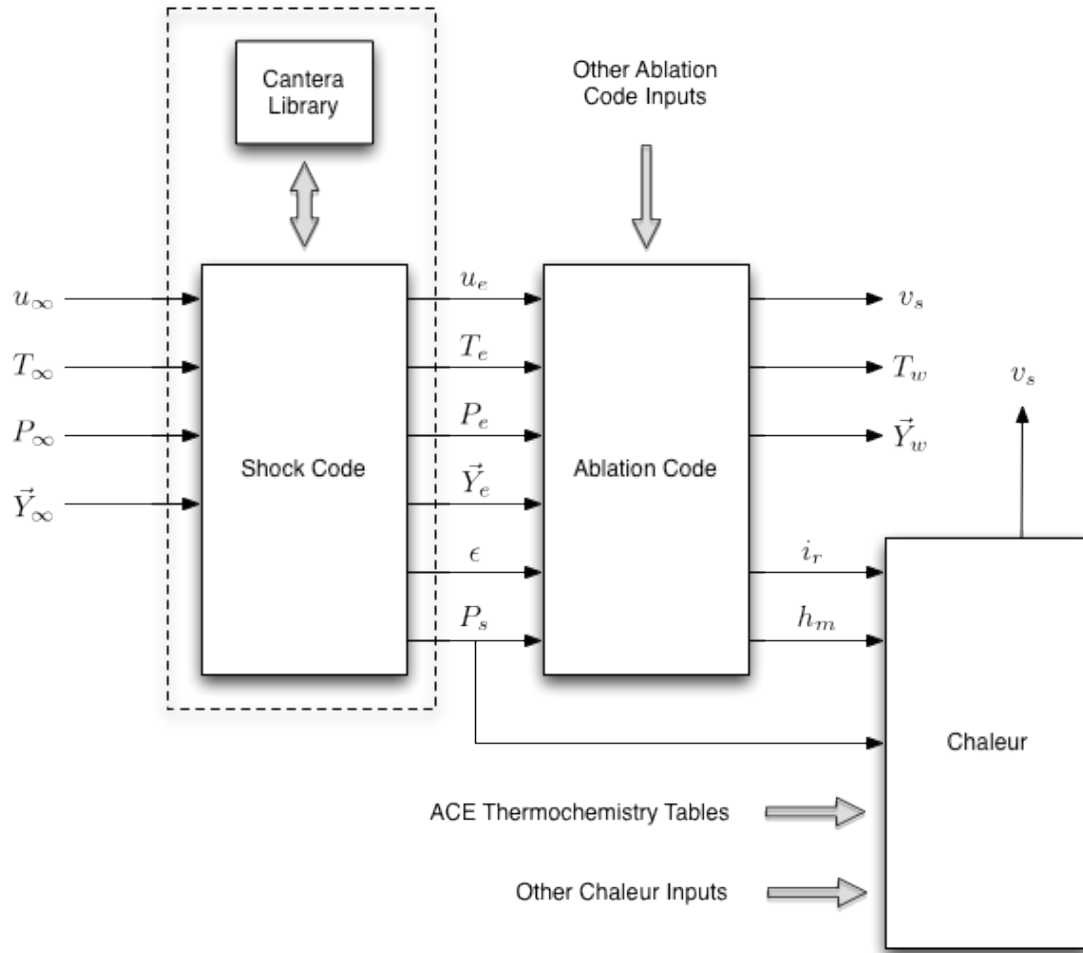


Figure 4.1: Method for carrying out computations of both Chaleur and the ablation code.

We first take our input freestream parameters and evolve them across the shock using the code discussed in Section 2.4.1: and Section 3.4:. The appropriate parameters are then passed to the ablation code as inputs, as described previously when discussing the implementation of the shock code.

The ablation code, with its flow-side inputs determined based on the regime of interest, is then run. When a solution is reached, the ablation code writes its normal output of gas phase composition, ablation rate, and temperature. However, it also writes out a number of parameters--the convective heat transfer coefficient, the recovery enthalpy, the surface pressure, and the

boundary layer edge velocity---that are used as inputs to Chaleur. The reason for calculating Chaleur's inputs in this manner is to ensure that the two codes are, in fact, performing the same calculation.

Chaleur has a wide variety of options for transferring heat to the ablating surface. There is an aeroheating model that is very similar to the one being used here, but there are also models for convection (like the simple heat transfer model discussed in Section 2.3.1:), constant heat flux input models, radiation models, and others. The boundary conditions applied to try to ensure that Chaleur and the ablation code are solving the same problem are the aeroheating condition and the far-field radiation condition. The radiation condition is of the form

$$q''_{rad,out} = \sigma \epsilon (T_w^4 - T_{ff}^4) \quad 4.10$$

where  $T_{ff}$  is the far-field temperature that the surface radiates out to, which is an input in Chaleur. In order to keep Chaleur the same as the ablation code, this is set to zero. The other heating boundary condition used is the aeroheating flux, which takes the form

$$q''_{aero} = h_m (i_r - i_\infty) \quad 4.11$$

and has the ability to compute hot wall and blowing corrections as the ablation code does. That said, it is important to note that at least in the version of Chaleur being used, this is different from how it is specified in the Chaleur user's manual. In the user's manual, the aeroheating flux is said to be computed as

$$q''_{aero} = \rho_e u_e C_H (i_r - i_\infty) \quad 4.12$$

However, in the actual code it is computed as in Equation 4.11 above---the  $h_m$  is what is input as  $C_H$ , rather than being multiplied by the boundary layer edge density and velocity.

With the output from the ablation code computed, it is converted into engineering units and used as input to Chaleur. Chaleur is then run with the inputs described above, and its output is converted back into SI units. The Chaleur output is checked to see if it has reached steady state

in the allotted time (maximum time is an input variable). If it has, the steady values are output and compared to those of the ablation code.

While other methods than the one just described were considered, they turned out to be unfeasible. The ablation code, with its coupled boundary layer, is incapable of handling a constant input heat flux---the diffusion model requires a heat transfer coefficient and boundary layer edge values of mass fractions to be input. The convective heat flux model in Chaleur is incompatible with the ablation module, so comparison through that method is impossible as well.

#### **4.4.2: Initial Chaleur Comparisons**

The ablation code and Chaleur are first compared for scenarios involving graphite ablators, which do not experience in-depth decomposition. This makes initial comparisons much simpler and allows us the ability to evaluate the differences in the surface reactions without them being distorted by the effects of the pyrolysis gases.

As discussed earlier, Chaleur performs its mass loss computations using  $B'$  tables. These tables are generally represented by curves where the surface temperature varies and the surface pressure is held constant. Despite this, we will attempt to compare the two codes under realistic conditions: the method used to compute results will be that discussed previously, where input conditions are evolved across a shock and input to the ablation code, and the heat transfer coefficient and recovery enthalpy computed by the ablation code are used as inputs to Chaleur. The results of the two codes will then be compared.

The first cases examined are based around the freestream conditions used by Chen and Milos [8] for their computations involving a graphite ablator. The specific values used are given in Table 4.3, which shows that the freestream flow is composed of molecular nitrogen, atomic oxygen, and nitrogen. While Chen and Milos do not explicitly give the pressure used in their simulation, they give enough information to compute the pressure used, which is taken as 1671 Pa. The temperature used is 1428 K. Though we are interested in exercising both codes over a wide range of surface temperatures, it is much easier to change the input heat flux to the ablator

by changing the freestream velocity rather than the temperature. This is because increasing velocity increases the amount of kinetic energy dissipated in the shock, thus increasing the recovery enthalpy. As such, velocities will range from 1000 to 6000 m/s, in steps of 100 m/s. Finally, the effective body radius of curvature is the same as that used by Chen and Milos, at 0.01905 m.

Table 4.3: Parameters used to generate the curves shown in Figure 4.3 through Figure 4.5.

Parameter	Value
Atomic nitrogen mass fraction, $Y_{N,\infty}$	0.14
Atomic oxygen mass fraction, $Y_{O,\infty}$	0.26
Molec. oxygen mass fraction, $Y_{O_2,\infty}$	0
Molec. nitrogen mass fraction, $Y_{N_2,\infty}$	0.60
Freestream temperature, $T_\infty$	1428 K
Freestream pressure, $P_\infty$	1671 Pa
Freestream velocity, $u_\infty$	1000 to 6000 m/s, in steps of 100 m/s
Body radius of curvature, $R_b$	0.01905

Chaleur uses the same material properties as the ablation code, and its thickness is set to two inches to avoid any issue with the temperature wave reaching the back face of the ablator, which would violate the semi-infinite assumption of the ablation code. The ablator was broken into 500 elements, and used an implicit time integrator with a maximum time step of 0.1 seconds. The initial temperature is 536 R. In general with these inputs, Chaleur was found to reach steady state in a time period on the order of 10 seconds. A typical surface recession rate curve from the calculations is shown below as Figure 4.2.

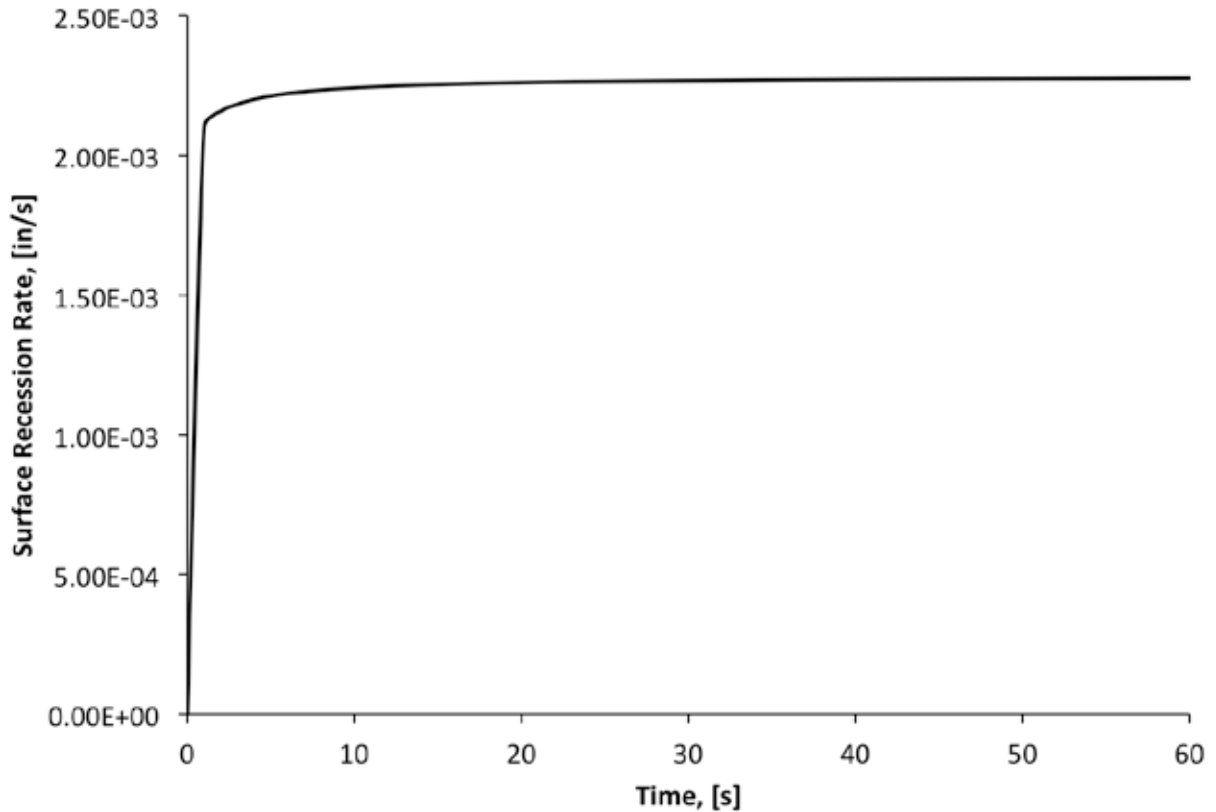


Figure 4.2: Plot of surface recession rate versus time for Chaleur with a graphite ablator.

Before going into the results, it will probably be most helpful to define what is meant by “diffusion-controlled” and “sublimation-controlled”, which are terms that will be used during the course of the following analysis. Throughout the  $B'$  curve, there are three competing processes: surface kinetics, diffusion to and from the surface, and sublimation. Sublimation is a kinetic process, and as such is dependent on the temperature---but it differs from the other reaction processes because the only chemical dependency is on the availability of carbon at the surface, which we assume is essentially infinite.

This is best explained by looking at the Damkohler number, which is a dimensionless number used to relate the reaction and transport timescales:

$$Da = \frac{\tau_{transp}}{\tau_{reac}} \quad 4.13$$

From Equation 2.11, which is the surface mass conservation, we know that

$$J_i + \rho_g v_w Y_{i,w} = \tilde{N}_i$$

for a non-decomposing ablator. Noting that the diffusive mass flux is a product of the mass transfer coefficient and a difference in the mass fractions, and that the reaction rate generally follows an Arrhenius curve, we can say

$$h_m \Delta Y_i + \rho_g v_w Y_{i,w} = \rho Y_{i,w} v_{molec} A_i \exp\left(-\frac{E_{a,i}}{T}\right) \quad 4.14$$

where  $v_{molec}$  is just representing the molecular velocity term (the square root) from Equation 2.16. If we divide through by the heat/mass transfer coefficient, we can say

$$\Delta Y_i + \frac{\rho_g v_w Y_{i,w}}{h_m} = \frac{\rho Y_{i,w} v_{molec} A_i \exp\left(-\frac{E_{a,i}}{T}\right)}{h_m} \quad 4.15$$

and the term on the right is the Damkohler number. As the mass transfer coefficient begins to get very large and the Damkohler number approaches zero, the composition at the wall should begin to approach the composition of the flow. As the mass transfer coefficient gets smaller and the Damkohler number increases,  $\Delta Y$  is less able to drive the reactions and the problem becomes limited by the availability of reactants.

At low surface temperatures, the kinetic reaction rate is relatively slow. Because of the abundance of the reactants required in the surface reaction (in our case, the carbon at the surface and oxygen or nitrogen from the flow), the rate of mass loss is controlled mostly by the surface temperature.  $B'$  will increase along with the surface temperature up until a point, where it should stabilize. When  $B'$  stabilizes, we say we are in the “diffusion-controlled” regime. At surface temperatures higher than this point, the rate of mass loss is controlled more by the ability of the flow to diffuse more reactants to the surface than the surface temperature. Essentially, the reactions at the surface are happening very quickly relative to the rate of transport of species from the freestream, and reactants are being consumed as soon as they reach the surface. As such, the mass loss rate (and thus  $B'$ ) does not increase due to increased surface temperature, and

we expect the value of  $B'$  to follow a roughly straight line. The curve stays constant until sublimation begins, when  $B'$  begins to increase very quickly, again because sublimation is only dependent on the temperature and the availability of carbon at the surface.

Figure 4.3 shows results for the value of  $B'$  with respect to surface temperature. Both curves should look roughly the same---however, they clearly do not. Chaleur looks mostly as we would expect: a straight, though slightly increasing, line in the diffusion-controlled region followed by a sharp increase as the temperature reaches the sublimation-controlled regime. The ablation code, however, follows a curved line, slowly sloping up as it begins to reach the sublimation region. Because of the phenomena outlined above, we also would expect the two curves to converge on a single curve in the sublimation region; clearly this is not the case, and the two sets of calculations are diverging.

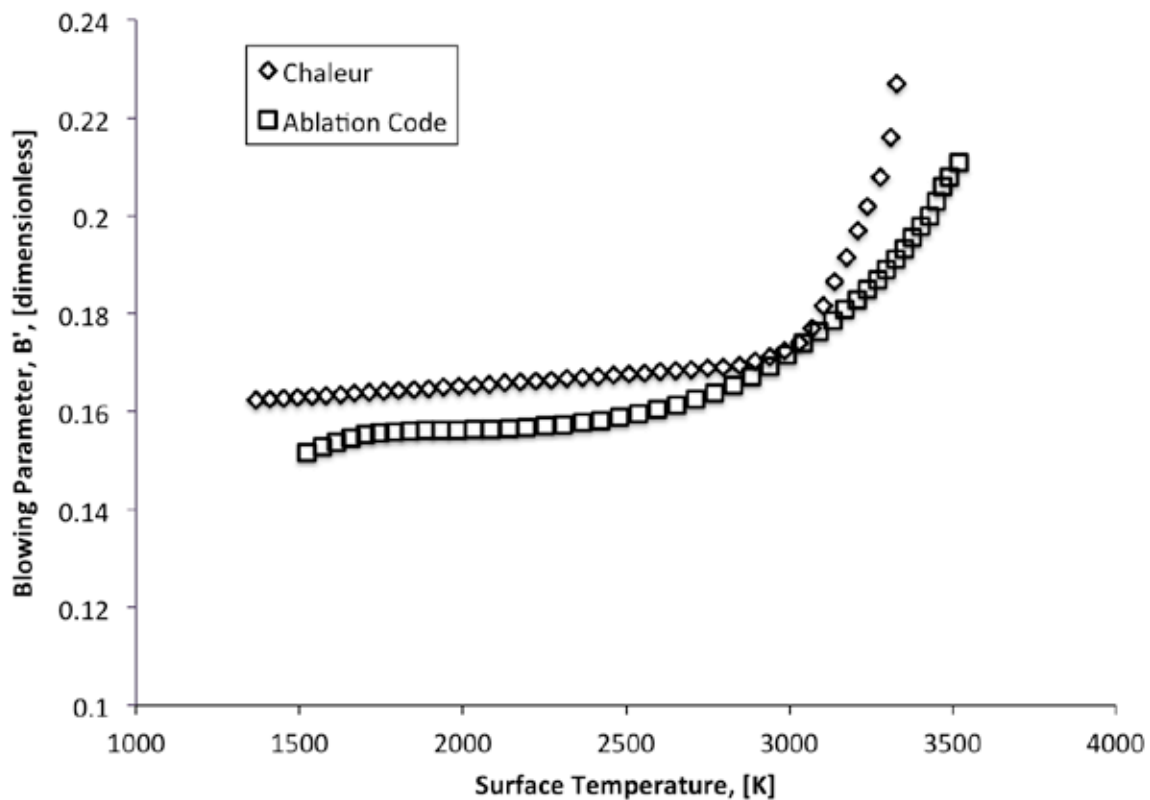


Figure 4.3:  $B'$  versus surface temperature for the ablation code and Chaleur with a graphite ablator.

All of the above are definitely issues, but it may help if we try to look at the same data in a different way. The plot of the actual ablation rates, given in Figure 4.4, can help to give us some more insight. The rates follow curves with similar slopes, though they are separated by some distance, until they start to diverge at a surface temperature somewhere between 3000 and 3500 K. This is where the carbon sublimation begins to occur in Chaleur, but the surface seems to be essentially not sublimating in the ablation code until somewhere above 3500 K.

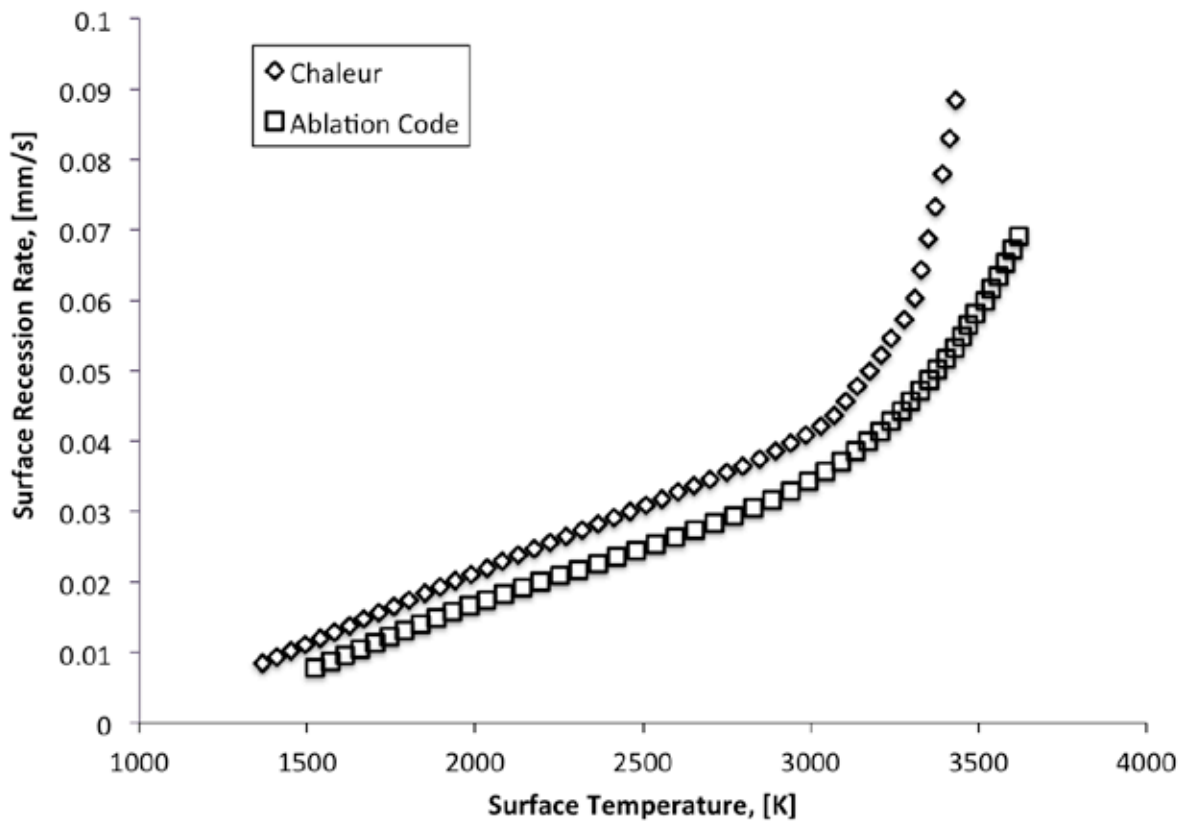


Figure 4.4: Ablation rates versus surface temperature for the ablation code and Chaleur using a graphite ablator.

This sublimation issue is relatively simple to diagnose. These results were computed using the ablation code’s “use\_experimental\_c3\_eq\_conc” option. The default without this option checked is to use equilibrium  $C_3$  surface concentrations as correlated to ACE. In either case, the mass loss rate of  $C_3$  is calculated as in Equation 2.17. However, if

“use\_experimental\_c3\_eq\_conc” is set to one, the equilibrium concentration of tricarbon is computed as

$$x_{C_3,eq} = \frac{A_{C_3,eq,exp} \exp\left(-\frac{E_{a,C_3,eq,exp}}{T}\right)}{\rho_g T} W_{C_3} \quad 4.16$$

and the reaction probability  $\beta_{C_3}$  is also fitted with an Arrhenius-type function:

$$\beta_{C_3} = A_{C_3} \exp\left(-\frac{E_{a,C_3}}{T}\right) \quad 4.17$$

Whereas when “use\_experimental\_c3\_eq\_conc” is set to zero, the equilibrium  $C_3$  composition is computed as

$$x_{C_3,eq} = \frac{A_{C_3,eq} \exp\left(-\frac{E_{a,C_3,eq}}{T}\right)}{P_s} \quad 4.18$$

and the reaction probability  $\beta_{C_3}$  is set to one.

The coefficients used when not using the experimentally correlated  $C_3$  equilibrium concentration values are correlated to ACE. Since ACE is where Chaleur gets its values of  $B'$  from, it makes sense to see how the two compare when using data from the same source. The above calculations were repeated using the other option for tricarbon reactions, and a plot of the results is shown as Figure 4.5.

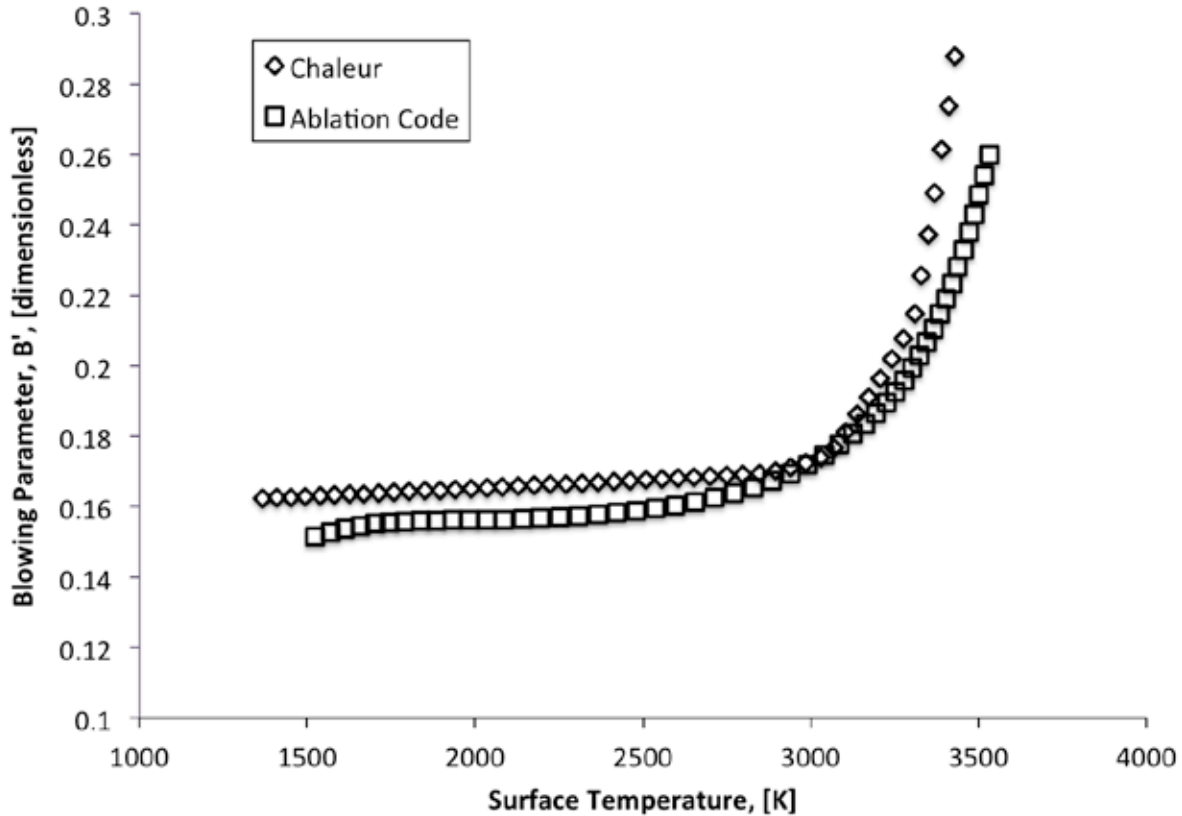


Figure 4.5:  $B'$  versus surface temperature for the ablation code and Chaleur using a graphite ablator. These results were computed using  $x_{C3,eq}$  values fitted from ACE.

In the sublimation-controlled regime, the ablation code and Chaleur match much better (though not exactly) using the ACE-fitted tricarbon equilibrium concentrations than the experimentally-fitted ones. This is to be expected because Chaleur is based on data from ACE; it does not mean that the experimentally-derived values are incorrect, but for the purposes of comparing Chaleur and the ablation code they may not be appropriate. In what should be the diffusion-controlled regime, however, the same problem of the curving ablation code curve persists. In fact, it is likely the *exact* same underlying issue: at lower temperatures, the difference is exactly the same for the different sublimation models. As it is only in the high surface temperature regime that sublimation takes effect, this makes perfect sense. The problem is that the actual underlying issue is somewhat more difficult to deduce.

### 4.4.3: Analysis of the Ablation Code $B'$ Curve

The ablation code  $B'$  curve makes sense in comparison to Chaleur in the sublimation-controlled regime, but not in the diffusion-controlled regime. The dip in the value of  $B'$  at the lower end of the temperature range should be explained, as should the gentle slope into the sublimation region, which we expect to be a steep elbows.

The dip is relatively easy to explain: these curves are representing extinction curves, as are well known in combustion and fire research. Extinction and ignition curves generally follow an “s” shape, as shown in Figure 4.6. In an extinction process, one follows the curve from higher temperatures to lower temperatures; the middle part of the s-shape is bypassed, and the temperature suddenly jumps to a lower level. Similarly, in ignition, as one moves from lower to higher temperatures, the middle of the s-shape is bypassed and the temperature suddenly increases.

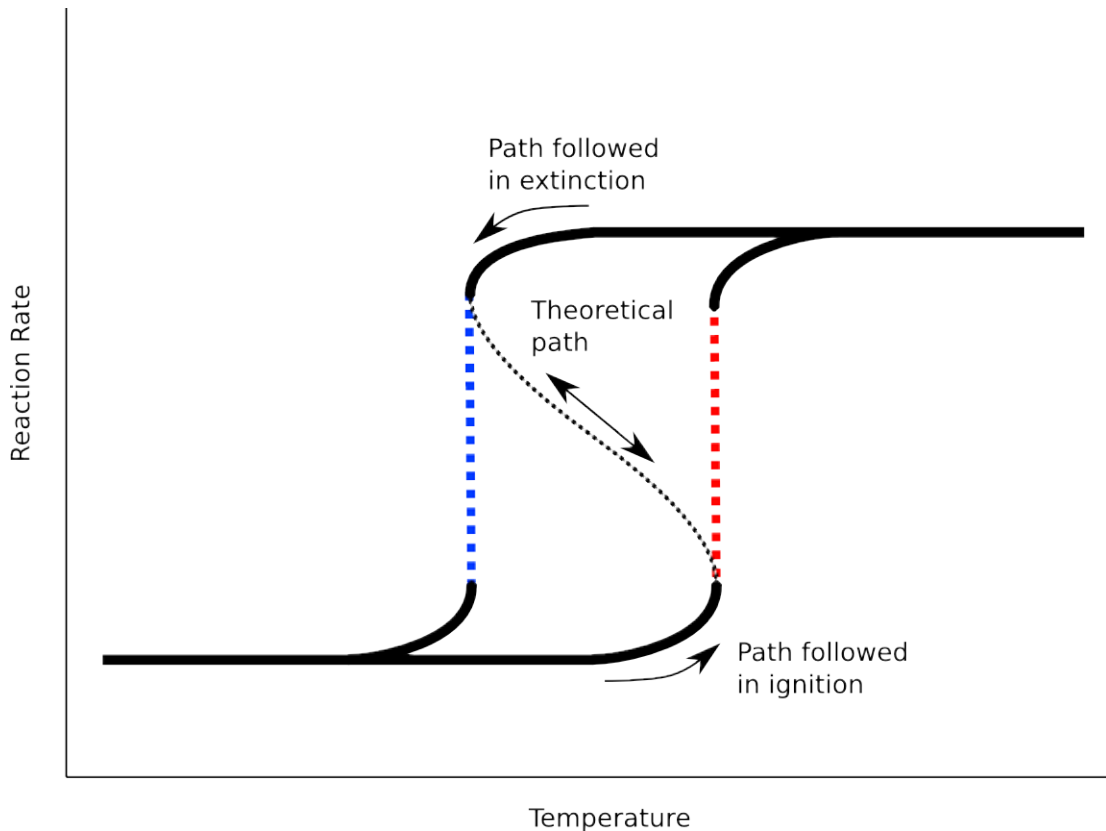


Figure 4.6: A typical ignition and extinction process.

The fact that the  $B'$  values are following extinction curves is easily explained by the circumstances of the problem: as the air passes through the shock, most of the oxygen is dissociated. Atomic oxygen, in our formulation, has a highly temperature dependent reaction rate. It should start to see ignition at lower surface temperature---depending, of course, on the value of the Damkohler number, as discussed previously. We do not see this phenomenon in Chaleur precisely because of the model differences between the two codes. Chaleur uses an equilibrium model at the surface, and regardless of how fast the diffusion of species is taking place, equilibrium is faster; equilibrium is always as fast as it needs to be. Chaleur will therefore always trace the same  $B'$  curve given an input surface temperature and pressure regardless of the value of the film transfer coefficient that is input. That coefficient is only used to drive the heat transfer to the surface, and has nothing to do with the surface chemistry other than its impact on the surface energy balance.

The other question, which is perhaps more important, is the curvature of the ablation code's  $B'$  curve throughout the diffusion-controlled region. The underlying issue, however, is fairly evident when considering how the calculations are being performed. When executing these calculations, we are first taking some input variables and evolving them across a shock before the resulting boundary layer edge variables are used as inputs to the ablation code. There is no knowledge in advance of what the value of the heat transfer coefficient would look like, and the relationship between this heat transfer coefficient and the freestream flow parameters is *very* complex.

Essentially, we are not calculating the  $B'$  curves we expect to see because the  $B'$  curves we expect are not good representations of how the system will act under actual physical circumstances. They are a good way to show how the surface responds to an input stimulus, such as an imposed temperature and pressure, but they effectively assume a constant value of the heat transfer coefficient. By varying the freestream velocity between cases, our heat transfer coefficient is very much not constant.

To ensure that it is in fact the dependence of the heat transfer coefficient on the velocity that is responsible for the issues in the  $B'$  curve, a number of computations were performed. The results are shown below as Figure 4.7. In these computations, a new model for heat transfer was used that is exactly the same as that the one in Chaleur: an enthalpy-driven heat transfer with a constant input heat transfer coefficient and recovery enthalpy:

$$q''_{conv} = h_m(i_r - i_\infty) \quad 4.19$$

where  $h_m$  and  $i_r$  are constant inputs. By using this model we can directly control the input heat transfer through both the heat transfer coefficient and the enthalpy, allowing us to see how having an increasing heat transfer coefficient may affect the value of  $B'$  in the diffusion-controlled regime. (As a side note, modeling the recovery enthalpy as we did before, in terms of the boundary layer edge temperature, composition, and velocity, gives us the same level of control over the problem. When  $h_m$  is held constant, there are no other parameters in the code that depend on that temperature or velocity.)

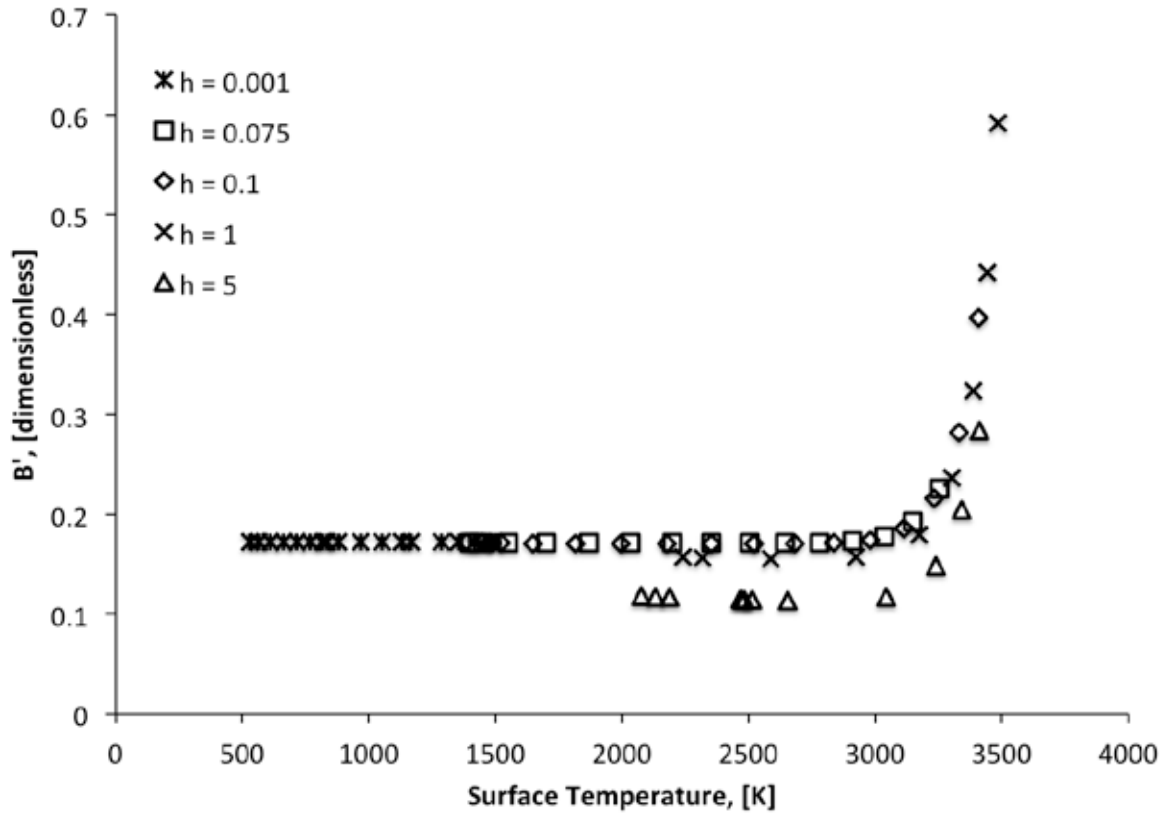


Figure 4.7:  $B'$  versus surface temperature for a number of values of  $h_m$  over a range of input recovery enthalpies.

All of the  $B'$  curves, even the ones at higher  $h_m$  values, are straight rather than slanted or curved. This is because the value of  $h_m$  is held constant across each curve; if it were to be a function of the velocity or temperature we would get similar results to before. As we expect, at lower values of  $h_m$ —all of the values of  $h_m$  below 1 in the figure—the values of  $B'$  in the diffusion-controlled regime all collapse onto a single curve. As  $h_m$  increases to extremely high levels, the value of  $B'$  in the diffusion-controlled regime begins to drop significantly, corresponding to a large Damkohler number. The curves then converge on a single curve as they approach the sublimation-controlled regime, again as expected.

### ***New Chaleur Comparison Method***

Though the unusual trends expressed by the ablation code are not unphysical, when using the full heat transfer correlation as developed previously, they are not useful for comparison with

Chaleur, which is incapable of replicating these phenomena. If we are interested in examining the underlying material response model, we should evaluate Chaleur and the ablation code together in a way that allows for a much better comparison. As such, the method used previously will be modified to use the heat transfer model given above: with input constant heat transfer coefficient and recovery enthalpy. Since this is the same model used by Chaleur, and has been shown to be able to calculate a reasonable  $B'$  curve, it will be used for future comparisons.

#### **4.4.4: Final Chaleur Comparisons**

New comparisons between Chaleur and the ablation code are made using new method. As before, the codes will be compared for both graphite and PICA ablators in such a way as to examine a wide range of surface temperatures. The pressure for each case will be kept constant throughout the computations because pressure helps to shift the  $B'$  curves along the surface temperature axis, which would make comparison much more difficult.

##### ***Graphite Ablator Comparison***

The two codes were compared for the case of a graphite ablator in air over a range of recovery enthalpies and a constant input  $h_m$ , with the results shown as Figure 4.8 and inputs shown in Table 4.4. Park [38], Fletcher [36], and Sakai [40] give typical enthalpy values for the NASA IHF arcjet of 10-50 MJ/kg; Anderson [25] gives a reference for heat transfer coefficients in the range of 0.1 to 1. The value of  $h_m$  chosen was 0.01, to completely avoid the Damkohler number problem discussed previously, and the values of  $i_r$  ranged from 10 MJ/kg to 800 MJ/kg, in order to evaluate the ablator for the range of surface temperatures we would like to see. It is important to note that this is not necessarily physical, but lets us examine a wide range of surface temperatures without having to worry about the  $B'$  issue with respect to the heat transfer coefficient. Surface pressure was set at one atmosphere. Again, as in the results discussed previously, the ablator in Chaleur was set to be thick to avoid violations of the assumptions made in the ablation code—here it is taken to be 3 inches thick and is discretized into 600 elements. The time integration is the same as before, and the initial temperature of the ablator is 536 R.

With these inputs, Chaleur was found to reach steady-state on an order of magnitude of 100-200 seconds, as it did in the previous calculations.

Table 4.4: Parameters used to generate the curves shown in Figure 4.8

Parameter	Value
Molec. oxygen mass fraction, $Y_{O_2,e}$	0.23
Molec. nitrogen mass fraction, $Y_{N_2,e}$	0.77
Boundary layer edge enthalpy, $i_e$	10-100 MJ/kg in steps of 10 MJ/kg; 100-800 MJ/kg in steps of 100 MJ/kg
Surface pressure, $P_s$	1 atm
Heat transfer coefficient, $h_m$	0.01

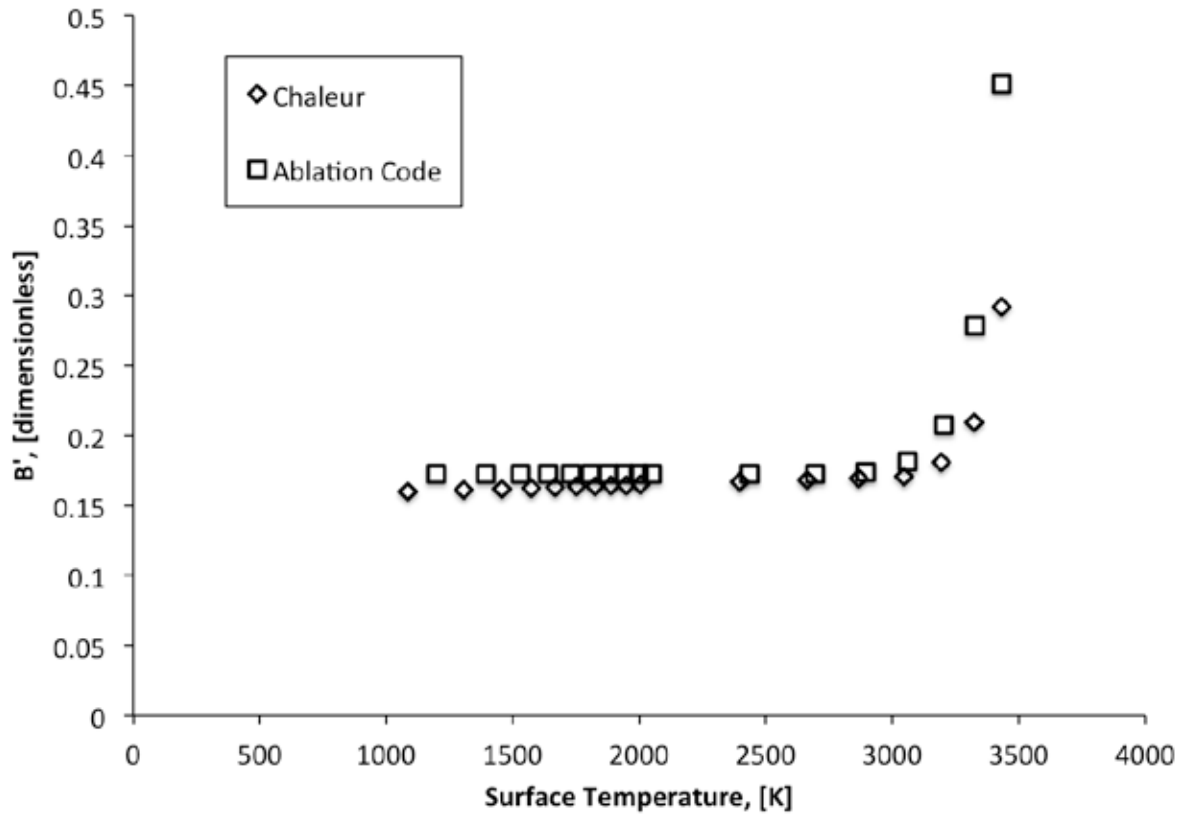


Figure 4.8:  $B'$  versus surface temperature for Chaleur and the ablation code, over a range of input enthalpies and with  $h_m = 0.01$

The ablation code, overall, does a very good job of matching with the results from Chaleur. It has a tendency to solve for a slightly higher surface temperature: at the lower end of the range shown, this difference is as much as 10%, but decreases to virtually no difference as we move along the  $B'$  curve. Also at the lower end of the surface temperature which we explored, the ablation code slightly over-predicts the ablation rate, though the difference in  $B'$  is less than 10% and at higher ranges is around 5%. The only significant issue is in the sublimation regime, where the ablation code seems to be over-predicting the ablation rate by a significant margin---at the highest surface temperature shown on the plot, the difference between the value given by the ablation code and that given by Chaleur is greater than 50%. The steep slope of the curve makes over-prediction easy. That said, it is relatively simple to change the shape of the

sublimation curve by adjusting the kinetic parameters, which can easily be done to match the results from Chaleur.

### *PICA Comparison*

The scenario used for PICA was essentially the same as what was done for graphite with two differences. First, the value of  $h_m$  used was 0.1 rather than 0.01---this was an arbitrary decision, which was made because there did not seem to be any problem with the computed  $B'$  for graphite. Second, the recovery enthalpy was calculated from input freestream temperature, composition, and velocity, rather than being input directly. This was an arbitrary decision as well, and was made to get a better intuitive understanding of what is physically happening in the simulation. It should be noted, however, that using input temperature and velocity to calculate the recovery enthalpy is essentially exactly the same as directly inputting the recovery enthalpy because no other parameters depend on those input variables. As such it is purely an aesthetic decision that should have the same end result. In this case, the temperature was held constant and the velocity was increased, going from 1000 m/s to 10,000 m/s; the specific inputs are given in Table 4.5.

Table 4.5: Parameters used to generate the curves shown in Figure 4.10.

Parameter	Value
Molec. oxygen mass fraction, $Y_{O_2,e}$	0.23
Molec. nitrogen mass fraction, $Y_{N_2,e}$	0.77
Boundary layer edge temperature, $T_e$	1500 K
Boundary layer edge velocity, $u_e$	1000 - 10,000 m/s in steps of 1000 m/s
Surface pressure, $P_s$	1 atm
Heat transfer coefficient, $h_m$	0.1

Again, the thickness of the ablator in Chaleur is 3 inches, discretized into 600 elements, though this time the integrator has a maximum time step of 0.01 seconds. The initial temperature is still set at 536 R. The decomposition data for PICA is taken from [41], since Chaleur uses the same decomposition equations as CMA. With this input data, Chaleur was found to reach steady-state in 10-50 seconds depending on the freestream conditions. A typical recession rate curve for Chaleur with PICA is shown below as Figure 4.9.

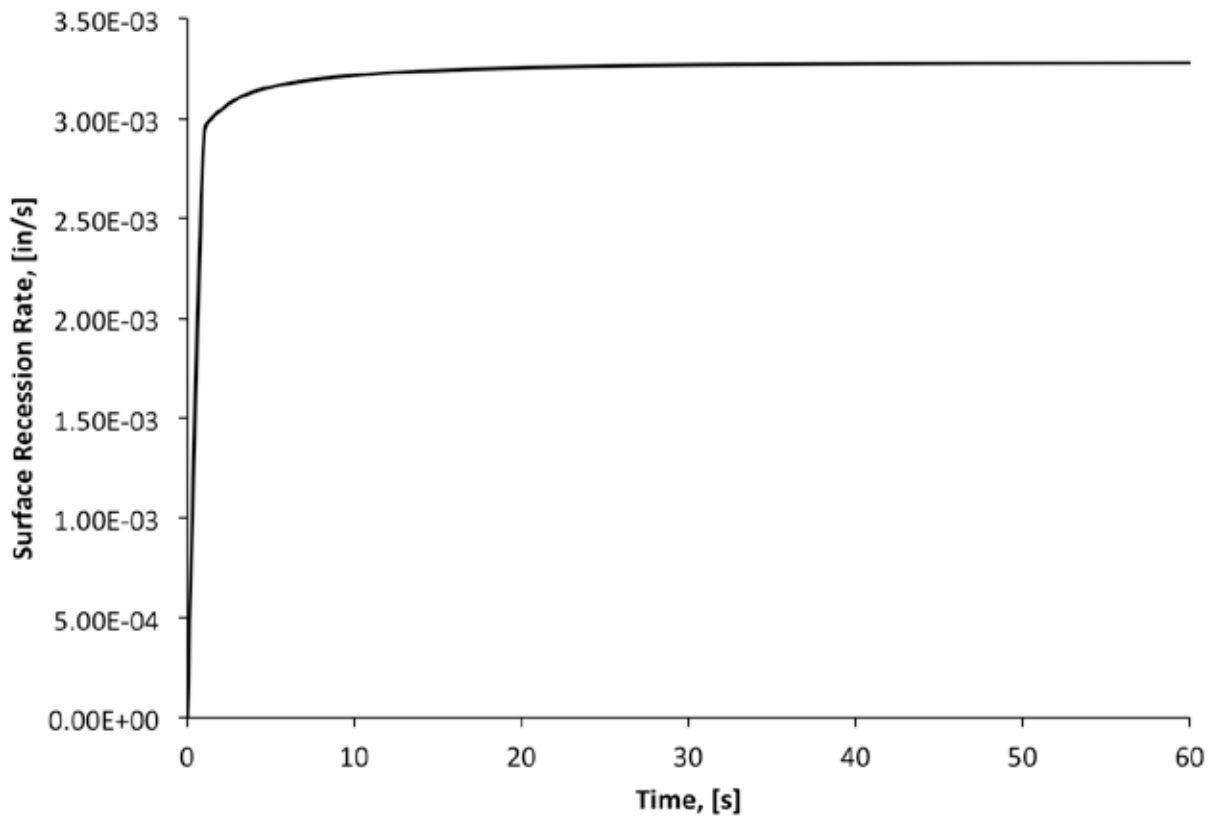


Figure 4.9: Plot of surface recession rate versus time for Chaleur running with a PICA ablator.

The results of the computations are shown below in Figure 4.10. It is worth noting that the  $B'$  used here is not the total  $B'$  for the entire mass loss, which would be the sum of the char blowing parameter and the pyrolysis blowing parameter. It is the  $B'$  specifically for the char,  $B'_C$ . At the lower end of the  $B'$  range which was computed, the surface temperature calculated by the

two codes is different by as much as 10%. The values of  $B'$ , though, are similar, with overall differences of less than 1%. Moving up the  $B'$  curve brings the temperatures closer into alignment but the  $B'$  values farther apart, with the maximum difference of about 10% occurring in the middle of the elbow.

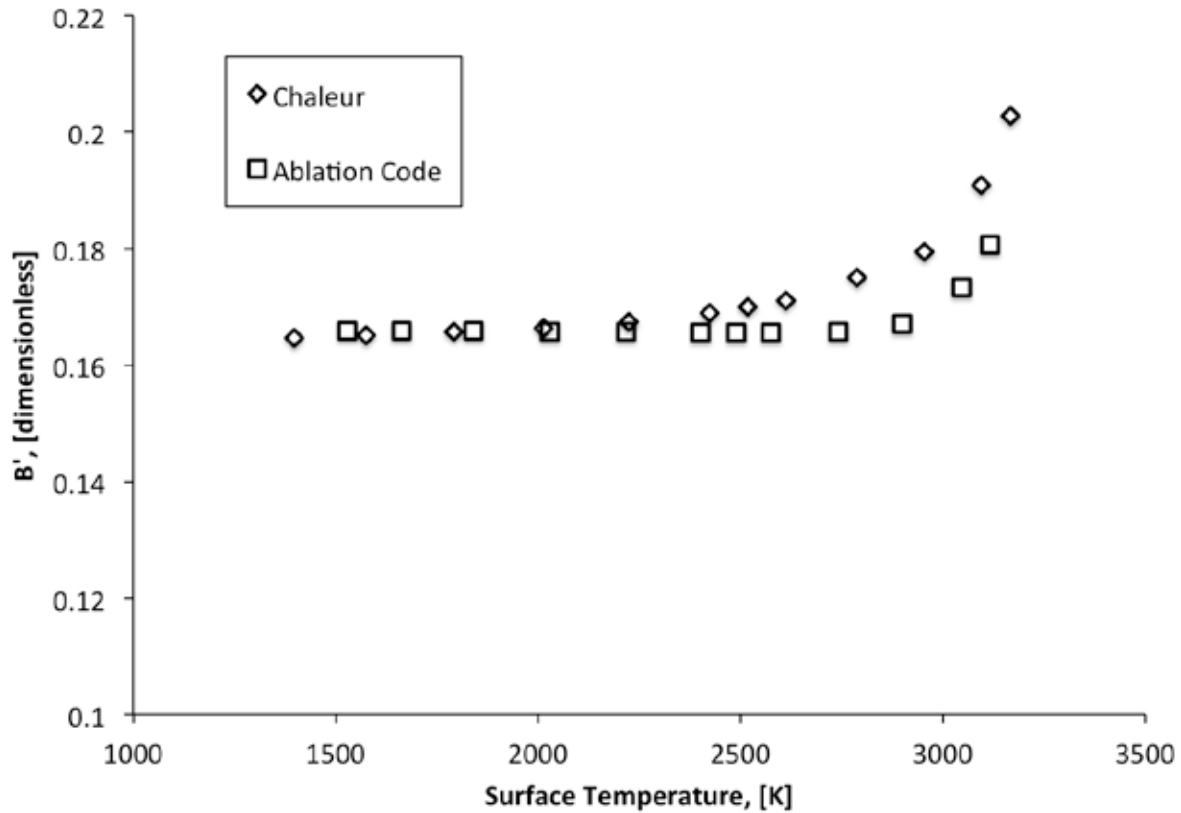


Figure 4.10:  $B'_c$  versus surface temperature for PICA in air, with  $h_m = 0.1$  and the freestream velocity, which effectively sets the recovery enthalpy, varied from 1000 to 10000 m/s.

The  $B'_c$  curve as computed by the ablation code, which as noted at the beginning of this chapter is related to the mass loss rate of the char, looks very similar to the curve computed previously for graphite. This is because, in the ablation code, pyrolysis gases do not have a significant impact on the surface recession rate. This is because for PICA, the difference between the char and virgin densities,  $\rho_c$  and  $\rho_v$ , is relatively small; our source, Tran [41], gives a virgin

density of  $227.45 \text{ kg/m}^3$  and a char density of  $201.06 \text{ kg/m}^3$ . Recall from Equation 2.30 that the pyrolysis gas flux is

$$\dot{m}''_{py} = v_s(\rho_v - \rho_c)$$

whereas the char mass loss rate is

$$\dot{m}''_c = \rho_c v_s$$

Dividing the pyrolysis flux by the char mass loss rate shows that their ratio is

$$\frac{\dot{m}''_{py}}{\dot{m}''_c} = \frac{v_s(\rho_v - \rho_c)}{\rho_c v_s} = \frac{\rho_v}{\rho_c} - 1$$

which for our numbers is approximately 13%. Consider then that the quantity of a given element in the pyrolysis gases is some percentage of that 13% and it is possible to see how the pyrolysis gas composition would have relatively little influence on the value of  $B'_c$ , whereas it seems to have a not insignificant influence for Chaleur. For a larger difference in the char and virgin densities it could potentially have more of an effect in the ablation code, as well.

#### 4.5: CHEN AND MILOS COMPARISON

As noted in Section 4.4.2., our initial Chaleur comparisons were carried out based on the Chen and Milos [8] freestream conditions, which are given in Table 4.3. Knowing what is known now about the ablation code, especially in terms of the sublimation model, it was decided to try to compare directly to the results of Chen and Milos' calculations. Results were computed using the values given in the table and Chen and Milos' freestream velocity of 5354 m/s, and they are given below in Table 4.6.

Table 4.6: Comparison of results from the ablation code to calculations by Chen and Milos.

	Parameter	Chen and Milos	Shock/Ablation Code
Boundary Layer Edge Composition	$Y_{N_2,e}$	0.63	0.61
	$Y_{O,e}$	0.25	0.25
	$Y_{N,e}$	0.12	0.11
	$Y_{O_2,e}$	$1 \times 10^{-4}$	$3 \times 10^{-4}$
Surface Composition	$Y_{CO,w}$	0.30	0.35
	$Y_{CN,w}$	0.02	0.026
	$Y_{C_3,w}$	0.15	0.03
	$Y_{N,w}$	0.03	0.08
	$Y_{O,w}$	0.01	0.008
	$Y_{O_2,w}$	0	0.0003
	$Y_{N_2,w}$	0.43	0.50
Surface Temperature, [K]		3500	3475
Surface Pressure, [kPa]		82	83
Mass Loss Rate, [kg/m <sup>2</sup> -s]		0.14	0.14
Heat Flux, [W/cm <sup>2</sup> ]		800	527

The mass loss rate and heat flux values from Chen and Milos are extracted from the “Park – no nitridation” curves their given charts, and as such may not be extremely precise. That said, the comparison is nonetheless impressive: the shock code does a very good job of calculating the boundary layer edge composition, and the ablation code matches surprisingly well with all of the surface conditions with the exception of the heat flux, which could be a result of a mismatch in some parameters in the comparison. Chen and Milos do not give values for their emissivity or graphite density, and these are very important--as will be discussed in the next section.

## Chapter 5: Uncertainty Propagation with the Direct Quadrature Method of Moments

### 5.1: UNCERTAINTY PROPAGATION

The purpose of performing uncertainty propagation is to determine the sensitivity of the quantity of interest---in this case, the ablation rate---to uncertainty in various parameters in our system simulation. The parameters chosen to be “uncertain” for the purpose of uncertainty propagation will be picked carefully, and their uncertainties will be modeled by probability density functions for distributions which are appropriate for the parameters in question. For the sake of simplicity, scenario parameters will be kept separate from model parameters. This means, for example, that when the activation energy of the carbon monoxide surface reaction is being changed the input flow conditions will be kept constant. The reverse will be true as well: when varying flow conditions, model parameters internal to the material response code will be kept constant.

This type of uncertainty propagation is frequently done using the Monte Carlo method, where a domain of possible inputs is generated according to a probability distribution, points are randomly sampled from the input space, and computations are carried out at those points, eventually resulting in a distribution for the quantity of interest. However, to carry out the simulation enough times to get a large enough sample of the input space to be able to fully approximate the distribution function can be very computationally expensive. This is particularly true if one wishes to study the impact of varying multiple parameters at once rather than independently.

As such, when performing the uncertainty propagation in the ablation code the quadrature method of moments (QMOM) will be used. This will help to minimize the number of computations that are required (though for large numbers of parameters and large numbers of quadrature points, QMOM can still be very computationally expensive) and give us multiple

methods for determining the probability density function of the quantity of interest. Further, a C++ library developed by Rochan Upadhyay, libMoM, is used to help compute our calculations. It has functions to define probability distributions, calculate moments and points and weights, and evaluate cumulative distribution functions (CDFs) from a set of data.

## 5.2: INTRODUCTION TO THE QUADRATURE METHOD OF MOMENTS

The method of moments (MOM) is a technique for evaluating distributions by their moments. A moment is, generally speaking, a measure of the shape of a distribution: the first moment is the mean, the second moment is the variance, the third moment is the skewness, and so on. The zeroth moment of a probability distribution is always one, but the others will vary. The  $k^{\text{th}}$  moment of a probability distribution  $p(x)$  may be written

$${}_xM_k = \int x^k p(x) dx \quad 5.1$$

A distribution can generally be well defined simply by knowledge of its lower-order moments; more moments can yield a better approximation of the distribution, but for many common probability distributions this is not necessary.

Generally, the method of moments is used to solve for the time evolution of a distribution through a set of moment dynamic equations. This requires the moment equations to be formulated in closed form, such that the equations are only functions of the moments. To circumvent this “severe restriction” on the method of moments, McGraw [20] developed the quadrature method of moments (QMOM), where the moment integral is approximated by  $n$ -point Gaussian quadrature. The  $k^{\text{th}}$  moment may then be written

$${}_xM_k = \sum_{i=1}^n \hat{x}_i^k w_i \quad 5.2$$

where  $\hat{x}_i$  is the  $i^{\text{th}}$  quadrature abscissa (or point) and  $w_i$  is the  $i^{\text{th}}$  quadrature weight. This equation is valid for the evaluation of moments 0 through  $2n - 1$ , where  $n$  is the total number of points used in the quadrature process.

The Jacobian Matrix Transformation (JMT) [42] is an extension of QMOM that can be applied to an arbitrary number of dimensions, where instead of tracking the evolution of a set of moments of a distribution, we directly track the evolution of the quadrature weights and points. Using this method, for a large class of problems, the quadrature points for the output quantity of interest can be computed by mapping the quadrature points for the input distributions through the model function.

### **5.3: LIBMOM**

As discussed previously, the libMoM library is used to aid in the application of QMOM to the problem in question. It has functions to help generate moments from known probability distributions, solve for the quadrature abscissas and weights from a given set of moments, solve for moments from sets of quadrature points and weights, and reconstruct CDFs from either sets of moments or sets of points and weights. It takes advantage of the GNU scientific library (GSL) for solvers and other linear algebra classes (matrices, vectors, etc.).

The probability distributions that libMoM is equipped to handle are the beta, generalized beta, univariate lognormal, and univariate Gaussian distributions. For these distributions, libMoM can, given input shaping parameters, evaluate the moments of the distribution up to an appropriate number, depending on the number of quadrature points specified. Since the moments of these distributions are known, their computation is trivial.

## 5.4: APPLICATION OF QMOM

The way QMOM will be used for uncertainty propagation is relatively simple, and is best explained by way of examples. First, we will look at propagation of uncertainty of a single variable, then move on to multiple variables.

### 5.4.1: Univariate Cases

Say we have a variable,  $x$ , and a function  $y = f(x)$ . Say then that  $x$  has a probability density function  $p(x)$  which corresponds to a known distribution. If the distribution is known, then the moments are known; from these moments we can calculate the quadrature points and weights using methods in libMoM. The moments of the distribution on  $x$  may be written in terms of either the integral or the quadrature method

$${}_xM_k = \int x^k p(x) dx = \sum_{i=1}^n \hat{x}_i^k w_i \quad 5.3$$

Say now that parameter  $y$  has a density  $q(y)$ . The density can be written in terms of the density of  $x$  as

$$q(y) dy = p(x) dx \quad 5.4$$

We can write the moments of the  $y$ -distribution as

$${}_yM_k = \int y^k q(y) dy \quad 5.5$$

which enables us to substitute Equation 5.4 to get

$${}_yM_k = \int [f(x)]^k p(x) dx \quad 5.6$$

If the quadrature points of  $p(x)$  are defined as  $\hat{x}_i$  as discussed previously, let us define the quadrature points of  $q(y)$  as

$$\hat{y}_i = f(\hat{x}_i) \quad 5.7$$

which is simply the function evaluated at each of the quadrature points for the  $x$ -distribution. The quadrature weights associated with the  $y$ -distribution quadrature points are the same as the ones for the  $x$ -distribution. As such, we can write the quadrature approximation for the moments of  $q$  as:

$${}_yM_k = \sum_{i=1}^n \hat{y}_i^k w_i = \sum_{i=1}^n [f(\hat{x}_i)]^k w_i \quad 5.8$$

### ***Univariate Example – $y = x^2$***

To show how this process works, let us take a specific example for which we can easily calculate what the moments of the final distribution should be. If the functional relationship between  $y$  and  $x$  is

$$y = x^2 \quad 5.9$$

we can see from Equation 5.1 that the moments of  $y$  are

$${}_yM_k = \int y^k q(y) dy = \int (x^2)^k p(x) dx \quad 5.10$$

We may now note that the moments of  $y$  can be defined in terms of the moments of the  $x$ -distribution as

$${}_yM_k = \int x^{2k} p(x) dx = {}_xM_{2k} \quad 5.11$$

which is saying that the  $k^{\text{th}}$  moment on  $y$  is equal to the  $2k^{\text{th}}$  moment on  $x$ . Performing the process outlined above to calculate the moments on  $y$  by the quadrature points and weights yields exactly what we would expect.

### **5.4.2: Multivariate Cases**

In general, we call cases with more than one variable multivariate, though a case with two variables may be referred to as bivariate. First we will look at a bivariate example, and then move to a more general multivariate case. Say now that we have a function

$$z = f(x, y) \tag{5.12}$$

where  $x$  and  $y$  are independent parameters that have probability densities  $n(x)$  and  $m(y)$ , respectively, and that these yield a density on  $z$  of  $s(z)$ . We will now say that these variables  $x$  and  $y$  have moments that may be represented as

$${}_xM_k = \sum_{i=1}^{N_i} \hat{x}_i^k w_i \tag{5.13}$$

$${}_yM_k = \sum_{j=1}^{N_j} \hat{y}_j^k v_j \tag{5.14}$$

We can say, based on previous analysis, that the moments of  $s$  may be written

$${}_zM_l = \sum_{h=1}^{N_h} \hat{z}_h^l u_h \tag{5.15}$$

where  $h$  is an index that is different from  $i$  or  $j$ ---it is along the internal space of  $z$ . This function may be rewritten as

$${}_zM_l = \sum_{i=1}^{N_i} \sum_{j=1}^{N_j} [f(\hat{x}_i, \hat{y}_j)]^l w_i v_j \tag{5.16}$$

so we can see that  $h$  will range from 1 to  $N_i N_j$ , that the quadrature points in  $z$ -space are all of the possible combinations of the  $x$ - and  $y$ -space quadrature points, and that the weights associated with each quadrature point in  $z$  are the product of the corresponding  $x$  and  $y$  quadrature weights.

This method can easily be generalized to an arbitrary number of dimensions. The function is evaluated at points corresponding to combinations of quadrature points in each of the dimensions. At these points, the weight applied to the resulting quadrature point is the product of the weights of the original points. For an arbitrary number of dimensions, the problem scales up quickly: if there are  $N$  quadrature points in each of the  $M$  dimensions, there will need to be  $N^M$  evaluations of the function. As such, higher-dimensional problems are undesirable but increasing

numbers of quadrature points to better represent the underlying densities are relatively computationally inexpensive.

***Bivariate Example –  $z = xy$***

As in the univariate example, we choose an example that we can evaluate analytically to ensure that the method is acting as it should. For a case where

$$z = xy \tag{5.17}$$

we can say that the final moments of the distribution on  $z$  will look like

$${}_z M_l = \int z^l s(z) dz \tag{5.18}$$

Using the definition

$$s(z) dz = n(x)m(y) dx dy \tag{5.19}$$

we may write

$${}_z M_l = \iint (xy)^l n(x)m(y) dx dy \tag{5.20}$$

This is precisely equivalent to

$${}_z M_l = {}_x M_l {}_y M_l \tag{5.21}$$

When performing the process outlined above in terms of the quadrature points and weights, we obtain the expected result.

**5.5: SAMPLE PROBLEM**

To show the utility of the QMOM method, we first take an example problem that can be evaluated analytically. Say we have a variable,  $z$ , which is a function of two independent variables  $x$  and  $y$  in the form

$$z = ax + by \tag{5.22}$$

such that  $z$  is a linear combination of  $x$  and  $y$ . Say now that  $x$  and  $y$  have probability density functions  $m(x)$  and  $n(y)$ , leading to a probability density function in the solution  $s(z)$ . The first moment, which is the mean, of the pdf  $s(z)$  may be evaluated as

$${}_z M_1 = \bar{z} = \iint zs(z)dz \quad 5.23$$

Which as we noted previously may be transformed to

$$\bar{z} = \iint (ax + by)m(x)n(y)dxdy \quad 5.24$$

We can break Equation 5.32 into separate integrals on  $x$  and  $y$ , because by definition

$$\int m(x)dx = \int n(y)dy = 1$$

The mean then looks like

$$\bar{z} = a \int xm(x)dx + b \int yn(y)dy \quad 5.25$$

The two integrals are the equivalents of the first moments of the densities  $m$  and  $n$  and thus we can say that

$$\bar{z} = a\bar{x} + b\bar{y} \quad 5.26$$

Let us now consider the second central moment, which is the variance. This moment, for the density  $s(z)$ , takes the form

$$\text{var}(z) = \int (z - \bar{z})^2 s(z)dz \quad 5.27$$

Again, substitution gives us

$$\text{var}(z) = \iint [a(x - \bar{x}) + b(y - \bar{y})]^2 m(x)n(y)dxdy \quad 5.28$$

The first term in the integral may be written

$$(z - \bar{z})^2 = a^2(x - \bar{x})^2 + 2ab(x - \bar{x})(y - \bar{y}) + b^2(y - \bar{y})^2 \quad 5.29$$

Knowing this, we may now break the integral into three parts: one that is only a function of  $x$ , one that is only a function of  $y$ , and one that is a function of both. We will call these components  $A$ ,  $B$ , and  $C$ , respectively.

Let us take a look at  $A$ :

$$A = \int a^2(x - \bar{x})^2 m(x) dx$$

Moving the coefficient  $a^2$  outside of the integral lets us recognize that this is simply the second central moment of the density  $m$  and therefore that

$$A = a^2 \int (x - \bar{x})^2 m(x) dx = a^2 \text{var}(x)$$

The same is true of  $C$ :

$$C = b^2 \text{var}(y)$$

$B$ , however, is equal to zero---it is the product of the first central moments of  $x$  and  $y$ , which must both be zero. As such, we can then say that

$$\text{var}(z) = a^2 \text{var}(x) + b^2 \text{var}(y) \quad 5.30$$

which if we take the square root, gives us the standard deviation:

$$\sigma_z = \sqrt{a^2 \sigma_x^2 + b^2 \sigma_y^2} \quad 5.31$$

This looks very similar to the Kline and McClintock method presented by Figliola and Beasley [43] for computing the uncertainty in a result  $R$  based on the sensitivity of  $R$  to the input variables:

$$u_R = \pm \sqrt{\sum_{i=1}^L \left( \frac{\partial R}{\partial x_i} u_{x_i} \right)^2} \quad 5.32$$

where  $u_R$  is the uncertainty in the result,  $x_i$  is the  $i^{\text{th}}$  input parameter (of which there are  $L$ ), and  $u_{x_i}$  is the uncertainty in that input parameter. It is clear that Equation 5.31 is exactly equivalent to Equation 5.32 when the “uncertainty” used is the standard deviation. This analysis also suggests that Equation 5.32 is *only* applicable when the “result” variable is a linear combination of independent parameters.

Regardless, we can compare using QMOM and this uncertainty method for a simple system. Say that we take the variables  $a$  and  $b$  from Equation 5.22 to be 2 and 3, respectively. Say now that  $x$  and  $y$  are normally distributed with means of 4 and 6, respectively, and standard deviations of 0.2 and 0.5, respectively. From the Kline and McClintock method, we can compute that the “error” in  $z$  should be:

$$u_z = \pm\sqrt{(2 * 0.2)^2 + (3 * 0.5)^2} = \pm 1.552$$

and the mean of  $z$  should be 26.

Using QMOM, we can calculate the standard deviation from the moments of  $z$ . With the information given above, our code gives us the first moment equal to 26 and a second moment equal to 678.41, which initially seems very wrong. However, our code does not calculate the central moments; it calculates the moments about the origin. The conversion from a second moment about the origin to a second moment about the mean is

$$M_2 = M'_2 - \mu^2$$

and therefore our variance is  $678.41 - (26)^2 = 2.41$ . The standard deviation, which as mentioned previously is the square root of the variance, is then equal to 1.552 and the two results are identical.

## 5.6: SELECTION OF UNCERTAIN PARAMETERS

As mentioned in the previous section, the curse of dimensionality can rear its head for large numbers of uncertain parameters and it is in our best interest to only examine those which

have a significant impact on the quantity of interest. A parameter that is very uncertain but only changes the quantity of interest by a small percentage is not particularly worth studying. Because of this, it will be necessary to perform a parameter sensitivity study before beginning the uncertainty propagation process.

We will narrow the number of possible options by ruling out some parameters before starting. Scenario parameters that help define the conditions of the simulation, such as the freestream velocity and temperature, will be considered to be constant inputs. Though they will certainly have a significant impact on the solution obtained, it makes the most sense to define uncertainty bounds on these parameters for a specific flight mission, which is beyond the scope of this paper---the author is not a NASA design engineer. For PICA, we will not consider the elemental fractions of the species in the virgin to be uncertain. We will also not consider the thermodynamic property correlation coefficients to be uncertain, because they are specifically calibrated to the model in question and are extremely widely used throughout the literature.

Ignoring the uncertainty of these parameters helps to narrow the list somewhat. We are left with two groups of parameters: the material properties of the ablator and the kinetic parameters used in the surface chemistry calculations. Each of these parameters will be perturbed by  $\pm 10\%$  from their nominal values (as given in Appendix B:) and separately run through the ablation code to determine their individual impact on our quantity of interest, which is the ablation rate. This will help us to choose the most important parameters by showing which have the largest impact.

However, this choice is compounded by the fact that parameters may have more or less of an impact in different scenarios. This is particularly true of the parameters used to calculate the chemical kinetics. For example, take the molecular oxygen reaction probability,  $\beta_{O_2}$ . In a gas composed of only atomic oxygen,  $\beta_{O_2}$  will have no impact; in a gas composed entirely of  $O_2$ , it may have a significant impact. As such, the choice of a scenario is extremely important---it should be a relatively realistic scenario, to give all of the parameters an appropriate level of importance.

## 5.7: UNCERTAINTY PROPAGATION WITH GRAPHITE IN THE CHEN AND MILOS CONDITIONS

We will use the scenario outlined by Chen and Milos [8] in their simulation of a graphite ablator in an arcjet because its freestream conditions are well-specified. The parameters given by Chen and Milos are evolved across a shock using the previously-described shock code to obtain their post-shock values, which are used as inputs to the ablation code. The post-shock boundary layer edge temperature is found to be 5981 K, the boundary layer edge pressure is found to be 79.7 kPa, the boundary layer edge velocity is found to be 467 m/s, and the composition is:  $Y_N = 0.116$ ,  $Y_O = 0.254$ ,  $Y_{N_2} = 0.619$ , and  $Y_{NO} = 0.011$ , with all the others zero. It is worth noting that though the nominal value of the emissivity and absorptivity is 1, that value was changed to 0.9 for the purposes of the uncertainty evaluation since it is unphysical for these values to be above 1. From these inputs, with an input body radius of curvature of 0.01905 m (as given by Chen and Milos), the nominal ablation rate is found to be  $6.54 \times 10^{-5}$  m/s.

### 5.7.1: Preliminary Uncertainty Analysis and Parameter Distributions

The results of the preliminary analysis are given below in Figure 5.1. As can be seen in the figure, the ablation code in this specific simulation is most sensitive to the activation energy of the tricarbon equilibrium concentration correlation, the graphite density, the emissivity, and, though they are difficult to see on the plot, the tricarbon equilibrium concentration pre-exponential and the reaction probability of nitrogen. It is essentially insensitive to the other parameters, though it is important to note that these sensitivities are only valid for this particular scenario and they may be completely different for different freestream conditions.

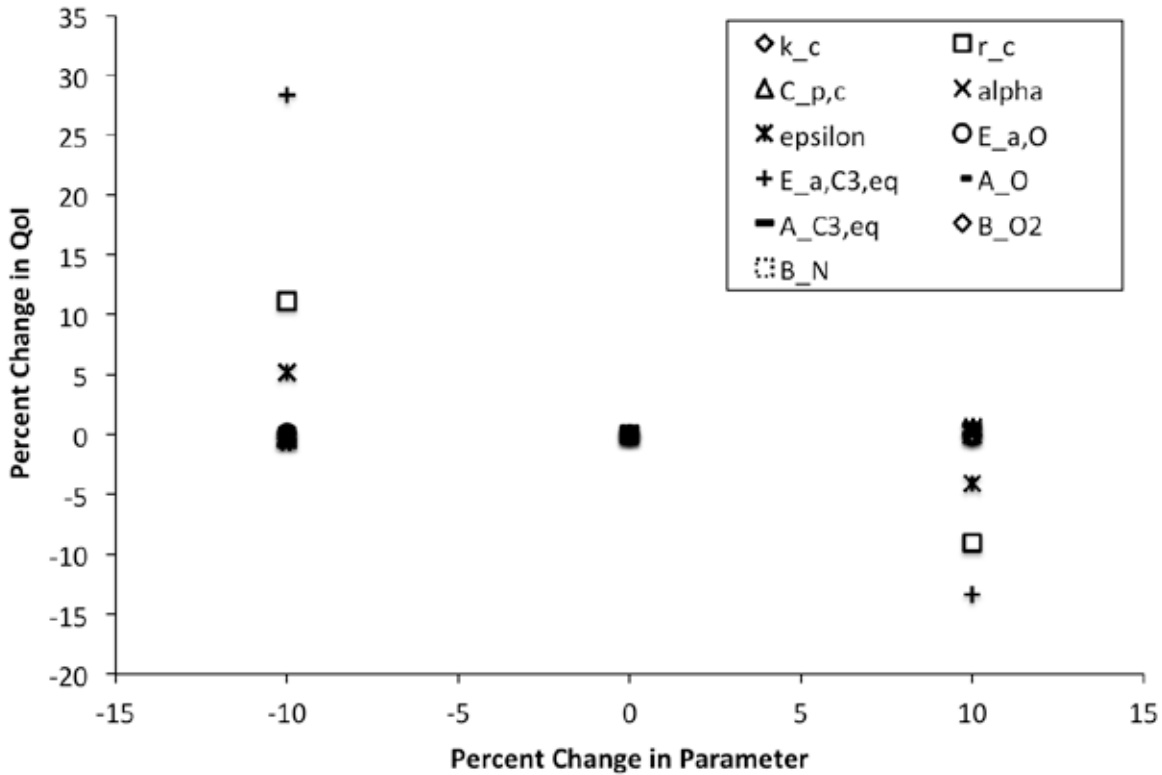


Figure 5.1: Percent change of the ablation rate with respect to the percent change in the input parameters.

The sensitivity of the ablation rate to the tricarbon equilibrium activation energy is highly nonlinear---reducing it by 10% has a significantly larger impact (nearly 30%) than increasing it by 10% (less than 15%). This is because the point we are performing our calculations at is sitting right on the elbow of the  $B'$  curve, where the conditions are such that a slight change can move the surface from diffusion-controlled to sublimation-controlled. This is also how the dependence on the sublimation pre-exponential comes into play. The other parameters make sense as well. The solid density is one of the most important components of the computations. The output radiative heat flux, which depends on the emissivity, is high due to the high temperatures at the surface (nearly 3500 K)---therefore it makes sense that there is some sensitivity to  $\epsilon$ . There is little dependence on the activation energy or pre-exponential for the oxygen reaction because the surface is so hot and thus atomic oxygen reactions are diffusion-limited. The nitridation is

overall not a large contributor to the surface recession rate because the reaction probability is so low. However, the surface recession rate is still sensitive to the reaction probability because the nitridation reactions are slow enough that they are not diffusion-limited. There is no  $O_2$  in the flow and thus the sensitivity to its reaction probability is essentially zero.

Now that we have the parameters that the code is most sensitive to for our given input conditions, we must define the distributions underlying those parameters.

### ***Probability Density of $\rho_c$***

Part of the problem with using a “graphite” ablator is that there are many different kinds of graphite, and all of these different varieties have different material properties. Our nominal value of the density is  $2162.5 \text{ kg/m}^3$ , but Incropera [44] gives the density of amorphous carbon as  $1950 \text{ kg/m}^3$  and of pyrolytic graphite as  $2210 \text{ kg/m}^3$ . Because we are uncertain of exactly what is being used or will be used, it makes the most sense to use a probability density function for the graphite density that has a fairly large variance. We will choose a Gaussian distribution with a mean of our nominal value ( $2162.5 \text{ kg/m}^3$ ) and a standard deviation large enough that most of the data will lie within 15% of the mean---this gives us  $\sigma = 144.167 \text{ kg/m}^3$ . When using a Gaussian it is always a potential concern that one of the quadrature points could be negative, which would be very much non-physical and would likely break the calculations. However, the mean is sufficiently far enough from the origin, and the standard deviation sufficiently small, that this should not be a problem. The pdf used is shown below in Figure 5.2.

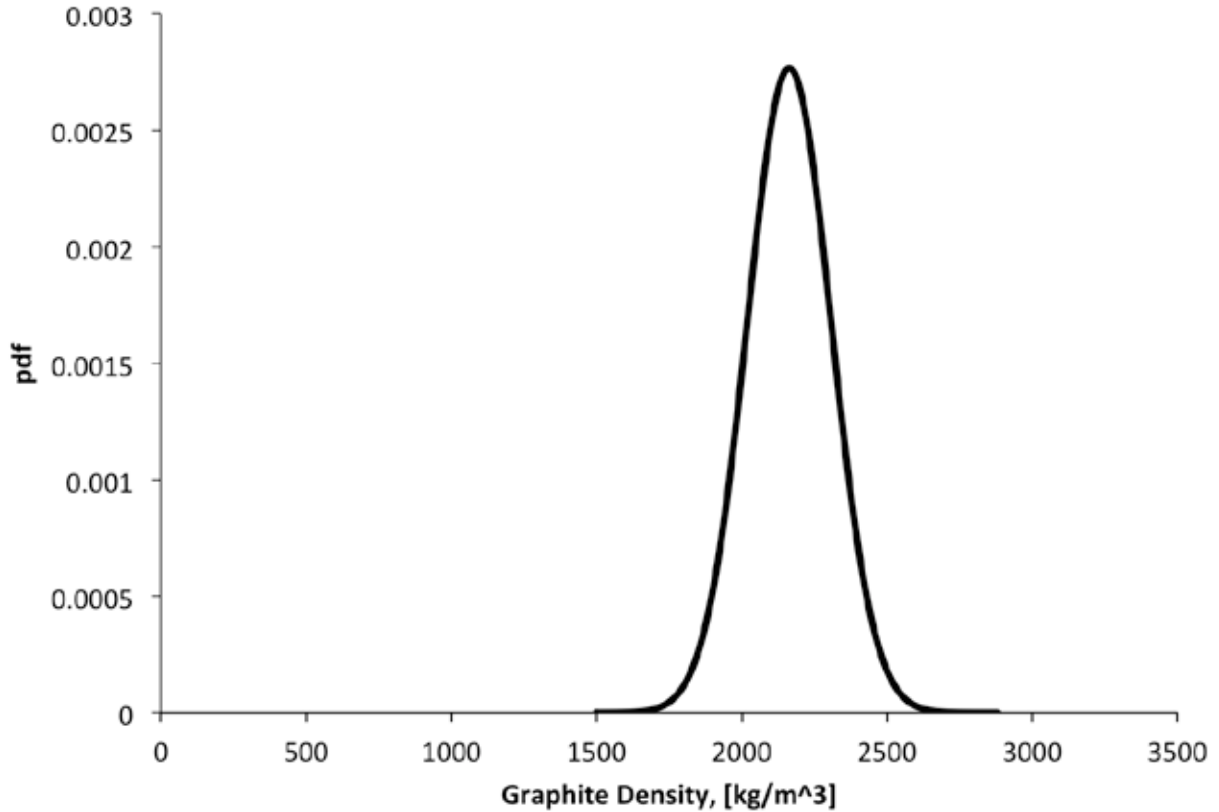


Figure 5.2: Probability density function of the graphite density, which is a Gaussian distribution with a mean of  $2162.5 \text{ kg/m}^3$  and standard deviation of  $144.167 \text{ kg/m}^3$ .

### ***Probability Density of $E_{a,C_3,eq}$***

The nominal value of  $E_{a,C_3,eq}$  comes from a fit of equilibrium concentrations of tricarbon as calculated by ACE. There is obviously no provided information as to what a reasonable value of the uncertainty should be, and any attempt to model the uncertainty would simply be a guess. However, because we must have some sort of distribution, we will choose a distribution wherein most of the curve---3 standard deviations from the mean covers 99.8% of the area under the curve---is inside  $\pm 5\%$  of the nominal value. Since  $E_{a,C_3,eq}$  comes from a curve fit in the first place, there is no expectation that there will be a large variance in its value. The nominal, and thus the mean, value of  $E_{a,C_3,eq}$  is 90908 K. The standard deviation will be  $0.05 \times 90908 / 3 \approx$

1515 (since the distribution is a guess, the precision is unimportant). These yield the distribution shown below as Figure 5.3.

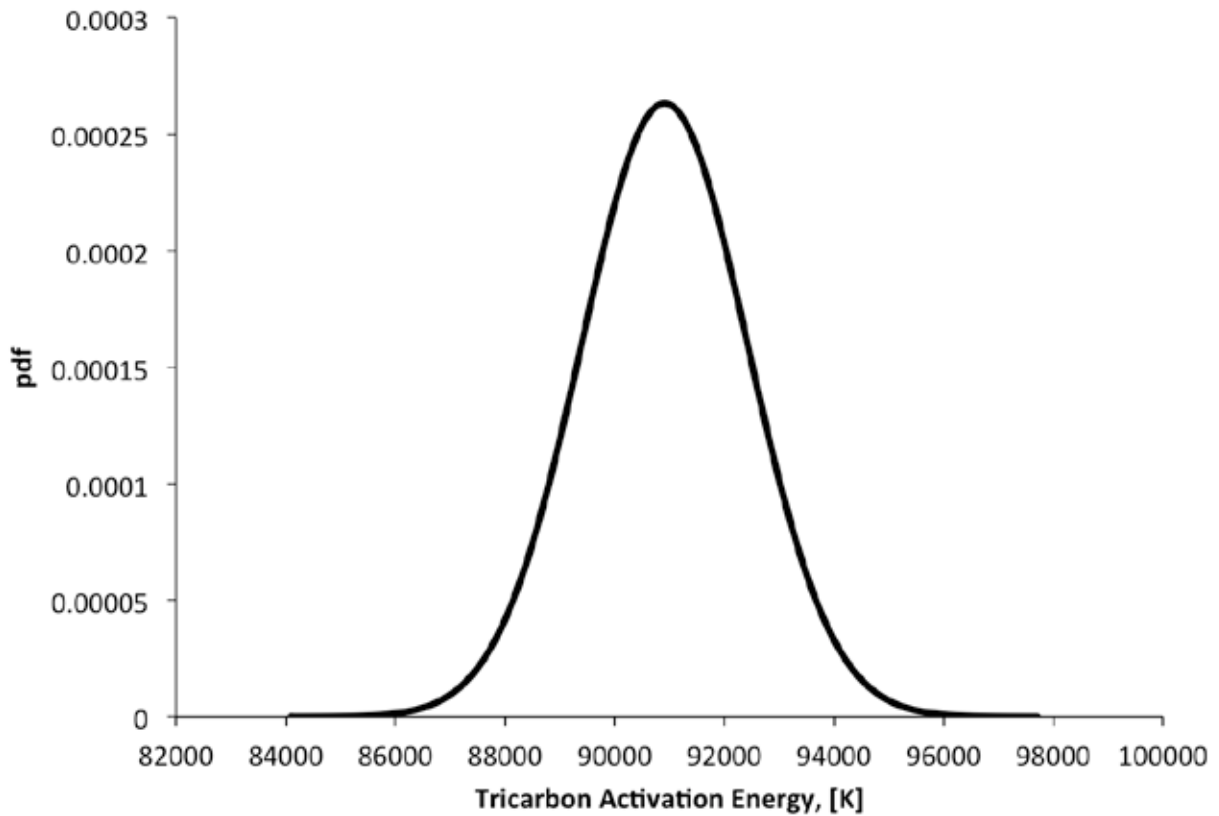


Figure 5.3: Probability density function of the tricarbon equilibrium concentration activation energy, which is a Gaussian distribution with a mean of 90908 K and a standard deviation of 1515 K.

### ***Probability Density of $A_{C_3,eq}$***

To find the probability density function of  $A_{C_3,eq}$ , we will perform the procedure used above to find the  $E_{a,C_3,eq}$  pdf. We take the pdf to be a Gaussian, with a mean of our nominal value,  $6.27 \times 10^{14}$ , and choose a standard deviation such that most of the curve will lie within 5% of the mean. This means that we have  $\sigma = 0.05 \times (6.27 \times 10^{14}) / 3 \approx 1.045 \times 10^{13}$ . Figure 5.4, below, shows our pdf. It should be noted that there are potentially issues associated with

calculating the higher-order moments of this distribution, because the mean is extremely large and the computer may not be able to handle them.

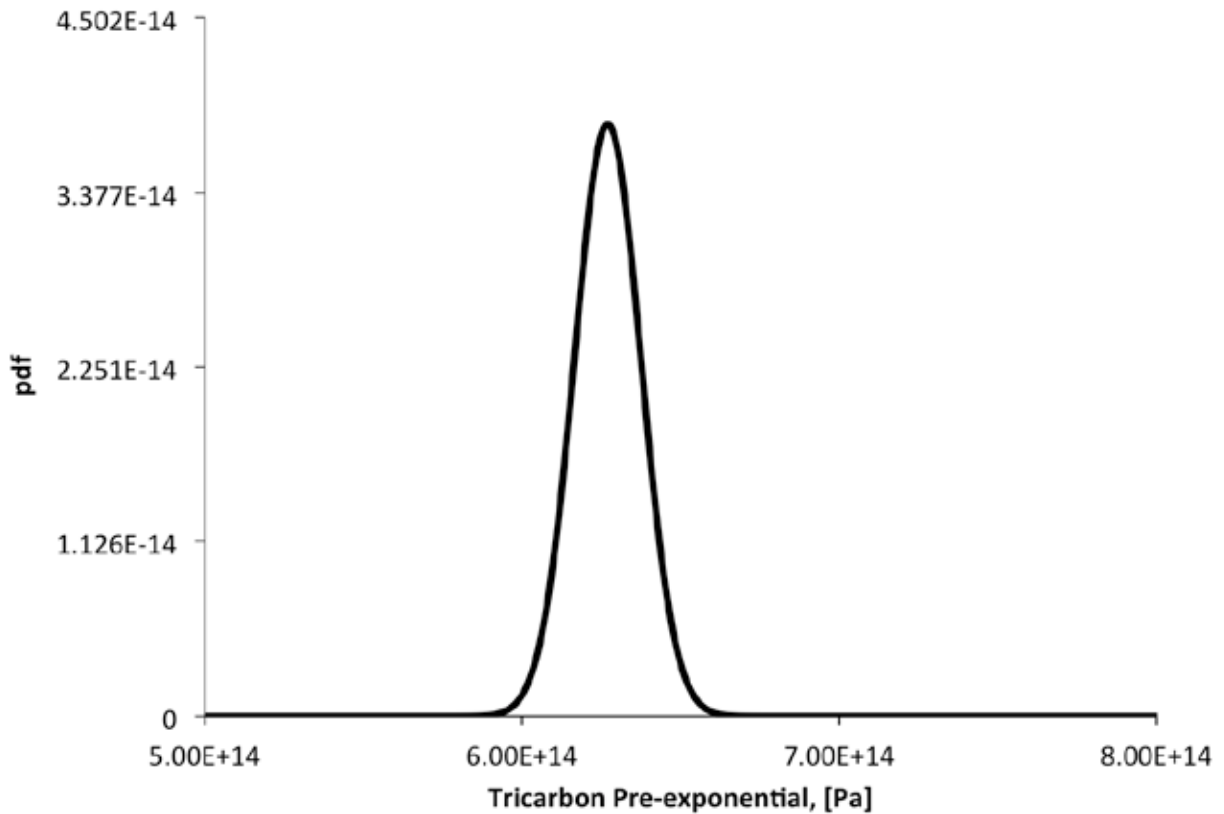


Figure 5.4: Probability density function of the tricarbon equilibrium concentration pre-exponential, which is a Gaussian with a mean of  $6.27 \times 10^{14}$  Pa and standard deviation of  $1.045 \times 10^{13}$  Pa.

### ***Probability Density of $\epsilon$***

The emissivity at the surface should be a relatively high value between zero and one. Knowing this, we will use a beta distribution with  $\alpha = 20$  and  $\beta = 2$ . This results in a distribution with a mean of approximately 0.9 and a standard deviation of approximately 0.06, and the curve shown below in Figure 5.5.

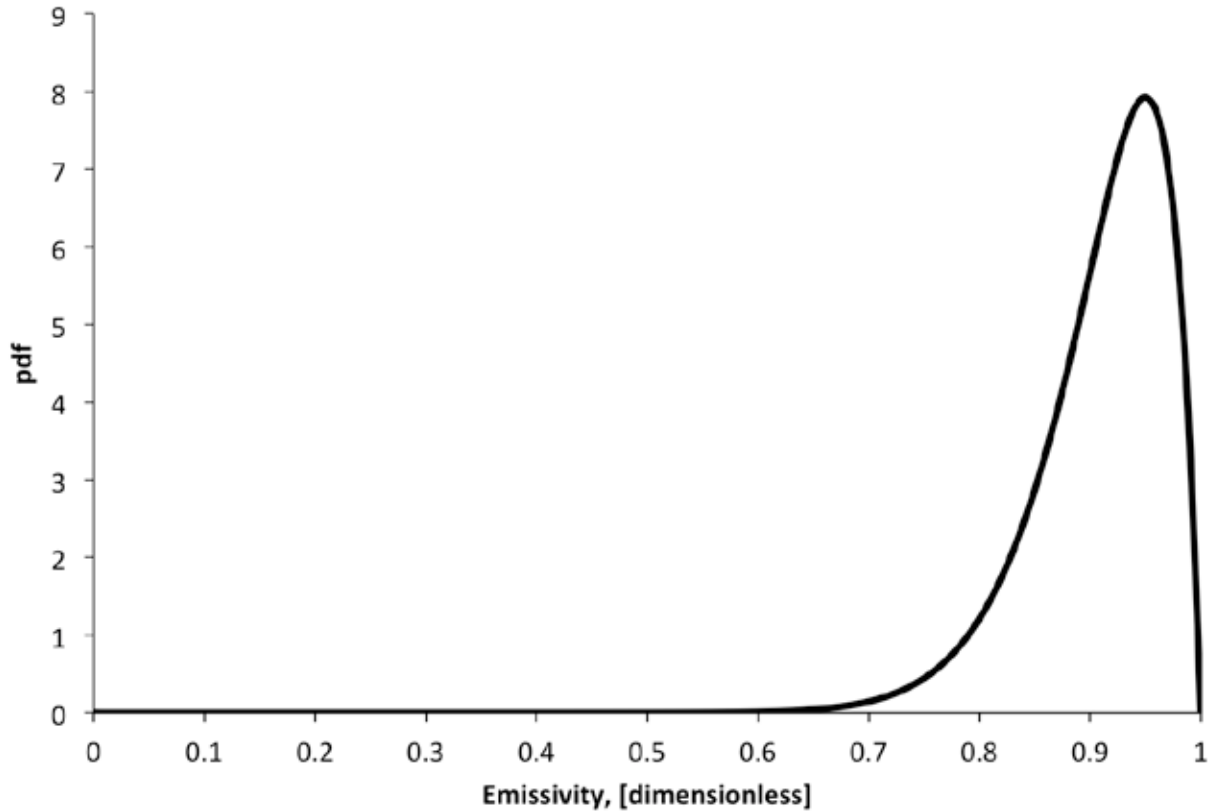


Figure 5.5: Probability density function of the graphite surface emissivity, which is a beta distribution with  $\alpha = 20$  and  $\beta = 2$ .

### ***Probability Density of $\beta_N$***

There has been a great deal of research on nitridation, and different experiments have come up with significantly different values. The one that is used as the nominal value in the current work is one in the range of  $10^{-3} - 10^{-2}$  provided by Marschall [11], but Park [10] has come up with a temperature-independent value of 0.3---two full orders of magnitude above the Marschall value. The Park value was used extensively when beginning the current work, and was found to *significantly* over-predict both the ablation rate and the amount of CN in the flow. In some circumstances, nearly all of the free atomic nitrogen would be converted to CN, and the ablation rate would be multiple times the accepted value.

Marschall provides a number of different values of the reaction efficiency, and these can be used to compute a distribution. It should be noted that Marschall's values are computed at a number of different experimental conditions, especially including velocity and surface temperature. Since the ablation code was originally made with Park's model in mind, it is currently not possible for  $\beta_N$  to be a function of temperature. As such, we will take the different experimental conditions of Marschall's experiments and account for them by using all of his  $\beta_N$  values regardless of the conditions under which they were obtained.

We will use the beta distribution rather than the lognormal distribution so that the pdf will be bounded on the interval  $[0,1]$  rather than extending to infinity. We find that a distribution with  $\alpha = 2$  and  $\beta = 600$  gives us a mean of approximately 0.003, with a standard deviation of 0.001, and results in the pdf shown in Figure 5.6.

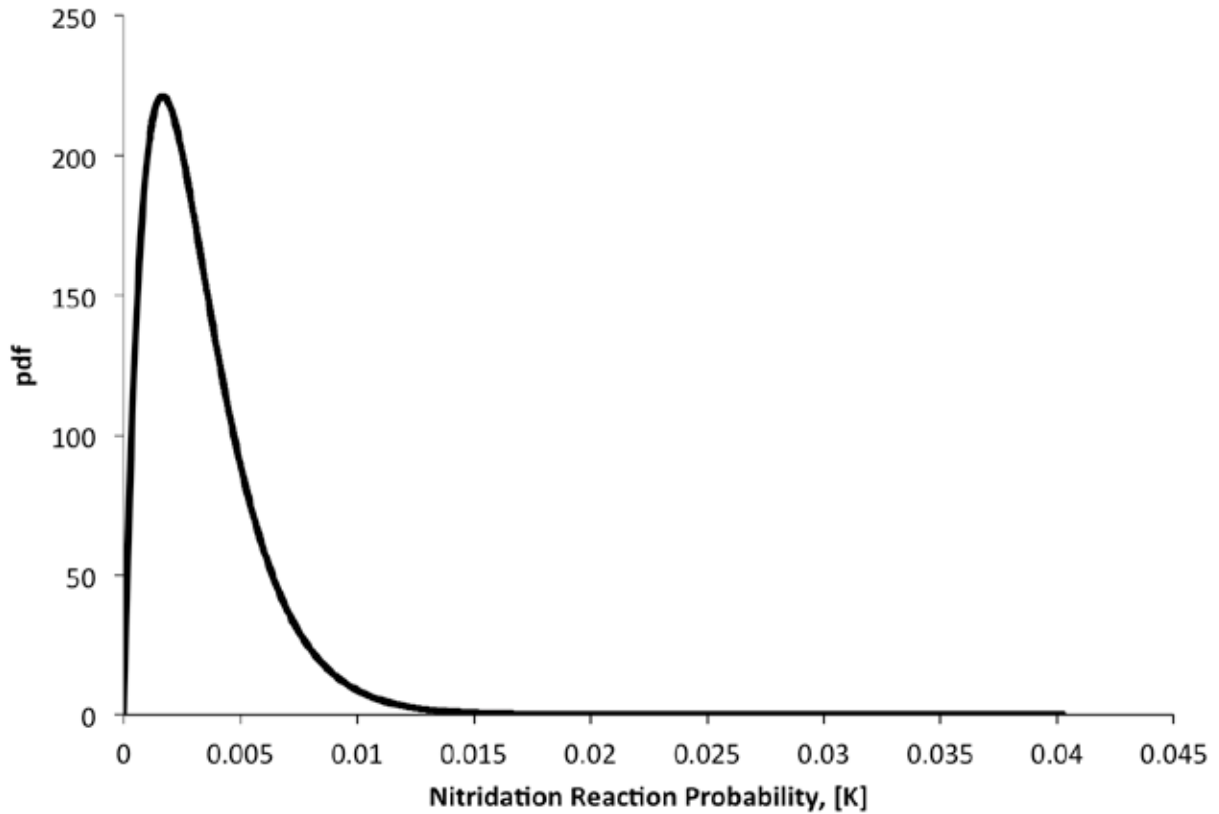


Figure 5.6: Probability density function of the nitridation reaction probability, which is a beta distribution with  $\alpha = 2$  and  $\beta = 600$ .

### 5.7.2: QMOM Calculation Results

The ablation code was run with the input probability density functions described in Section 5.7.1., and using the multivariate QMOM analysis described in Section 5.4.2.: The resulting cumulative distribution function for the ablation rate is shown below in Figure 5.7. The nominal value of the ablation rate, which is the value computed at the means of all of the distributions, had been found previously to be  $6.54 \times 10^{-5}$  m/s; based on the computed final cdf, there is an approximately 66% probability that the ablation rate would be higher than this value. The actual expected value of the surface recession rate is  $6.86 \times 10^{-5}$  m/s.

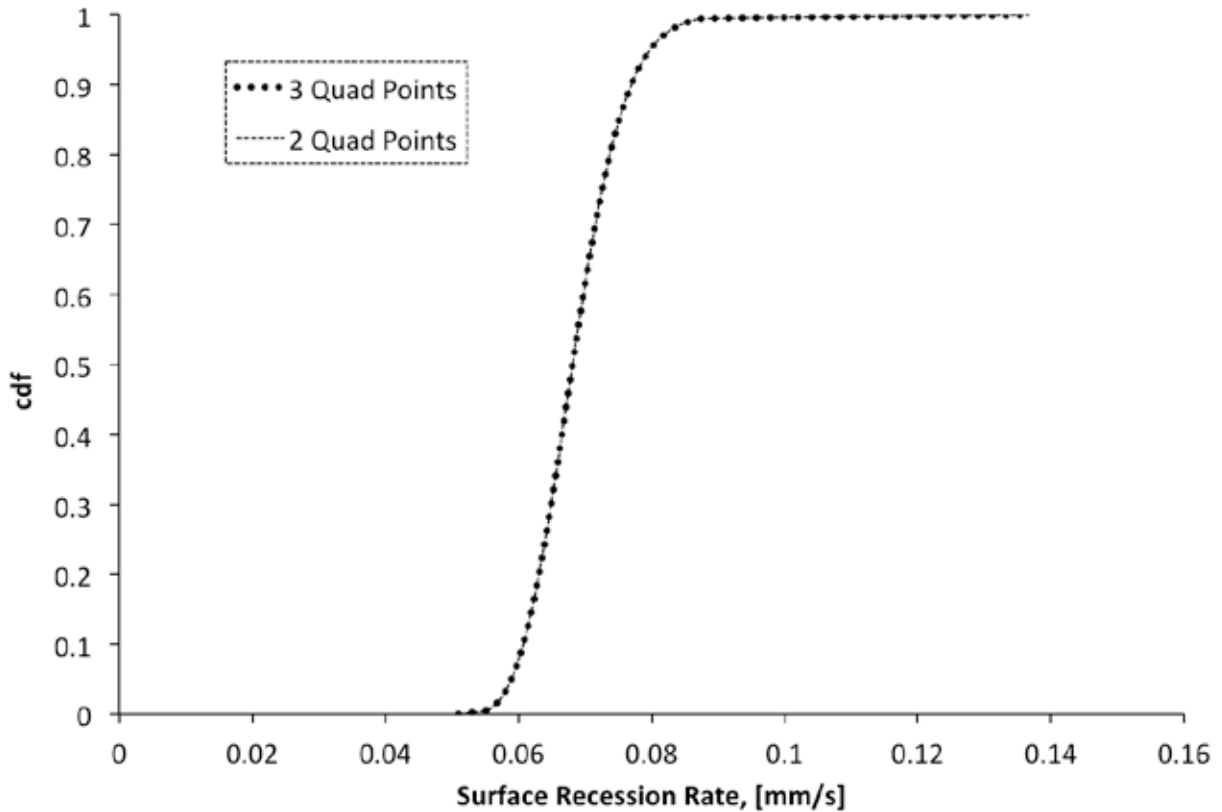


Figure 5.7: Cumulative distribution function for the surface recession rate, using the input pdfs described in Section 5.7.1:.

The QMOM calculations were performed for two and three quadrature points for the input probability densities, and both sets of calculations yielded nearly identical cumulative distribution functions. The expected value is off by less than a tenth of a percent between the two curves, and the higher order moments have even smaller differentials. As was a concern, the large values of the sublimation pre-exponential made it impossible to perform the calculations with higher numbers of quadrature points. That said, using three quadrature points allows us to compute six moments of the input distributions, which gives us a very good approximation.

From a design perspective, the cumulative distribution information is very useful. The designer can easily compute the probability that an ablation rate is above some desired quantity, and use that analysis to make a risk-informed decision. Say that we do not want the ablation rate

to exceed 0.07 mm/s because of the flight path that our vehicle is taking---there is a 40% chance that, given our uncertainty of the input variables, the ablation rate will exceed that value. The designer can make a judgment that this is an acceptable level of risk, he or she can go back and look at different elements of the design to try to lower that risk, or he or she can try to decrease the level of uncertainty in the input quantities by making improved measurements or collecting more data.

## Chapter 6: Conclusions and Future Work

Over the course of this thesis, an ablation code using finite-rate surface chemistry and a quasi-steady in-depth decomposition model was discussed and analyzed. A film transfer boundary layer was coupled to the ablation code to enable it to function as a separate, stand-alone code, which entailed developing models for both the heat and mass transfer as well as hypersonic shocks.

This fully-coupled code was found to compare reasonably well to arcjet experiments performed by Covington [35], though the uncertainty in these calculations is high due to the difficulty in determining the conditions upstream of the shock for input to the ablation code. It was also found to compare well to the unsteady ablation code Chaleur [6], under certain circumstances that allowed for a better comparison of the material response. Finally, it was found to compare very well to calculations made by Chen and Milos using the GIANTS code [8] with a finite-rate surface chemistry model. Over the course of these exercises it became evident that, because of the way the surface chemistry is computed, the ablation code has abilities that are absent from traditional equilibrium-based ablation codes. The fact that a user of the ablation code has direct control over the surface reaction rates, along with the fact that it uses the computationally inexpensive quasi-steady formulation, leads to the code being a perfect candidate for uncertainty analysis, which was performed using QMOM.

It would be interesting and instructive to perform this uncertainty analysis over a wider range of freestream conditions and ablator materials---decomposing ablators such as PICA and Avcoat immediately spring to mind. However, future QMOM tests should be compared to Monte Carlo methods for the purpose of checking the error in the calculations. QMOM in general seems extremely promising, though, and should be applied in a wider range of situations in ablation. That said, it could potentially be useful for libMoM to compute central moments or normalized moments, such that the moments of large variables are not computationally intractable.

More data about the surface reactions, which are extremely important in our formulation, would be very much desirable for decreasing the end uncertainty as a result of any uncertainty analysis. Furthermore, it would generally help a great deal to be able to compare the ablation code to a wider range of experimental conditions. While there are obviously issues with performing ablation-related experiments due to the difficulty of achieving high-enthalpy flow while still being able to characterize that flow, it is very important that ablation calculations be grounded by experimental research.

## Appendix A: Ablation Code Inputs

The inputs to the ablation code are provided in an input file that is meant to be parsed with the aid of the GRVY toolbox, a set of high performance computing utilities developed at PECOS. Comments in the input file are prepended with # symbols, and strings and vector inputs are enclosed in single quotation marks. The input file is broken into groups of related inputs, and these groups have descriptive headers enclosed in brackets (i.e. [ablation1d], etc.).

### A.1: INPUTS IN THE [WRAPPER] SECTION

#### A.1.1: General Inputs

- `use_film_transfer_bl` – set to 1 to use the film transfer model for computation of flow-side terms with the film transfer boundary layer as laid out in Section 2.3.; set this to 0 to not model the flow.
- `heat_transfer_model` – set this to 0 for a user-specified heat transfer coefficient, 1 for the Fay-Riddell model outlined in Section 2.3.2.: When using the user-specified heat transfer coefficient, the heat flux is driven by a temperature differential rather than an enthalpy differential as in the Fay-Riddell model.
- `corrections` – 0 keeps the heat fluxes uncorrected, 1 computes and applies the blowing and hot wall corrections.
- `body_radius` – the effective radius of curvature of the blunt body being computed. This value is only required if the Fay-Riddell model is being used.

#### A.1.2: Flow Inputs

- Infinite parameters: A number of parameters in the flow outside of the shock are currently required as inputs, though these parameters are deprecated and therefore not used.

- `shock_density_ratio` – the ratio of the density across the shock,  $\rho_0/\rho_1$ . This value is only required if the Fay-Riddell model is being used.
- Freestream parameters – values at the boundary layer edge for:
  - `freestream_mass_fractions` – mass fractions at the boundary layer edge. This parameter must have the same number of species as the model (10- or 13-species) being used
  - `freestream_temperature` – the temperature at the boundary layer edge, [K].
  - `freestream_pressure` – the pressure at the boundary layer edge, [Pa].
  - `freestream_velocity` – the gas velocity at the boundary layer edge, [m/s].

## A.2: INPUTS IN THE [ABLATION1D] SECTION

- `ablator` – ‘charring1’ for a decomposing material, ‘graphite1’ for a nondecomposing material.
- `type` – ‘charring’ for a decomposing material, ‘non-charring’ for a nondecomposing material.
- `chemistry` – ‘13species’ for the 13-species chemistry model, ‘10species’ for the 10-species chemistry model
- `diffusion` – ‘mass-frac’ for mass-fraction based diffusion, ‘mole-frac’ for mole fraction based diffusion. Note that the film boundary layer model is only compatible with the ‘mass-frac’ option at this point.
- `dump_file_output` – 1 to output solution parameters to solution.txt, 0 to write any file output
- `verbose_mode` – 1 to write information out during calculations, 0 to suppress output

- `use_external_fluxes` – 1 to allow input heat and mass fluxes directly to the ablation code. These fluxes are held constant throughout the iteration process, and the option is meant for a loose coupling scheme.
- `use_external_thermal_code` – 1 to accept gas-side thermal conductivity from an external model. A thermal conductivity must be provided as an input, so this is not really an option any more.
- `use_experimental_C3_eq_conc` – 1 to use an equilibrium mole fraction of tricarbon that is fitted in an Arrhenius form to experimental data – this method also sets the tricarbon reaction rate  $\beta_{C_3}$  to an Arrhenius fit. An option of 0 uses  $x_{C_3}$  fitted in an Arrhenius fit to ACE data, but sets  $\beta_{C_3}$  to 1.
- `use_equilibrium_solver` – 1 solves for pyrolysis gases using equilibrium methods; 0 uses composition values hard coded into the program.
- `use_surface_equilibrium_chemistry` – 0 uses the finite rate chemistry discussed in Section 2.2.2.; 1 uses surface composition calculated at equilibrium using the same method as the pyrolysis gases, as discussed in Sections 2.2.3: and 3.3:.
- `use_petsc` – a value of 1 uses the PETSc solver rather than the internal Newton solver. PETSc uses finite difference of the residual equations to compute the Jacobians.
- `recession_guess` – a guess of the recession rate to initialize the computations
- `max_iters` – the maximum number of Newton iterations to be used when computing a solution
- `newton_tol` – the convergence criterion used in the Newton solver
- `urelax_species` – the underrelaxation parameter for species in the internal Newton solver
- `urelax_temperature` – the underrelaxation parameter for temperature in the internal Newton solver
- `urelax_equilibrium` – the underrelaxation parameter for the internal equilibrium solver.

### A.3: INPUTS IN THE [ABLATION/STANDALONE] SECTION

This section covers the inputs that are passed to the ablation code in library form when it is called with another program. When they are not passed directly to the code, they must be read in as inputs. In the situation described in this paper, with the coupled film transfer boundary layer, most of these values are not used, and the ones that are used only to initialize the solution.

- $T_{nw}$  – near-wall value of temperature, [K]. When the ablation code is coupled to a CFD code, this is the value used to compute the heat flux to the surface. When it is not, this value is used to initialize a guess of the surface temperature.
- $P_w$  – the pressure at the ablating surface, [Pa].
- $\delta$  – distance from the point that the  $T_{nw}$  value is taken at to the surface, [m].
- $Q_{rad}$  – value of input radiative heat flux, [ $W/m^2$ ].
- $temp\_gradient$  – value of temperature gradient in the gas phase at the wall, [K/m] when the convective heat flux is not approximated by finite-difference or another model.
- $thermal\_cond$  – thermal conductivity of the gas phase, [W/mK].
- $Q_{flux}$  – constant heat flux input from other sources, [ $W/m^2$ ]; this differs from  $Q_{rad}$  because  $Q_{rad}$  is attenuated by the absorption coefficient of the surface.
- $C_{nw}$  – a vector of mass or mole fractions near the wall. This value is used in a similar fashion to  $T_{nw}$ , but for diffusive mass flux rather than convective heat flux.
- $Dig$  – a vector of diffusion coefficients for each gas in the gas phase, [ $kg/m\cdot s$ ].
- $C\_gradient$  – a vector of the gradients of the concentrations (mole or mass fractions) at the surface.
- $chem\_diff\_flux$  – a vector of the diffusive mass fluxes at the surface, [ $kg/m^2\cdot s$ ]. This value is used only when the `use_external_fluxes` parameter is set to 1.
- $temp\_cond\_flux$  – a value for the convective heat flux at the surface, [ $W/m^2$ ]. This value is used only when the `use_external_fluxes` parameter is set to 1.

#### A.4: INPUTS IN THE [ABLATOR/PROPS/GRAPHITE1] SECTION

This section defines the material properties of a nondecomposing ablator.

- `akc` – the thermal conductivity of the ablator, [W/mK].
- `rhoc` – the density of the ablator, [kg/m<sup>3</sup>].
- `absr_rad` – the absorptivity of the ablator.
- `eps_rad` – the emissivity of the ablator.
- `Cpc` – the specific heat capacity of the ablator, [J/kgK].
- `Tref` – the reference temperature for the virgin enthalpy of formation calculations; this is also assumed to be the temperature of the backside of the ablator.
- `thick` – the thickness of the ablator, [m]. This parameter is not currently used in the calculations at all.

#### A.5: INPUTS IN THE [ABLATOR/PROPS/CHARRING1] SECTION

This section defines the material properties of a decomposing ablator.

- `akch` – char thermal conductivity, [W/mK].
- `rhoch` – char density, [kg/m<sup>3</sup>].
- `Cpch` – char specific heat, [J/kgK].
- `eps_rad` – emissivity of the char.
- `absr_rad` – absorptivity of the char
- `thick` – thickness of the ablator [m]. As mentioned previously, this parameter is unused in the calculations.
- `akv` – virgin thermal conductivity, [W/mK].
- `rhov` – virgin density, [kg/m<sup>3</sup>].
- `Cpv` – virgin specific heat, [J/kgK].
- `hfv` – enthalpy of formation of the virgin, [J/kgK].
- `Tref` – the reference temperature for the virgin enthalpy of formation, [K].

- `Tpyrol` – the temperature that the pyrolysis gas equilibrium composition is computed at, [K].
- `Cfrac` – fraction of carbon in the virgin material.
- `Hfrac` – fraction of hydrogen in the virgin material.
- `Ofrac` – fraction of oxygen in the virgin material.
- `Nfrac` – fraction of nitrogen in the virgin material.

#### **A.6: INPUTS IN THE [ABLATION1D/CHEMISTRY/10SPECIES] SECTION**

- `num_species` – number of chemical species considered in this model.
- `num_elems` – number of elemental species considered in this model.
- `num_cmpnds` – number of compound species considered in this model.
- `species` – vector of the names of the species considered in this model.
- `mweights` – vector of the molecular weights of the species in `species`.
- `solid_species` – vector of the names of species in the solid
- `mweight_solids` – vector of the molecular weights of the species in the solid
- `Ea_O` – activation energy of oxygen for the  $C + O \rightarrow CO$  reaction
- `Ea_C3` – activation energy for the carbon sublimation reaction
- `Ea_C3eq` – activation energy for the equilibrium concentration of  $C_3$
- `Ea_C3eq_exp` – experimentally correlated activation energy for the equilibrium concentration of  $C_3$ . Used in the `use_experimental_C3_eq_conc` model.
- `A_O` – preexponential for the  $C + O \rightarrow CO$  reaction.
- `A_C3` – preexponential for the carbon sublimation reaction
- `A_C3eq` – preexponential for the equilibrium concentration of  $C_3$ .
- `A_C3eq_exp` – experimentally correlated preexponential for the equilibrium concentration of  $C_3$ . Used in the `use_experimental_C3_eq_conc` model.
- `Beta_O2` – reaction probability of  $O_2$  in the  $C + O_2 \rightarrow CO_2$  reaction

- $\text{Beta\_N}$  – reaction probability of nitrogen in the  $\text{N} + \text{C} \rightarrow \text{CN}$  reaction.
- Specific heat/enthalpy/entropy calculation coefficients: Each entry is a vector of each coefficient for all of the species in the denoted temperature range. For example,  $a1\_1$  is all of the  $a_1$  coefficients for the species considered in the flow in the first temperature range. There are three temperature ranges and thus three sets of  $a$  and  $b$  variables. There is also a set of entries for the solid.

#### **A.7: INPUTS IN THE [ABLATION1D/CHEMSITRY/13SPECIES] SECTION**

The set of inputs is precisely the same as for the `10species` section, though the vectors of coefficients should have a length of 13 rather than 10.

## Appendix B: Nominal Parameters

### B.1: GRAPHITE ABLATOR PROPERTIES

Property	Value	Source
Thermal conductivity, $k_c$	0.2 W/m-K	Incropera [44]
Density, $\rho_c$	2162.5 kg/m <sup>3</sup>	Incropera [44]
Absorptivity, $\alpha$	1.0	Incropera [44]
Emissivity, $\epsilon$	1.0	Incropera [44]
Specific heat, $C_{p,c}$	1004.8 J/kg-K	Incropera [44]

### B.2: PICA PROPERTIES

Property	Value	Source
Char thermal conductivity, $k_c$	0.05 W/m-K	Tran [41]
Char density, $\rho_c$	201.06 kg/m <sup>3</sup>	Tran [41]
Char specific heat, $C_{p,c}$	1400 J/kg-K	Tran [41]
Absorptivity, $\alpha$	0.9	Tran [41]
Emissivity, $\epsilon$	0.9	Tran [41]
Virgin thermal conductivity, $k_v$	0.04 W/m-K	Tran [41]
Virgin density, $\rho_v$	227.45 kg/m <sup>3</sup>	Tran [41]
Virgin heat of formation, $\Delta h_{f,v}^\circ$	-844337 J/kg-K	Tran [41]
Pyrolysis temperature, $T_{pyrol}$	1000 K	Arbitrary Estimate
C fraction in virgin	0.5315	Park [45]
H fraction in virgin	0.1285	Park [45]
O fraction in virgin	0.34	Park [45]
N fraction in virgin	0.0	Park [45]

### B.3: KINETIC PARAMETERS

Parameter	Value	Source
O activation energy, $E_{a,O}$	1160.0 K	Chen and Milos [8]
C <sub>3</sub> equilibrium activation energy, $E_{a,C_3,eq}$	90908 K	Chen and Milos [8]
O pre-exponential, $A_O$	0.63 s <sup>-1</sup>	Chen and Milos [8]
C <sub>3</sub> equilibrium pre-exponential, $A_{C_3,eq}$	6.27×10 <sup>14</sup> Pa	Chen and Milos [8]
O <sub>2</sub> reaction probability, $\beta_{O_2}$	0.25	Chen and Milos [8]
N reaction probability, $\beta_N$	0.003	Marschall [11]

## Appendix C: Jacobian of the Ablation Code

### C.1: COMMON TERMS

When computing the Jacobian matrix of the ablation code, we need to take the partial derivatives of all of the residual equations with respect to the solution variables. As such, because there are parameters that appear frequently in the residual equations, there are common derivative terms that will frequently appear in the Jacobian sensitivities.

#### C.1.1: Sensitivities of the Gas Phase Density

The gas phase density is defined as

$$\rho_g = \frac{p}{RT} \quad \text{C.1}$$

which, because of the definition of the specific gas constant  $R$  may be written

$$\rho_g = \frac{p}{\bar{R}T \sum_{i=1}^{N_s} \frac{Y_i}{W_i}} \quad \text{C.2}$$

As such, the derivative of the gas phase density with respect to the  $j^{\text{th}}$  mass fraction is

$$\frac{\partial \rho_g}{\partial Y_j} = \frac{p}{W_j \sum_{i=1}^{N_s} \frac{Y_i}{W_i}} \quad \text{C.3}$$

The gas phase density is insensitive to the blowing velocity, but its sensitivity to the surface temperature may be written

$$\frac{\partial \rho_g}{\partial T_w} = -\frac{p}{RT_w^2} = -\frac{\rho_g}{T_w} \quad \text{C.4}$$

### C.1.2: Sensitivities of Reaction Terms

Each reaction source/sink term,  $\tilde{N}_i$ , is composed of mass loss/production rates from the reactions that produce or destroy that species. Each of these mass loss/production rates generally follows the form

$$\dot{m}_{i,j}'' = \rho_g Y_i \sqrt{\frac{k_B T}{2\pi m_i}} \beta_i \frac{W_j}{W_i} \quad \text{C.5}$$

which represents the rate of loss or production of the  $i^{\text{th}}$  species from reactions involving the  $j^{\text{th}}$  species.

We can define the molecular velocity as

$$v_i = \sqrt{\frac{k_B T}{2\pi m_i}} \quad \text{C.6}$$

It is insensitive to the gas phase composition and the blowing velocity, and its derivative with respect to the wall temperature may be written as

$$\frac{\partial v_i}{\partial T_w} = \sqrt{\frac{k_B}{8\pi m_i T_w}} \quad \text{C.7}$$

Depending on the species being considered, the reaction probability  $\beta_i$  may be either a constant or a function of temperature. For constant  $\beta_i$ ,

$$\frac{\partial \beta_i}{\partial T_w} = 0 \quad \text{C.8}$$

For  $\beta$  as a function of the wall temperature of the form

$$\beta_i = A_i \exp\left(-\frac{E_{a,i}}{T_w}\right) \quad \text{C.9}$$

the sensitivity to temperature is

$$\frac{\partial \beta_i}{\partial T_w} = A_i \frac{E_{a,i}}{T_w^2} \exp\left(-\frac{E_{a,i}}{T_w}\right) \quad \text{C.10}$$

Like  $v_i, \beta_i$  is insensitive to the blowing velocity and the composition.

We can now compute the sensitivities of the various mass loss rates with respect to the solution parameters. The mass loss rates are insensitive the blowing velocity. The derivative of  $\dot{m}''_{i,j}$  with respect to the mass fraction of the  $k^{\text{th}}$  species is

$$\frac{\partial \dot{m}''_{i,j}}{\partial Y_k} = \frac{\partial \rho_g}{\partial Y_k} Y_i v_i \beta_i \frac{W_j}{W_i} \quad i \neq k \quad \text{C.11}$$

$$\frac{\partial \dot{m}''_{i,j}}{\partial Y_k} = \frac{\partial \rho_g}{\partial Y_k} Y_i v_i \beta_i \frac{W_j}{W_i} + \rho_g v_i \beta_i \frac{W_j}{W_i} \quad i = k \quad \text{C.12}$$

and its sensitivity to temperature can be written

$$\frac{\partial \dot{m}''_{i,j}}{\partial T_w} = \left[ \frac{\partial \rho_g}{\partial T_w} Y_i v_i \beta_i + \rho_g Y_i \frac{\partial v_i}{\partial T_w} \beta_i + \rho_g Y_i v_i \frac{\partial \beta_i}{\partial T_w} \right] \frac{W_j}{W_i} \quad \text{C.13}$$

Because the mass loss rate due to carbon sublimation is written in the form

$$\dot{m}''_{C_3,C} = \rho_g (x_{C_3,eq} - x_{C_3}) v_{C_3} \beta_{C_3} \quad \text{C.14}$$

its sensitivities are computed slightly differently from the rest of the mass loss rates. The sensitivity to the mass fraction of the  $k^{\text{th}}$  species is

$$\frac{\partial \dot{m}''_{C_3,C}}{\partial Y_k} = \frac{\partial \rho_g}{\partial Y_k} (x_{C_3,eq} - x_{C_3}) v_{C_3} \beta_{C_3} \quad k \neq C_3 \quad \text{C.15}$$

$$\frac{\partial \dot{m}''_{C_3,C}}{\partial Y_k} = \frac{\partial \rho_g}{\partial Y_k} (x_{C_3,eq} - x_{C_3}) v_{C_3} \beta_{C_3} - \rho_g v_{C_3} \beta_{C_3} \quad k \neq C_3 \quad \text{C.16}$$

and the sensitivity to temperature is

$$\begin{aligned} \frac{\partial \dot{m}''_{C_3,C}}{\partial T_w} &= \frac{\partial \rho_g}{\partial T_w} (x_{C_3,eq} - x_{C_3}) v_{C_3} \beta_{C_3} + \rho_g \frac{\partial x_{C_3,eq}}{\partial T_w} v_{C_3} \beta_{C_3} \\ &\quad + \rho_g (x_{C_3,eq} - x_{C_3}) \frac{\partial v_{C_3}}{\partial T_w} \\ &\quad + \rho_g (x_{C_3,eq} - x_{C_3}) v_{C_3} \frac{\partial \beta_{C_3}}{\partial T_w} \end{aligned} \quad \text{C.17}$$

In the above equation, the derivative of the equilibrium tricarbon mole fraction with respect to temperature may be written

$$\frac{\partial x_{C_3,eq}}{\partial T_w} = \frac{A_{C_3,eq} E_{a,C_3,eq}}{P T_w^2} \exp\left(\frac{-E_{a,C_3,eq}}{T_w}\right) \quad C.18$$

Finally, with all of the mass loss terms computed, it is simple to compute the sensitivities of the source/sink terms with the relationships given in Section 2.2.2:. As an example, take the terms for carbon monoxide:

$$\frac{\partial \tilde{N}_{CO}}{\partial Y_j} = \frac{\partial \dot{m}''_{O,C}}{\partial Y_j} \frac{W_{CO}}{W_C} + \frac{\partial \dot{m}''_{O_2,C}}{\partial Y_j} \frac{W_{CO}}{W_C} \quad C.19$$

where the derivatives will depend on the species given. For temperature, the sensitivities look very similar:

$$\frac{\partial \tilde{N}_{CO}}{\partial T_w} = \frac{\partial \dot{m}''_{O,C}}{\partial T_w} \frac{W_{CO}}{W_C} + \frac{\partial \dot{m}''_{O_2,C}}{\partial T_w} \frac{W_{CO}}{W_C} \quad C.20$$

The mass production/consumption rate is not sensitive to the blowing velocity at all, and therefore that term is not considered.

### C.1.3: Sensitivities of the Pyrolysis Flux

The pyrolysis mass flux is defined as

$$\dot{m}''_{py} = \rho v_w \left(1 - \frac{\rho_{ch}}{\rho_v}\right) \quad C.21$$

As such, the sensitivities are simple to compute based on previously derived quantities.

$$\frac{\partial \dot{m}''_{py}}{\partial Y_j} = \frac{\partial \rho_g}{\partial Y_j} v_w \left(1 - \frac{\rho_{ch}}{\rho_v}\right) \quad C.22$$

$$\frac{\partial \dot{m}''_{py}}{\partial v_w} = \rho_g \left(1 - \frac{\rho_{ch}}{\rho_v}\right) \quad C.23$$

$$\frac{\partial \dot{m}''_{py}}{\partial T_w} = \frac{\partial \rho_g}{\partial T_w} v_w \left(1 - \frac{\rho_{ch}}{\rho_v}\right) \quad C.24$$

## C.2: SENSITIVITIES OF THE MASS BALANCE EQUATIONS

Each of the mass balance equations, as laid out in Sections 2.2.2: and 3.1.: can be broken into a blowing term  $B$ , a reaction term  $N$ , a pyrolysis term  $P$ , and a diffusive term  $J$ :

$$\begin{aligned} R_i &= J_i|_{g,w} + \rho_g v_w Y_{i,w} - \tilde{N}_i - \dot{m}''_{py} Y_{i,py} \\ &= J_i + B_i - N_i + P_i \end{aligned} \tag{C.25}$$

The sensitivities of each of these terms may be computed separately, and then summed to find the full sensitivity.

### C.2.1: Sensitivities of the Diffusive Term

The sensitivities of the diffusive mass flux are computed by finite difference, as was briefly mentioned in Section 3.1.1.: Therefore, we can say that the sensitivity of the diffusive mass flux to the  $j^{\text{th}}$  mass fraction is

$$\frac{\partial J_i}{\partial Y_j} = \frac{1}{\Delta Y_j} [J_i(Y_j + \Delta Y_j) - J_i(Y_j)] \tag{C.26}$$

The sensitivity to the surface temperature is

$$\frac{\partial J_i}{\partial T_w} = \frac{1}{\Delta T_w} [J_i(T_w + \Delta T_w) - J_i(T_w)] \tag{C.27}$$

and the sensitivity to the blowing velocity is assumed to be zero, though it may actually not be due to the small influence of the blowing velocity on the blowing correction. This will not change the overall accuracy of the solution, as the same residual equation is being minimized; however, leaving out the sensitivity may make the solution slightly harder to reach.

### C.2.2: Sensitivities of the Blowing Term

The blowing term is

$$B_i = \rho_g v_w Y_{i,w} \tag{C.28}$$

and its sensitivities with respect to wall temperature, blowing velocity, and surface mass fraction are

$$\frac{\partial B_i}{\partial T_w} = \frac{\partial \rho_g}{\partial T_w} v_w Y_{i,w} \quad \text{C.29}$$

$$\frac{\partial B_i}{\partial v_w} = \rho_g Y_{i,w} \quad \text{C.30}$$

$$\frac{\partial B_i}{\partial Y_j} = \begin{cases} \frac{\partial \rho_g}{\partial Y_j} v_w Y_{i,w} & i \neq j \\ \frac{\partial \rho_g}{\partial Y_j} v_w Y_{i,w} + \rho_g v_w & i = j \end{cases} \quad \text{C.31}$$

### C.2.3: Sensitivities of the Reaction Term

The sensitivities of the reaction terms are computed as noted in Section C.1.2.:

### C.2.4: Sensitivities of the Pyrolysis Flux Term

The pyrolysis flux term given here is the pyrolysis gas production rate multiplied by the mass fraction of the  $i^{\text{th}}$  species. We can therefore write the residuals simply in terms of previously defined quantities:

$$\frac{\partial P_i}{\partial Y_j} = \frac{\partial \dot{m}''_{py}}{\partial Y_j} Y_i + \dot{m}''_{py} \quad i = j \quad \text{C.32}$$

$$\frac{\partial P_i}{\partial Y_j} = \frac{\partial \dot{m}''_{py}}{\partial Y_j} Y_i \quad i \neq j \quad \text{C.33}$$

$$\frac{\partial P_i}{\partial v_w} = \frac{\partial \dot{m}''_{py}}{\partial v_w} Y_i \quad \text{C.34}$$

$$\frac{\partial P_i}{\partial T_w} = \frac{\partial \dot{m}''_{py}}{\partial T_w} Y_i \quad \text{C.35}$$

## C.3: SENSITIVITIES OF THE SURFACE RESSION RATE EQUATION

The surface recession rate equation is

$$R_{N_s+1} = \rho_g v_w - \dot{m}''_C - \dot{m}''_{py} \quad \text{C.36}$$

where the mass loss rate of carbon is the sum of all of the mass loss rates of species that react with the surface (namely, O, O<sub>2</sub>, and N) and the rate of production of C<sub>3</sub>. For the purposes of computing the sensitivities, this equation will be broken into a blowing flux,  $B$ , a char mass loss rate,  $C$ , and a pyrolysis mass loss rate,  $P$ , whose sensitivities will be evaluated separately.

### C.3.1: Sensitivities of the Blowing Flux

The sensitivities of the blowing flux are

$$\frac{\partial B}{\partial Y_j} = \frac{\partial \rho_g}{\partial Y_j} v_w \quad \text{C.37}$$

$$\frac{\partial B}{\partial v_w} = \rho_g \quad \text{C.38}$$

$$\frac{\partial B}{\partial T_w} = \frac{\partial \rho_g}{\partial T_w} v_w \quad \text{C.39}$$

### C.3.2: Sensitivities of the Char Mass Loss Rate

The char mass loss rate, as mentioned previously, is the sum of a number of mass loss rates. It may be written

$$\dot{m}''_C = \dot{m}''_{O,C} + \dot{m}''_{O_2,C} + \dot{m}''_{N,C} + \dot{m}''_{C_3,C} \quad \text{C.40}$$

and its sensitivities are therefore

$$\frac{\partial \dot{m}''_C}{\partial Y_j} = \frac{\partial \dot{m}''_{O,C}}{\partial Y_j} + \frac{\partial \dot{m}''_{O_2,C}}{\partial Y_j} + \frac{\partial \dot{m}''_{N,C}}{\partial Y_j} + \frac{\partial \dot{m}''_{C_3,C}}{\partial Y_j} \quad \text{C.41}$$

$$\frac{\partial \dot{m}''_C}{\partial v_w} = 0 \quad \text{C.42}$$

$$\frac{\partial \dot{m}''_C}{\partial T_w} = \frac{\partial \dot{m}''_{O,C}}{\partial T_w} + \frac{\partial \dot{m}''_{O_2,C}}{\partial T_w} + \frac{\partial \dot{m}''_{N,C}}{\partial T_w} + \frac{\partial \dot{m}''_{C_3,C}}{\partial T_w} \quad \text{C.43}$$

where the mass loss rate sensitivities are as they were discussed in Section C.1.2:.

### C.3.3: Sensitivities of the Pyrolysis Mass Flux

The sensitivities of the pyrolysis term in the surface recession equation are the same as those derived in Section C.1.3.:

### C.4: SENSITIVITIES OF THE ENERGY BALANCE EQUATION

Like the mass balance equations, the energy equation can be broken into its component pieces which can be evaluated separately for their sensitivities. The energy equation, as discussed in Section 3.1.1., can be written

$$R_{N_s+2} = q''_{conv} - \sum_{i=1}^{N_s} i_i [\tilde{N}_i + \dot{m}''_{py} Y_{i,py}] + \alpha q''_{rad} - \epsilon \sigma T_w^4 + \rho_v v_s i_{f,v}^{\circ} \quad C.44$$

and will be broken into a convective heating term, a reaction term, a pyrolysis gas term, two radiation terms, and a term to represent the convection of virgin material into the bottom control surface. As such, we can say

$$R_{N_s+2} = q''_{conv} - q''_{reac} - q''_{pyr} + q''_{rad,in} - q''_{rad,out} + q''_{virgin} \quad C.45$$

#### C.4.1: Sensitivities of the Convective Heat Flux Term

The sensitivities of the convective heat flux, like those of the diffusive mass flux, shall be computed by finite difference. The convective heat flux is assumed to be insensitive to both blowing velocity and composition, though some actual dependence may exist through the heat transfer coefficient and its corrections. Since the only variable the convective heat flux is sensitive to is the temperature, we may simply write

$$\frac{\partial q''_{conv}}{\partial T_w} = \frac{1}{\Delta T_w} [q''_{conv}(T_w + \Delta T_w) - q''_{conv}(T_w)] \quad C.46$$

Where the convective heat flux is computed according to the models laid out in Section 2.3.:

### C.4.2: Sensitivities of the Reaction Energy Term

The energy consumed and released through the reactions at the surface is represented as the sum of the enthalpies of each species multiplied by their individual consumption or production rates. The enthalpy of a given species is insensitive to the gas composition and the blowing velocity, and the consumption/production rate has been discussed in Section C.1.2:---it is sensitive only to the surface temperature and gas phase composition.

As such, we may write the sensitivity to the  $j^{\text{th}}$  mass fraction as

$$\frac{\partial q''_{\text{reac}}}{\partial Y_j} = \sum_{i=1}^{N_s} i_i \frac{\partial \tilde{N}_i}{\partial Y_j} \quad \text{C.47}$$

and to the surface temperature as

$$\frac{\partial q''_{\text{reac}}}{\partial T_w} = \sum_{i=1}^{N_s} \left[ i_i \frac{\partial \tilde{N}_i}{\partial T_w} + \frac{\partial i_i}{\partial T_w} \tilde{N}_i \right] \quad \text{C.48}$$

### C.4.3: Sensitivities of the Pyrolysis Enthalpy Flux Term

The sensitivity of the pyrolysis enthalpy flux term is very similar to that of the reaction term. Again, the enthalpy of a given species is insensitive to the gas composition and the blowing velocity; the pyrolysis mass flux is sensitive to all of the solution variables, as has been discussed in Section C.1.3:.. We can therefore write the sensitivities as

$$\frac{\partial q''_{\text{pyrol}}}{\partial Y_j} = \sum_{i=1}^{N_s} i_i \frac{\partial \dot{m}''_{\text{py}}}{\partial Y_j} \quad \text{C.49}$$

$$\frac{\partial q''_{\text{pyrol}}}{\partial v_w} = \sum_{i=1}^{N_s} i_i \frac{\partial \dot{m}''_{\text{py}}}{\partial v_w} \quad \text{C.50}$$

$$\frac{\partial q''_{\text{pyrol}}}{\partial T_w} = \sum_{i=1}^{N_s} \left[ i_i \frac{\partial \dot{m}''_{\text{py}}}{\partial T_w} + \frac{\partial i_i}{\partial T_w} \dot{m}''_{\text{py}} \right] \quad \text{C.51}$$

#### C.4.4: Sensitivities of the Radiative Heat Fluxes

The input radiative heat flux,  $q''_{rad,in}$ , is completely insensitive to the surface conditions, because it is taken as a constant input value. The output radiative flux is sensitive to neither the blowing velocity nor the surface composition, but is sensitive to temperature. That sensitivity may be written

$$\frac{\partial q''_{rad,out}}{\partial T_w} = 4\sigma\epsilon T_w^3 \quad C.52$$

#### C.4.5: Sensitivities of the Virgin Material Enthalpy Flux

Because the protected surface, the surface which is used as the bottom control surface of the control volume in the ablator, is assumed to be at a constant temperature throughout the computations, all of the terms in the virgin convection flux are constant---except for the rate at which the virgin material enters the control volume. Since the total mass flux through both ends of the control volume must be the same, we can say

$$\rho_g v_w = \rho_v v_s \quad C.53$$

and replace the velocity and density terms in the virgin flux by those in the gas phase. As such, the sensitivities are

$$\frac{\partial q''_{virgin}}{\partial Y_j} = \frac{\partial \rho_g}{\partial Y_j} v_w h_{f,v}^\circ \quad C.54$$

$$\frac{\partial q''_{virgin}}{\partial v_w} = \rho_g h_{f,v}^\circ \quad C.55$$

$$\frac{\partial q''_{virgin}}{\partial T_w} = \frac{\partial \rho_g}{\partial T_w} v_w h_{f,v}^\circ \quad C.56$$

## Bibliography

- [1] Moyer, C.B. and Rindal, R.A., “Finite Difference Solution for the In-Depth Response of Charring Materials Considering Surface Chemical and Energy Balances”, NASA CR-1061, 1968.
- [2] Kendall, R.M., Rindal, R.A., and Bartlett, E.P., “A Multicomponent Boundary Layer Chemically Coupled to an Ablating Surface”, *AIAA Journal*, Vol. 5, No. 6, 1967, pp. 1063-1071.
- [3] “User’s Manual, Aerotherm Chemical Equilibrium Computer Program (ACE 81)”, UM-81-11/ATD, Acurex Corporation, Aerotherm Division, Mountain View, CA, 1981.
- [4] Chen, Y.-K. and Milos, F.S., “Ablation and Thermal Response Program for Spacecraft Heatshield Analysis”, *Journal of Spacecraft and Rockets*, Vol. 36, No. 3, 1999, pp. 475-483.
- [5] Chen, Y.-K. and Milos, F.S., “Two-Dimensional Implicit Thermal Response and Ablation Program for Charring Materials”, *Journal of Spacecraft and Rockets*, Vol. 38, No. 4, 2001, pp. 473-481.
- [6] Blackwell, B.F., Amar, A.J., and Edwards, J.R., “One-Dimensional Ablation with Pyrolysis Gas Flow Using a Full Newton’s Method and Finite Control Volume Procedure”, *39th AIAA Thermophysics Conference*, AIAA 2007-4535, AIAA, Miami, FL, 2007.
- [7] Zhluktov, S.V., and Abe, T., “Viscous Shock-Layer Simulation of Air- flow past Ablating Blunt Body with Carbon Surface”, *Journal of Thermophysics and Heat Transfer*, Vol. 13, No. 1, 1999, pp. 50-59.
- [8] Chen, Y.-K. and Milos, F.S., “Navier–Stokes Solutions with Finite Rate Ablation for Planetary Mission Earth Reentries”, *Journal of Spacecraft and Rockets*, Vol. 42, No. 6, 2005, pp. 961-970.
- [9] Park, C., *Nonequilibrium Hypersonic Aerothermodynamics*, Wiley-Interscience, New York, 1990.
- [10] Park, C. and Bogdanoff, D.W., “Shock-Tube Measurement of Nitridation Coefficient of Solid Carbon”, *Journal of Thermophysics and Heat Transfer*, Vol. 20, No. 3, 2006, pp. 487-492.
- [11] Zhang, L., Pejakovic, D.A., Marschall, J., and Fletcher, D.G., “Laboratory Investigation of Active Graphite Nitridation by Atomic Nitrogen”, *41st AIAA Thermophysics Conference*, AIAA 2009-4251, AIAA, San Antonio, TX, 2009.
- [12] Zoby, E.V., “Empirical Stagnation-Point Heat Transfer Relation in Several Gas Mixtures at High Enthalpy Levels”, NASA TN D-4799, 1968.

- [13] Sutton, K. and Graves, R.A., "A General Stagnation-Point Convective Heating Equation for Arbitrary Gas Mixtures", NASA TR R-376, 1971.
- [14] Fay, J.A., and Riddell, F.R., "Theory of Stagnation-Point Heat Transfer in Dissociated Air", *Journal of the Aeronautical Sciences*, Vol. 25, No. 2, 1958, pp. 73-85.
- [15] Fay, J.A. and Kemp, "Theory of Stagnation-Point Heat Transfer in a Partially Ionized Diatomic Gas", *AIAA Journal*, Vol. 1, No. 12, 1963, pp. 2741-2751.
- [16] Crabtree, L.F., Dommett, R.L., and Woodley, J.G., "Estimation of Heat Transfer to Flat Plates, Cones, and Blunt Bodies", R. & M. No. 3637, 1970.
- [17] Quinn, R.D. and Gong, L., "A Method for Calculating Transient Surface Temperatures and Surface Heating Rates for High-Speed Aircraft", NASA/TP-2000-209034, 2000.
- [18] Upadhyay, R.R. and Ezekoye, O.A., "Treatment of Size-Dependent Aerosol Transport Processes Using Quadrature Based Moment Methods", *Journal of Aerosol Science*, Vol. 37, No. 7, 2006, pp. 799-819.
- [19] Upadhyay, R.R. and Ezekoye, O.A., "Treatment of Design Fire Uncertainty Using Quadrature Method of Moments", *Fire Safety Journal*, Vol. 43, No. 2, 2008, pp. 127-139.
- [20] McGraw, R., "Description of Aerosol Dynamics by the Quadrature Method of Moments", *Aerosol Science and Technology*, No. 27, 1997, pp. 255-265.
- [21] Karian, Z.A. and Dudewicz, E.J., *Fitting Statistical Distributions: The Generalized Lambda Distribution and Generalized Bootstrap Methods*, CRC Press, Boca Raton, 2000.
- [22] Upadhyay, R.R., "Coupling of Ablation Code with DPLR", PECOS Technical Report, University of Texas at Austin, Austin, Texas, 2010 (Unpublished).
- [23] Kays, W.M., Crawford, M.E., Weigand, B., *Convective Heat and Mass Transfer*, 4<sup>th</sup> Ed., McGraw-Hill, New York, 2005.
- [24] Amar, A.J., "Modeling of One-Dimensional Ablation with Porous Flow Using Finite Control Volume Procedure", Master's Thesis, Department of Aerospace Engineering, North Carolina State University, Raleigh, NC, 2006.
- [25] Anderson, J.D., *Hypersonic and High Temperature Gas Dynamics*, McGraw-Hill, New York, 1989.
- [26] Zehe, M.J., "NASA Thermo Build", Thermodynamic Property Database [online database], URL: <http://cea.grc.nasa.gov/> [cited 3 December 2010].

- [27] McBride, B.J. and Gordon, S., "Computer Program for Calculation of Complex Chemical Equilibrium Compositions and Applications II. Users Manual and Program Description", NASA RP-1311, 1996.
- [28] Kee, R.J., Coltrin, M.E., and Glarborg, P., *Chemically Reacting Flow: Theory and Practice*, Wiley-Interscience, Hoboken, 2003.
- [29] Poling, B.E., Prausnitz, J.M., and O'Connell, J.P., *The Properties of Gases and Liquids*, 5<sup>th</sup> Ed., McGraw-Hill, New York, 2001.
- [30] Svelha, R.A., "Estimated Viscosities and Thermal Conductivities of Gases at High Temperatures", NASA Technical Report R-132, 1962.
- [31] Bird, R.B., Stewart, W.E., and Lightfoot, E.N., *Transport Phenomena*, Wiley, New York, 1960.
- [32] EDL Shock & Detonation Toolbox, Shock Calculations, Software Package, Ver. 1.0, Caltech Explosion and Detonation Laboratory, Pasadena, CA, URL: [http://www.galcit.caltech.edu/EDL/public/cantera/html/SD\\_Toolbox/](http://www.galcit.caltech.edu/EDL/public/cantera/html/SD_Toolbox/) [cited 3 December 2010].
- [33] Cantera, Equilibrium Calculations, Software Package, Ver. 1.8, Caltech, Pasadena, CA, URL: <http://code.google.com/p/cantera/> [cited 3 December 2010].
- [34] Wittliff, C.E. and Curtis, J.T., "Normal Shock Wave Parameters in Equilibrium Air", Cornell Aeronautical Laboratory Report No. CAL-111, 1961.
- [35] Covington, M.A., et al., "Erratum on Performance of a Low Density Ablative Heat Shield Material", *Journal of Spacecraft and Rockets*, Vol. 45, No. 4, 2008, pp. 854-864.
- [36] Fletcher, D.G., "Measurement Requirements for Improved Modeling of Arcjet Facility Flows", *Measurement Techniques for High Enthalpy and Plasma Flows*, RTO EN-8, RTO AVG, Rhode-Saint-Genese, Belgium, 1999.
- [37] Winovich, W., "On the Equilibrium Sonic-Flow Method for Evaluating Electric-Arc Air-Heater Performance", NASA TN D-2132, 1964.
- [38] Zobe, E.V. and Sullivan, E.M., "Effects of Corner Radius on Stagnation Point Velocity Gradients on Blunt Axisymmetric Bodies", NASA TM X-1067, 1965.
- [39] Park, C., et al., "Comparison of Enthalpy Determination Methods for Arc-Jet Facility", *Journal of Thermophysics and Heat Transfer*, Vol. 20, No. 4, 2006, pp. 672-679.
- [40] Sakai, T., "Computational Simulation of High-Enthalpy Arc Heater Flows", *Journal of Thermophysics and Heat Transfer*, Vol. 21, No. 1, 2007, pp. 77-85.

[41] Tran, H.K., et al., "Phenolic Impregnated Carbon Ablators (PICA) as Thermal Protection Systems for Discovery Missions", NASA TM 110440, 1997.

[42] McGraw, R. and Wright, D.L., "Chemically Resolved Aerosol Dynamics for Internal Mixtures by the Quadrature Method of Moments", *Journal of Aerosol Science*, Vol. 34, No. 2, 2003, 189-209.

[43] Figliola, R.S. and Beasley, D.E., *Theory and Design for Mechanical Measurements*, Wiley, New York, 1991.

[44] Incropera, F.P and DeWitt, D.P, *Fundamentals of Heat and Mass Transfer*, 5<sup>th</sup> Ed., Wiley, New York, 2002.

[45] Park, C., Jaffe, R.L., and Partridge, H., "Chemical - Kinetic Parameters of Hyperbolic Earth Entry", *Journal of Thermophysics and Heat Transfer*, Vol. 15, No. 1, pp. 76-90.

## **Vita**

Reed Anthony Anzalone was born in 1986 in Washington, D.C., and was raised in Falls Church, Virginia. There, he attended George Mason High School and graduated in 2004. He enrolled at the Virginia Polytechnic Institute and State University (Virginia Tech) and earned his B.S. in Mechanical Engineering in 2008.

When not performing ablation research, Reed enjoys cooking, music, and video games.

Permanent address: 212 W Cameron Rd, Falls Church, VA 22046

This thesis was typed by Reed Anthony Anzalone.